ALTERNATIVE ELECTRODE FABRICATION FOR LITHIUM-ION BATTERIES
USING
FLAME SPRAY PYROLYSIS

Vom Fachbereich Produktionstechnik

der

UNIVERSITÄT BREMEN

zur Erlangung des Grades
Doktor der Ingenieurswissenschaften (Dr.-Ing.)
genehmigte

Dissertation

von
Master of Science, Michael Gockeln

Gutachter: Prof. Dr. -Ing. habil. Matthias Busse
Prof. Dr. -Ing. Arno Kwade (Technische Universität Braunschweig)

Tag der mündlichen Prüfung: 22.11.2022

“We are equal beings and the universe is our relations with each other.
The universe is made of one kind of entity: each one is alive,
each determines the course of his own existence.”

Thaddeus Golas, American writer (1924-1997)

Abstract

Conventional lithium-ion batteries (LIBs) are famous for their high energy and power density, efficiency, and long cycle life. These properties make LIBs a highly relevant power source for the electronic consumer market, electric vehicles, and stationary energy storage applications. Major drawbacks of LIBs are high production costs and safety issues arising from the flammability of the liquid electrolyte. All-solid-state lithium-ion batteries (ASSBs) incorporate incombustible solid-state electrolytes, avoiding leakages and burning hazards. ASSBs also suffer from high production costs and large-scale fabrication routes are unavailable yet, hampering their commercial launch. Electrode fabrication for both LIBs and ASSBs is complex and expensive, bearing a significant potential to reduce overall battery fabrication costs.

Flame spray pyrolysis (FSP) has emerged as a promising tool for synthesizing ultrafine, phase-pure and crystalline battery electrode active materials. In this dissertation, it will be shown that FSP offers a cost-effective and facile synthesis of spinel $Li_4Ti_5O_{12}$ (LTO) based electrodes for both LIBs and ASSBs. Four process-oriented key hypotheses were formulated and tested in anticipation of technical improvements of LIBs and ASSBs electrode manufacturing: (1) high-purity FSP-produced LTO powders perform comparable in LIB cells, independent of the underlying precursor solvent combinations, (2) LIB performances of carbon-coated LTO (LTO/C) composite electrodes, prepared by double flame spray pyrolysis (DFSP) and transfer-lamination technique, are improved for higher transfer-lamination pressures, (3) FSP-based *in-situ* deposition of well-crystallized LTO thin-films to flexible substrates, makes commonly applied thermal treatments for particle crystallization obsolete. Assembled in ASSBs, the flexible LTO electrodes are cyclable in flat and statically bent condition without mechanical deterioration, (4) adjusting the compression procedure of such *in-situ* deposited LTO thin-films leads to modified microstructures. Less porous particle networks promote the intrinsic charge carrier transports, resulting in larger practicable capacities.

Based on the new scientific results, following conclusions have been drawn: (1) irrespective of the applied precursor solvent combination, electrochemical performances of FSP-synthesized phase-pure LTO are indeed comparable. This finding allows battery manufacturers to choose the combination that serves best their economic and ecologic needs, (2) the LIB performance of LTO/C electrodes, fabricated by DFSP/transfer-lamination, was enhanced for higher transfer-lamination pressures based on an enlarged electrically conductive particle network. Due to the optimized microstructure with favorable electrical and ionic transport properties, the stronger compressed LTO/C electrodes were electrochemically outperforming analogous electrodes prepared by conventional doctor blading technique. Remarkably, the novel transfer-lamination method was independent of any solvents and binding additives, (3) crystalline LTO powders were successfully deposited to temperature-sensitive flexible polymer substrates, without requiring any additional sintering step. Assembled into ASSBs, the flexible LTO electrodes showed excellent cycling stability. Upon static battery-cell bending, the capacities were slightly reduced, but the electrochemical reversibility of the LTO electrode was still remarkable, (4) yielded capacities of flexible LTO thin-film electrodes were significantly enhanced after reducing the porosity. Microstructural simulations indicated that this was due to enlarged LTO particle coordination numbers, and increased contact densities at interfaces to adjacent functional layers.

Zusammenfassung

Konventionelle Lithium-Ionen-Batterien (LIB) sind bekannt für ihre hohe Energie- und Leistungsdichte, Effizienz und Lebensdauer. Diese Eigenschaften machen LIB zur hochrelevanten Stromquelle für portable Elektronik, Elektromobilität und stationäre Energiespeichersysteme. Nachteile der LIB sind hohe Produktionskosten und Sicherheitsrisiken die auf der Brennbarkeit der flüssigen Elektrolytmaterialien beruhen. Feststoffbatterien beinhalten unbrennbare Feststoffelektrolyte, wodurch Leckagen und Brandgefahren ausgeschlossen sind. Allerdings leiden auch Feststoffbatterien unter hohen Herstellungskosten. Fehlende großskalige Fabrikationsrouten der einzelnen Zellkomponenten erschweren zusätzlich die kommerzielle Vermarktung von Feststoffbatterien. Besonders die Elektrodenherstellung ist für beide, flüssig- sowie feststoffelektrolytbasierte LIB-Systeme, komplex und kostspielig. Technische Innovationen bergen hier ein nennenswertes Potential für die Gesamtkostenreduzierung der Batterieherstellung.

Die Flammensprühpyrolyse (FSP) hat sich zu einem vielversprechenden Werkzeug für die Herstellung von ultrafeinen, phasenreinen und kristallinen Batterieelektrodenmaterialien entwickelt. In dieser Dissertation wird gezeigt, dass sich die FSP für eine trockenbeschichtende Herstellung von Spinel-$Li_4Ti_5O_{12}$ (LTO) basierten Elektroden für konventionelle LIB und Feststoffbatterien eignet. Vier prozessorientierte Schlüsselhypothesen wurden formuliert und im Hinblick auf eine verbesserte Leistungsfähigkeit der beiden lithiumbasierten Speichertechnologien getestet: (1) hochreines FSP-produziertes LTO zeigt unabhängig von den zugrundeliegenden Präkursoren und Lösungsmitteln, eine vergleichbare Leistungsfähigkeit in LIB-Zellen, (2) die Leistungsfähigkeit von kohlenstoffbeschichteten LTO Kompositelektroden (LTO/C), hergestellt durch die Doppelflammensprühpyrolyse (DFSP) und Transferlaminierungstechnik, ist verbessert für höhere Laminierungsdrücke, (3) die FSP-basierte *in-situ* Abscheidung von polykristallinen LTO Dünnschichten auf flexiblen Substraten, erübrigt typischerweise notwendige Kalzinierungsschritte zur Partikelkristallisierung. In Feststoffbatterien assembliert, sind die flexiblen LTO Elektroden in flachem, sowie statisch gebogenem Zustand, zyklisierbar, (4) abhängig von Art und Intensität der Komprimierungsmethode, kann die Mikrostruktur der *in-situ* abgeschiedenen LTO Dünnschichten modifiziert werden. Weniger poröse Partikelnetzwerke verbessern den intrinsischen Ladungsträgertransport, was zu größeren praktischen Kapazitäten führt.

Basierend auf den wissenschaftlichen Ergebnissen wurden folgende Schlussfolgerungen getroffen: (1) die Wahl der Präkursoren und Lösungsmittel für die FSP-Synthese von LTO, spielt eine untergeordnete Rolle, solange das hergestellte LTO phasenrein ist. Diese Erkenntnis erlaubt dem Batteriehersteller eine Kombination auszuwählen, die seinen ökonomischen und ökologischen Vorstellungen entspricht, (2) die Leistungsfähigkeit von LTO/C Elektroden in LIB, hergestellt

durch DFSP/Transferlaminierung, kann durch höhere Transferlaminierungsdrücke verbessert werden. Dies resultierte vor allem aus einem vergrößerten elektrisch leitfähigen Partikelnetzwerk. Die stärker komprimierten LTO/C Elektroden haben Vergleichselektroden, die durch das konventionelle Rakelverfahren hergestellt wurden, in ihrer elektrochemischen Leistung übertroffen. Dies wurde erneut der bemerkenswert homogenen Mikrostruktur, mit verbesserten elektrischen aber auch ionischen Transporteigenschaften, zugeschrieben. Hervorzuheben an dieser Technik ist, dass sie zeiteffizient, technisch simpel und unabhängig von Lösungsmitteln und Binderadditiven ist, (3) polykristalline LTO Pulver wurden erfolgreich auf temperaturempfindliche Polymersubstrate abgeschieden, ohne einen zusätzlichen Sinterschritt zu benötigen. In Feststoffbatterien verarbeitet, zeigten die flexiblen LTO Elektroden eine exzellente Zyklenstabilität. Unter statischer Batteriezellbiegung waren die Kapazitäten leicht reduziert, allerdings unter Beibehaltung der Zyklenstabilität, (4) die erreichten Kapazitäten der flexiblen LTO Dünnschichten wurden signifikant verbessert für Schichten mit geringerer Porosität. Mikrostrukturelle Simulationen haben ergeben, dass dies aufgrund von erhöhter LTO Partikelkoordinierung, sowie größeren LTO Kontaktdichten an den Grenzflächen zu den benachbarten funktionellen Schichten, beruhte.

List of Content

List of Abbreviations

ADCs - Areal discharge capacities

BET - Brunauer-Emmett-Teller surface area analysis

CV - Cyclic voltammetry

DSC - Differential scanning calorimetry

EDX - Energy dispersive X-ray spectroscopy

EHA - 2-ethyl hexanoic acid

EtOH - Ethanol

ESS - Energy storage system

Flex-TFB - Flexible all-solid-state thin-film batteries

FSP - Flame spray pyrolysis

GCPL - Galvanostatic cycling with potential limitations

HOMO - Highest occupied molecular orbital

LAA - Lithium acetylacetonate

LIB - Lithium-ion batteries

LiPON - Lithium phosphorous oxynitride

LNT - Lithium nitrate

LSM - Laser scanning microscope

LTB - Lithium *tert*-butoxide

LTO - $Li_4Ti_5O_{12}$

LTO/C(DBap)- As-prepared doctor bladed LTO electrode

LTO/C(DBc) - Calendered doctor bladed LTO electrode

LUMO - Lowest unoccupied molecular orbital

MS - Mass spectrometry

NMP - N-methyl-2-pyrrolidon

PTFE	-	Polytetrafluorethylen
PVDF	-	Polyvinylidene fluorid
RCR	-	Relative capacity retention
SDC	-	Specific discharge capacity
SEI	-	Solid electrolyte interface
SEM-FIB	-	Scanning electron microscopy coupled with focused ion beam
TEM	-	Transmission electron microscopy
TGA	-	Thermogravimetric analysis
XRD	-	X-ray diffraction

Acknowledgements

This dissertation was possible due to the great support of my teachers, fellow students, co-workers, family and friends. I would like to express my sincere gratitude to:

Prof. Dr. -Ing. habil. Matthias Busse, head of the “Fraunhofer Institute for Manufacturing Technology and Advanced Materials” in Bremen, for supporting this work and for examining this dissertation. I am thankful for his faith in me and for supporting our working group “Innovative Sensor and Functional Materials”, managed by my boss at the time, Dr. Robert Kun.

Prof. Dr. -Ing. Arno Kwade, head of the “Institute for Particle Technology” at the TU Braunschweig, for being the second supervisor of this dissertation. I appreciate that my dissertation is co-evaluated by a longtime experienced scholar in battery manufacturing and particle technology.

Dr. Robert Kun for his scientific guidance during my PhD time. Unfortunately, he left Germany and the University of Bremen for new challenges and was not able to supervise this work to its completeness. I am very thankful that he believed in my abilities for offering me the PhD position and introducing me to the fascinating world of battery research and engineering. I am inspired by his ability to create innovative ideas and his practical way of problem solving.

Dr. habil. Suman Pokhrel, who opened the door of production engineering and flame spray pyrolysis for me. While offering me the chance to do my master thesis with him and Robert Kun, he enabled me to do this whole work. His faith and his constant support as well as his skills in scientific thinking, writing and presentation, allowed me to fundamentally enhance my scientific abilities.

Prof. Dr. -Ing. habil. Lutz Mädler, head of the department “Leibniz-Institut für Werkstofforientierte Technologien, Universität Bremen” for supporting and maintaining the mutual collaboration between the groups of “Reactive Spraying” and “Innovative Sensor and Functional Materials”. The collaboration allowed me to do the here reported work in a great working atmosphere. The high laboratory, infrastructural and moral standards in his department and his working group are exemplary for me.

Dr. -Ing. Julian Schwenzel, head of the Fraunhofer IFAM group “Department for Electrical Energy Storage Systems” for enabling me to do the battery related work in his department. In the great working atmosphere in the labs of Fraunhofer IFAM Oldenburg, I learned the practical fundamentals of battery fabrication.

Prof. Dr. Fabio La Mantia that he was constantly and kindly willing to discuss any electrochemical questions related to my work.

All my dear friends and colleagues who constantly supported me and my work with their knowledge, affection and time. To name some of the closest, I thank Jens Glenneberg, Ingo Bardenhagen, Ghoncheh Kasiri, Miriam Gutjahr, Frederieke Langer, Sebastian Jentzsch, Maggie Werner, Ralf Meyer, Alexander Gräfenstein, Florian Meierhofer, Haipeng Li, Hendrik Naatz, Valentin Baric and Thomas Varelmann.

The master students that I have worked with in different projects: Elena Crespo, John Gerges, Ana Palacios Saura and Bernhard Linnebaum.

My family and friends, foremost my mother, for the consistent support, love, advice, and time, they provided me with.

Declaration of Authorship

I, Michael Gockeln, certify that this dissertation titled “ALTERNATIVE ELECTRODE FABRICATION FOR LITHIUM-ION BATTERIES USING FLAME SPRAY PYROLYSIS”, and the work presented in it, was written without external support and that I did not use any other sources and auxiliary means than those quoted. Parts of the experimental results, related to the pressure-dependent fabrication of flexible $Li_4Ti_5O_{12}$ thin-film electrodes, were elaborated together with the master student Ana Palacios Saura, while the microstructural simulations were conducted in a research collaboration by Tom Ruiter and Valentin Baric as, published in ACS Appl. Energy Mater. 2020, 3, 9667−9675.

Place/date

Michael Gockeln

I. Introduction

1. Fundamentals About Lithium-Ion Batteries

1.1. Lithium-Ion Batteries as Energy Storage System

Lithium-ion batteries (LIBs) offer high specific energy, high efficiency, and long cycle life, making them a highly relevant energy storage system for current and seminal technologies such as portable electronics, electric mobility, and stationary energy storage. Portable electronics for entertainment, telecommunication and computing devices are increasingly demanded by today´s information-rich and mobile society. Electric mobility is intended to replace the internal combustion engine-based technology, to reduce carbon-dioxide emissions and air pollution in urban areas. Stationary energy storage systems are helpful to balance the intermittence of renewable energy resources such as photovoltaic and wind energy [1–6].

Systematically, LIBs belong to the group of energy storage systems (ESS). A classical ESS is a resource, facility or device, inheriting a certain amount of energy that is exploitable for energy supply. Primary ESSs include various nonrecurring natural reservoirs, consisting of accumulated biomass such as oil deposits, coal tips or natural gas fields. The contained “primary” energy can be withdrawn only once by irreversibly burning the energy-material in plants, firings or vehicles [7].

Secondary ESSs can be recharged multiple times, preferably with sustainable energy from renewable energy resources. They include various technologies, distinguishable based on their discharge time, as illustrated in **Fig. 1.1**. Chemical ESSs such as caverns and porous formations store *e.g.* methane and hydrogen, and can provide energy dischargeable in days or several months. This resembles magnitudes and discharge times, comparable to “primary” fossil fuel reservoirs. Secondary ESS technologies that exhibit rather short discharge times of less than 24 hours, comprise capacitors and inductors (electrical ESSs), flywheels, latent heat, compressed air, hydroelectric, and electrochemical ESSs.

Electrochemical ESSs are represented by batteries (green area in **Fig. 1.1**). The term “battery” colloquially describes the combination of several electrochemical cells, which historically resembled a stack of cannons, *i.e.* “battery”, in military terminology. These electrochemical cells are also known as galvanic cells and can be of “primary” or “secondary” nature, depending on the applied chemistry. Batteries can be distinguished into low-temperature, including LIBs, high-temperature, and redox-flow systems [7,8].

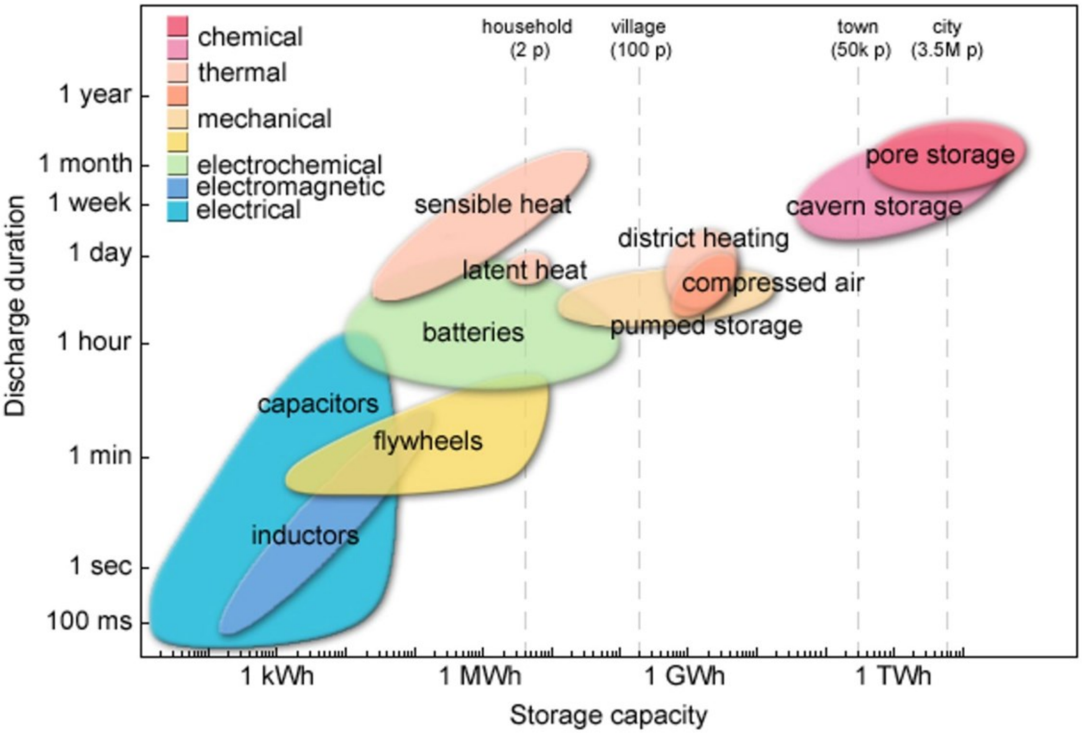

Fig. 1.1 Ragone plot showing various secondary ESSs based on their storage capacity and discharge duration. Lithium-ion and other battery technologies (green area) belong to the short-term energy supplier. The colored fields represent existing energy storage facilities in Germany in 2016. The dashed vertical lines indicate the typical annual energy consumption of groups of different sizes (adapted with permission from [7]).

1.2. The Galvanic Cell

Galvanic cells are generally autonomous devices that are able to electrochemically convert the energy of a chemical reaction between an oxidizing and reducing agent into electrical energy. In such redox reactions, the reducer is being oxidized by releasing electrons, while the oxidizer is reduced due to take-up of electrons [8]. In an exemplary redox reaction, silver oxide acts as the oxidizer while metallic zinc is the reducer:

$$Ag_2O + Zn \rightarrow 2Ag + ZnO \tag{1.1.}$$

During physical contact, the electrons transfer from zinc atoms of metallic zinc to silver ions of silver oxide. Assuming reaction **1.1.** occurred in a container in which silver oxide was thoroughly mixed with fine zinc powder, all the electron transfers would have occurred at the grain boundaries, disabling the generation of a directed electrical current. The random electron transfer would merely lead to liberation of reaction energy into heat, which can even dramatically raise the temperature of the mixture [8].

In silver-zinc batteries, the very same reaction principles apply. However, instead of simply mixing powders in a container, two electrically conductive metal plates, *i.e.* electrodes, are immersed in an ion-conducting medium with dissolved ions, *i.e.* electrolyte. The electrodes and thus the related partial reactions are separated in space, enabling an ordered flow of electrical current. This setup that allows the separation of spontaneous redox reactions defines the galvanic cell, mostly just addressed as battery-cell [8].

To understand the electrochemical principles in a thermodynamically stable battery-cell, **Fig. 1.2**. schematically illustrates the relative electron energies in the electrodes with respect to an aqueous electrolyte. The energy separation of the lowest unoccupied molecular orbital (LUMO) and the highest occupied molecular orbital (HOMO), corresponds to the electrolytes' thermodynamic stability window E_g. The anode (negative electrode) and cathode (positive electrode) are electrically conductive and have electrochemical potentials of μ_A and μ_C, which correspond to the respective materials' Fermi energies (ε_F). The anode and cathode act as reducing and oxidizing agents, respectively. A μ_A above the LUMO will result in electrolyte reduction, whereas a μ_C below the HOMO will oxidize the electrolyte. In both cases, the reaction products form a so-called solid electrolyte interface (SEI) on the expense of the active materials, resulting in capacity losses.

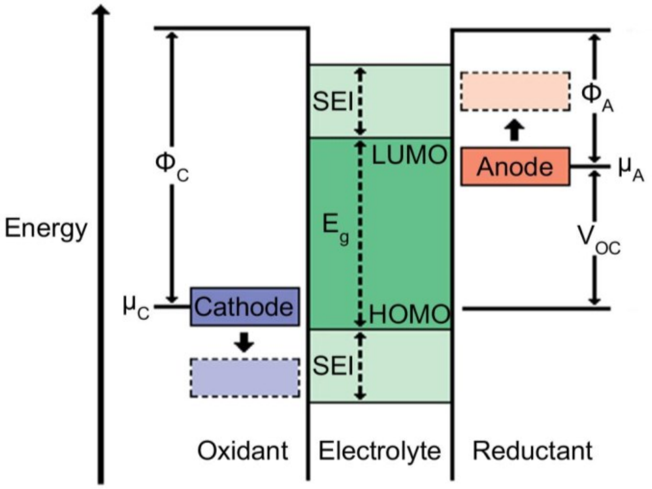

Fig. 1.2 Schematic open circuit diagram of a galvanic cell with aqueous electrolyte. Φ_A and Φ_C correspond to the anodes and cathodes work functions. E_g denotes the electrolyte stability window. Kinetic stability for μ_A and μ_C higher or lower than LUMO or HOMO, requires the formation of a SEI-layer (adapted with permission from [9]).

To avoid these so-called parasitic reactions, μ_A and μ_C are required to be present within the electrolyte thermodynamic stability window E_g, constraining the open circuit voltage eV_{oc} of a galvanic cell to:

$$eV_{oc} = \mu_A - \mu_C \leq E_g \qquad (1.2.)$$

with e as the magnitude of the electron charge.

Against its apparent drawback of causing capacity losses, the SEI-layer also acts as an indispensable passivation layer at the electrode/electrolyte interface, providing kinetic stability for larger V_{oc}, given that eV_{oc}-E_g is not too large [9]. The energy density of a battery-cell is denoted as the product ΔV_{oc}, where Δ is the capacity of reversible charge transfer per unit weight (mAh/g) between anode and cathode.

To fabricate batteries with higher open circuit voltage V_{oc} and, therefore, higher energy densities ΔV_{oc}, aqueous electrolytes can be replaced by non-aqueous electrolytes. This was discovered once lithium salts were found soluble in certain non-aqueous liquids and polymers. In applying non-aqueous electrolytes, the HOMOs of both the salt and the solvent, determines the limiting μ_C of the cathode (**Fig. 1.2**). A battery with high energy density ΔV_{oc} and longevity, consequently demands the application of suitable high capacity electrodes that have their μ_A and μ_C matched to the LUMO and HOMO of the non-aqueous/salt electrolyte, respectively.

1.3. Famous Secondary Battery Types

In modern battery technology, less than two dozen systems are produced on a commercial level. The largest production volumes are found in three systems: primary zinc-manganese, rechargeable lead acid, and rechargeable alkaline (*e.g.* nickel-cadmium) batteries. These battery systems are being manufactured for more than one century and are still widely used. During the second half of the twentieth century, LIBs and nickel-metal hydride storage batteries have gained increasing importance [8].

Despite the striking advantages of LIB technology, the other secondary battery chemistries and technologies still have their relevance. Lead-acid is the oldest and best-known electrochemical couple. It is the battery of choice for the market of starting-lighting-ignition batteries in vehicles with internal combustion engines. It is also the dominating battery type for powering industrial electric vehicles such as forklifts. Lead-acid batteries are cost-efficient but inherit a low specific energy of 30 Wh/kg [10–12]. Alkaline batteries comprise *e.g.* nickel-cadmium and nickel-metal hydride chemistries and use an alkaline solution as electrolyte. Nickel-cadmium offers a specific energy of 50 Wh/kg, fast charging capability, good specific power, and good cycle life. Due to the environmental concerns of the hazardous heavy metals, nickel-cadmium has almost completely disappeared from the portable electronics market. Nevertheless, nickel-cadmium still remains in use for industrial applications [12,13]. Nickel-metal hydride battery-cells are outperforming nickel-cadmium batteries due to a higher specific energy (~70 Wh/kg) and the substitution of toxic cadmium with specific alloys. Due to certain economic and technical advantages, nickel-metal hydride batteries are still the most applied battery system for power-assist hybrid vehicles such as the Toyota Prius. Nickel-metal hydride batteries did also have a significant market share for powering portable electronics. Since the 1990s, however, nickel-metal hydride batteries are increasingly replaced by LIBs [10,12,13]. The sodium-nickel-chloride system (ZEBRA) operates at elevated temperatures (~300°C) and has a high specific energy around 100 Wh/kg. This battery type has been used to power various electric vehicle designs. However, a required heating after longer standstill periods (<24 h) makes this battery type rather suitable for continuously used vehicles in *e.g.* fleet applications [12]. Owed to economic and safety drawbacks, as well as difficult handling of their liquid and hot components, sodium-nickel-chloride, and likewise sodium-sulfur batteries (150-240 Wh/kg [14]), are limited to niches motive powers (electrical buses) and stationary applications [13].

Another group of electrochemical cells is the redox-flow battery. The energy in this battery-type is stored primarily in the active materials which are dissolved in two externally stored electrolytes, connected through a membrane. Main advantages of this battery are the simple scalability of power and energy components. A famous flow battery type is the vanadium redox-flow battery with lifetimes greater than 10,000 cycles or ten years. Main drawbacks are a relatively low specific energy and energy density compared to other battery technologies [14,15].

From the so-called Ragone chart in **Fig. 1.3**, it becomes obvious that LIBs offer a superior trade-off in specific energy and specific power densities when compared to lead-acid, nickel-cadmium, nickel-metal hydride and the high-temperature sodium-nickel-chloride (ZEBRA) battery. The LIB system has an operation potential at ~3.7 V with high specific energy and energy densities of around 75-200 Wh/kg or 150-315 Wh/L, respectively, making this battery type applicable for weight and volume sensitive applications [5]. LIBs do not reach power densities and cycle life of supercapacitors but they exhibit significantly larger energy densities [12,16,17].

The beneficial performance of LIB technology is greatly based on the properties of its core material lithium. Lithium metal has the lowest reduction potential among all elements, *i.e.* -3.04 V *vs.* standard hydrogen electrode, giving lithium-based batteries the highest possible battery-cell voltage. Lithium is also the third lightest element with one of the smallest ionic radii of any single charged ion, explaining the extraordinarily high gravimetric capacities (theoretical capacity of 3860 mAh/g) and power densities in LIBs [18,19]. The excellence of LIB technology is represented by a discharge rate of ~8% per month, a cycle life of >1000 cycles, and wide operating temperature windows of -20 to 60°C for charge and -40 to 65°C for discharge. Noteworthy drawbacks of LIBs are high production costs and the necessity for a protective system, to avoid thermal runaway due to liquid electrolyte decomposition, with possible explosion and fire hazards [5]. The mentioned characteristics of LIBs are making this technology highly relevant for powering numerous current and future electronic devices.

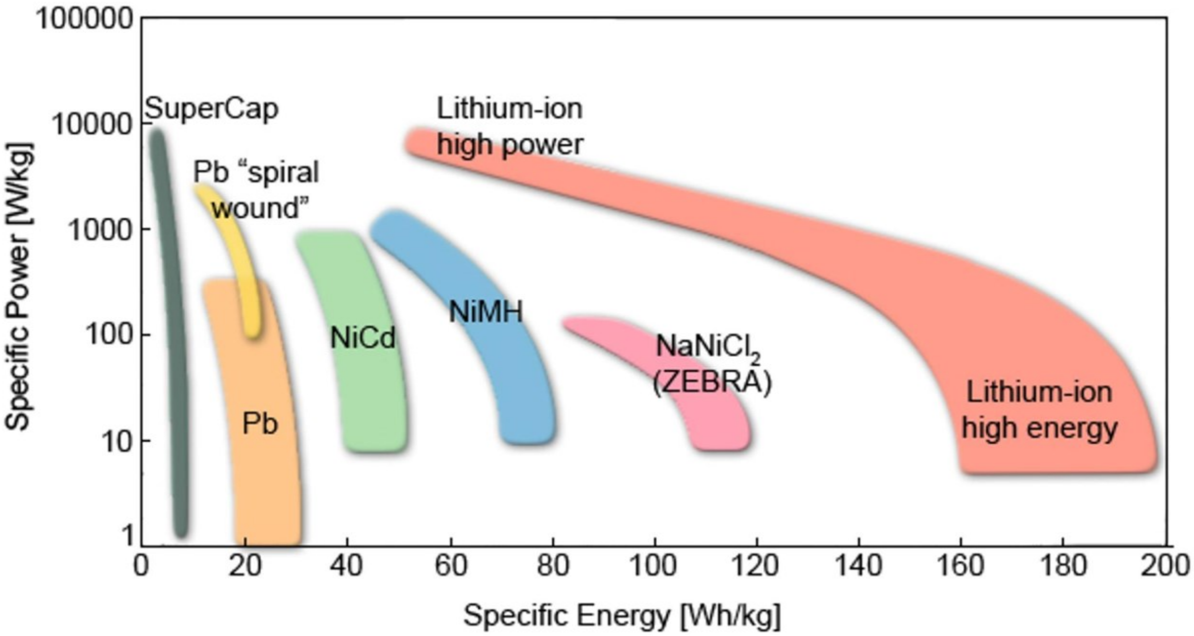

Fig. 1.3 Ragone chart showing selected battery types and their specific power and energy characteristics. Lithium-ion battery technology demonstrates a superior trade-off in specific power and specific energy (adapted with permission from [16]).

1.4. Principles of Lithium-Ion Batteries

Cathode, anode and electrolyte, as the most important active materials in LIBs, determine the electrochemical performance. The energy of LIBs is stored in the anode and cathode, while anode materials offer a larger storage capacity than cathodes. Accordingly, the cathode is the limiting factor in the performance of LIBs. The energy density of a LIB is often determined by the lithium-ion storage capacity and discharge potential of the battery-cell. The lithium-ion storage capacity arises from the (1) capability of electrode to change valence states, (2) space availability for lithium-ion storage, and (3) reversibility of intercalation reactions. The discharge potential of a cathode is directly proportional to the reduction of Gibbs free energy during lithium-insertion.

Electrodes can be distinguished into three types based on the underlying electrochemical reactions *i.e.* alloying, conversion, and intercalation reactions. These three mechanisms direct the charge storage very distinctly, resulting in different capacities, morphologies and structures. Alloying electrodes undergo a direct chemical bonding between inserted lithium-ions and the host element A, (A=Si, Ge, Sn) to form Li-A alloys. Alloying allows significantly larger specific capacities (up to one magnitude more) than other reaction mechanisms. As a drawback, this is accompanied by large volume changes of typically more than 100%. Conversion-type electrode materials can provide high theoretical capacities and are cots-efficient, but their application is hampered due to irreversible reactions. A conversion reaction occurs, when lithium-ions are inserted into nano-sized binary compounds, denoted by MX. Hereby, M can stand for transition metal such as Fe, Co and Cu, and X represents O, S, F, etc. They are rarely used alone in LIBs, but often combined with alloying mechanism [17,20].

Intercalation electrodes have intrinsic one-, two- or three-dimensional openings to allow lithium-ion transport without causing significant structural changes [20]. Intercalation-type host electrodes have available space for accommodating lithium-ions, as well as multivalent ions, to maintain electroneutrality. A commercial intercalation-type LIB comprises lithium transition metal oxides as cathodes and carbon as anodes, next to a non-aqueous, organic, carbonaceous electrolyte such as propylene carbonate, ethylene carbonate, and ethylene carbonate, in which a conductive lithium salt is dissolved [21–23]. **Fig. 1.4** shows an intercalation-type LIB with a graphite anode and $LiCoO_2$ (LCO) cathode, placed on electrically conductive copper and aluminum current collectors, respectively. A lithium-ion permeable separator electrically insulates the electrodes from each other. All components are immersed in an organic electrolyte to allow facile lithium-ion transport to the reaction sites. In the example of the graphite/LCO battery-cell, the corresponding reaction based on lithium-ion exchange can be written as: $LiC_6+CoO_2 \leftrightarrow C_6+ LiCoO_2$ [21]. To power a random electronic device by discharging the graphite/LCO battery-cell, electrons move spontaneously through the external circuit from anode (LiC_6) to cathode (CoO_2). This leads to the oxidation of LiC_6 and reduction of CoO_2. To maintain charge neutrality in LiC_6, lithium-ions deintercalate and enter the electrolyte, resulting in C. CoO_2 that attracts the electrons, maintains charge neutrality by uptake and intercalation of lithium cations from the electrolyte into its structure, leading to $LiCoO_2$. During battery charging, the whole process is occurring on reverse [5,9]. The lithium-ions are literally rocking from one electrode to the other, giving intercalation-type LIBs the nickname "rocking chair batteries" [24,25].

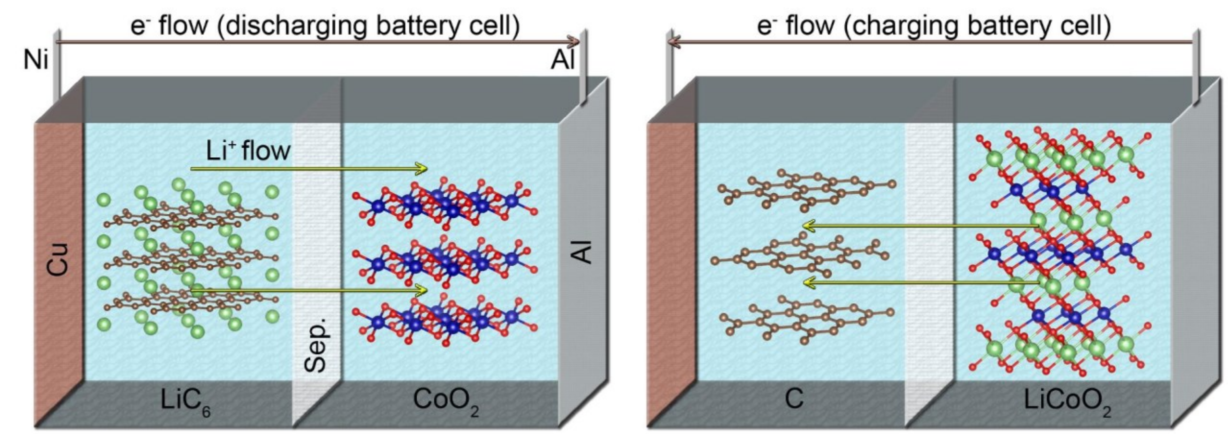

Fig. 1.4 Schematic representation of lithium-ion exchange in a graphite/LCO battery-cell. The reaction between charged (left) and discharged (right) state can be denoted as $LiC_6+CoO_2 \leftrightarrow C_6+LiCoO_2$.

1.5. $Li_4Ti_5O_{12}$ Active Material

Next to carbon as anode and LCO as cathode material, battery manufacturers can choose among numerous electrode active materials to tailor the battery properties such as energy density, power density, and cycle life, depending on the desired field of application. The cathode side, on one hand, offers a wide selection of high voltage lithium transition metal oxides with famous examples such as $LiMn_2O_4$ (LMO), $Li(Ni_{1/3}Mn_{1/3}Co_{1/3})O_2$ (NMC), and $LiFePO_4$ (LFP), as comprehensively summarized by Fergus [26]. The anode side, on the other hand, is commonly equipped with carbon-based compounds, lithium-containing alloys or spinel-$Li_4Ti_5O_{12}$ [26].

Spinel-$Li_4Ti_5O_{12}$ (LTO) is a low voltage intercalation-type material and is also reported as $Li_{4/3}Ti_{5/3}O_4$, $Li_{1.33}Ti_{1.67}O_4$, or $Li[Li_{1/3}Ti_{5/3}]O_4$. It can be used as cathode in low-voltage battery-cells or as anode against high-voltage metal oxide cathodes [26]. It is a famous member of the solid solution family $Li_{3+x}Ti_{6-x}O_{12}$ ($0 \leq x \leq 1$) [27,28]. Due to the high de-/intercalation voltage of 1.55 V (*vs.* Li^+/Li^0), LTO-based LIB cells have comparably low energy densities compared to *e.g.* LMO (around 4 V *vs.* Li^+/Li^0) [29,30]. The accommodation of three lithium-ions per unit formula allows a theoretical maximum capacity of 175 mAh/g. At a potential of 1.55 V (*vs.* Li^+/Li^0), LTO has a low-reactivity with common electrolytes. This avoids pronounced electrolyte decomposition and related SEI-layer or dendrite formation, making it a significantly safer electrode material compared to conventional graphite electrodes [31,32].

The energy densities of LTO-based LIBs may be comparably low, however, a combination of high voltage lithium transition metal oxide cathodes with LTO anodes, results in battery-cells with extraordinary cycle life numbers. Depending on the chosen cathode material, voltages are ranging from 1.55 to 3.50 V [31]. Generally, LTO-based LIB cells are more suitable for high power purposes in which high rates are applied for dis-/charging, rather than for high energy applications [32]. LTO is comparably non-toxic, inexpensive, and very famous for having negligible unit cell volume changes upon lithium insertion/extraction (8.3595 to 8.3538 Å) [30]. This so called "zero-strain property" and a high thermal stability are the basis for the long cycle lifetime of LTO [27,31]. All these features make LTO a considerable anode material in LIBs for portables and electric vehicles [27].

Crystallographically, LTO has a cubic defect spinel crystal structure with an $FD\overline{3}m$ (No. 227) space group. The unit cell parameter a is reported to be between 8.352-8.370 Å. Materials with a spinel structure have the general formula of AB_2O_4. In Wyckoff notation, the oxygen ions in 32e represent a cubic closed packed oxygen array, containing tetrahedrally coordinated 8a, 8b and 48c, and octahedrally coordinated 16c and 16d interstices that are partially occupied by the A and B cations [27,33]. At room temperature, the tetrahedral 8a sites of LTO are fully occupied with lithium, whereas the octahedral 16d sites are shared by lithium and titanium in an atomic ratio of 1 to 5. While the other sites in LTO remain empty, the structure is often denoted as $[Li_3]_{8a}[\ ]_{16c}[Ti_5Li]_{16d}[O_{12}]_{32e}$ [27,31,34]. LTO provides a three-dimensional diffusion network of possible lithium sites throughout the crystal, while other famous electrode materials are mostly constrained to two (graphite or CoO_2) or even one ($LiFePO_4$) dimension(-s). This property and the abundance of defects may explain the high rate capability of LTO. The overall lithium-ion diffusion within LTO is considered to take place mainly over the 8a and 16c positions and vacancy hopping [35,36]. Upon lithium-ion insertion the lithium-ions in the 16d sites remain immobile due to very large energy barriers [36]. Instead, lithiation moves the lithium-ions, *i.e.* three per unit formula, from the occupied 8a sites to the empty octahedral 16c sites while the additional lithium-ions are also stored in the 16c vacancies [35]. This occurs most likely due to coulombic repulsion between nearest lithium-ions occupying the 8a-16c positions. The filling of the 16c sites is accompanied with the phase transition from cubic spinel $Li_4Ti_5O_{12}$ to rock-salt $Li_7Ti_5O_{12}$, *i.e.* $[\ ]_{8a}[Li_6]_{16c}[Ti_5Li]_{16d}[O_{12}]_{32e}$ [34], according to:

$$Li_4Ti_5O_{12} + 3Li^+ + 3e^- \leftrightarrow Li_7Ti_5O_{12} \qquad [1.3]$$

LTO features strong covalent bonds between titanium and oxygen atoms, resulting in high structural stability of the crystal lattice. The resilient nature of the LTO crystal structure is favorable for the considerable reversibility of lithium de-/intercalation during cycling [31]. Major drawbacks of LTO are its low intrinsic electrical conductivity (~10^{-13} S/cm) as well as low ionic diffusion coefficient (~10^{-9}

to ~10^{-16} cm^2/s), preventing the realization of the maximum theoretical capacities of 175 mAh/g, at high dis-/charge rates [31]. To enhance the poor electrical and ionic conductivities at higher rates, researchers downsized the LTO particles into the nano-regime for two reasons: first, this reduces the diffusion pathway lengths for lithium-ions and electrons, and second, it increases the available reactive contact area between the electrolyte and LTO particles [27,37]. The electrical conductivity is additionally optimized by surface modifications. Carbon coatings in particular, can serve as multifaceted layers between electrode and electrolyte due to their excellent electrical conductivity and superior electrochemical stability [31].

1.6. Overpotentials in Batteries

Batteries reactions are not always occurring at values that one would predict from thermodynamics. Due to restricted charge transport velocities and required activation energies for electrochemical reactions, considerably higher electron energies must be applied, leading to more negative potentials. These voltage losses are termed "overpotentials" due to the additional potential that is needed to drive a reaction at a certain rate [38]. Overpotentials are considered positive upon charging (positive current) and negative upon discharging (negative current). They are inconstant and vary depending on the applied current, operation temperature, state-of-charge and the age of a battery. Overpotentials in batteries are the sum of ohmic, charge transfer, and diffusion overpotentials. Ohmic overpotentials are arising from ohmic resistances in metallic current collectors, active materials, and electrolytes. The poor and temperature-dependent conductivities of the liquid electrolyte contribute largely to ohmic losses due to significantly poorer conductivities than metallic battery-cell components. Further, the charged active material inherits a different conductivity than the discharged one, making the ohmic resistance dependent to the state-of-charge of the battery-cell. Additionally, the age of a battery-cell affects the ohmic resistance due to (1) alteration, *e.g.* consumption of the electrolyte, and (2) phenomena in the active material such as elevation of charge transfer resistances or development of passivation layers. During charge transfer at electrode/electrolyte interfaces, electrical conduction transfers into ionic conduction and vice versa. The charge transfer itself is a dynamic equilibrium resulting from a forward and backward reaction. At equilibrium condition, both reactions are equally fast so that a charge transfer in sum is factually absent. Due to overpotentials in a battery-cell, the equilibrium can be shifted causing a charge transfer into one of either direction. At the electrode/electrolyte interface, charge carriers of opposite polarity are gathered closely, which physically resembles a capacitor. Due to large active material surface areas and short distances of the charge carriers, a significant capacity, *i.e.* double layer capacity develops. The double layer capacity itself is not causing any overpotentials but it influences the overpotential of the charge transfer reactions at the interfaces. Diffusion overpotentials also depend on the geometry of diffusion channels in the battery-cell components. Therefore, porosities and thicknesses of active materials and separators, significantly affect the ion transport. Accordingly, high power batteries comprise commonly thin active material and separator layers [39].

1.7. Safety Issues in Lithium-Ion Batteries

In principal, elemental lithium (Li^0) is an ideal anode since it has the lowest reduction potential among all elements [18]. As a major drawback, however, the electrochemical potential of Li^0 is located above the LUMO of common organic electrolytes. In reference to the SEI-layer formation, Li^0 can still be used as anode, albeit, only transitorily: on repeated dis-/charging, the lithium anode experiences volumes changes that lead to repetitive local cracking of the SEI-layer and uncontrolled formation of lithium dendrites [40]. These dendrites can grow through the electrolyte and reach critical sizes. If they pinch through the separator and contact the positive electrode, it will lead to short-circuiting. A hazardous consequence may be a thermal runaway, where the electrodes' reaction with the electrolyte becomes self-sustaining, entering an autocatalytic mode. This phenomenon is the reason for many safety incidents and fires related to battery operation [41–43]. This imminent danger factually limits the application of Li^0 anodes in LIBs, to the characterization of μ_A and μ_C of practical electrodes relative to the Li^+/Li^0 energy level. Such liquid electrolyte-based characterization cells are commonly termed LIB "half-cells" and were also applied in the current work. To prevent the danger of LIB failure due to dendrite growth, two provisions have to be considered: either the anodes μ_A and cathodes μ_C match the LUMO and HOMO of the electrolyte, or the SEI-layer heals itself rapidly upon cracking. The latter, *i.e.* breaking and healing, diminishes the capacity but also significantly decelerates the rate of dendrite formation, as it is the case with *e.g.* graphite anodes, making them a viable anode material [9,44].

1.8. All-Solid-State-Batteries

State-of-the-art LIBs currently have an upper limit in energy densities of 256 Wh/kg at cell-level. This is fairly low compared to combustion engines in automobiles, having energy densities of more than 1000 Wh/kg. To become competitive, the energy density of LIBs needs to be significantly improved. The employed liquid organic electrolyte is causing further difficulties. The solvents in the liquid organic electrolyte are (1) flammable, which raises safety concerns of fires and explosions [19], (2) causing side reactions that lead to capacity fading and aging. At last, during LIB production, both the cumbersome electrolyte filling and wetting procedure, as well as the extensive formation process, are contributing to high costs [23].

As mentioned previously, elemental lithium has an extraordinary high gravimetric capacity and low electrochemical potential. Therefore, its application as metal anodes in LIBs seems inevitable to meet the requirements for electric vehicles. However, elemental lithium reacts irreversibly with common liquid organic electrolytes, leading to dendrite formation and the corresponding performance detriments and safety concerns. Maximizing the energy stored in the limited space of a LIB would even increase possible safety hazards. To enable the application of elemental lithium, various approaches have been undertaken to avoid or mitigate dendrite formation, *e.g.* by modifying the electrolyte (change concentration, using additives), lithium metal anode (forming artificial SEI, surface structuring), or separator [19,23,45,46].

All-solid-state lithium-ion batteries (ASSBs) are considered to overcome the limited energy density and safety hazards of LIBs. Contrary to LIBs that apply a porous separator soaked with the liquid organic electrolyte, ASSBs use a non-flammable solid-state electrolyte, serving as both electrical insulator and ionic conductor [23]. Due to the solid-state electrolyte, leakages, pressure build-ups from electrolyte decomposition, and burning hazards, are absent, making related precautionary measures redundant. Thus, ASSBs are less harmful and offer more architectural design options than their liquid counterparts [47].

Solid-state electrolytes often have a large electrochemical stability window, and a higher mechanical strength compared to liquid electrolytes. The latter was considered to hamper dendrite formation. However, it was recently found that lithium dendrites can still form and propagate in battery-cells that comprise such high-strength solid electrolytes. The formation of lithium dendrites in ASSBs is still incompletely understood and is described to be much more complex than in liquid electrolytes. Nevertheless, promising approaches exist for tackling dendrite formation in ASSBs such as compositing ceramic or glass electrolytes with polymers and introducing artificial interfaces between the lithium anodes and solid-state electrolytes. Eventually, the combination of lithium metal anodes and solid-state electrolytes remains a potential strategy to obtain inflammable, high-performance, and cost-efficient energy storage systems with long life-times [19].

The new cell design possibilities of ASSBs allow the realization of two-dimensional thin-film geometries and three-dimensional cell-concepts. Also the stacking of monopolar or bipolar electrode and solid-state electrolyte layers becomes feasible [48–50]. Especially bipolar battery-cell stacks will lead to increased energy- and power-densities and lower production costs, since (1) the amount of electrochemically inactive materials for each cell, such as housing, wiring, current collector, is reduced, and (2) resistive losses are decreased due to shorter charge-carrier pathways [51].

Also the realization of mechanically flexible and miniaturized power sources becomes feasible with ASSBs. Developing flexible and miniaturized on-board power supplies is a decisive requirement for the production of sophisticated micro-fabricated devices such as wearables, smart clothes, smart cards, electronic papers, electronic skins, implantable medical devices, complementary metal-oxide semiconductor backups, various sensors, and microelectromechanical systems [3,4,47,49,52–56].

Requirements to the solid-state electrolyte materials are manifold and numerous challenges have to be overcome to realize commercialization [22,46]. Major objectives are a high ionic conductivity ($>10^{-4}$ S/cm), negligible electrical conductivity, feasible electrochemical stability windows, and suitable transfer impedances at the interfaces. Furthermore, stability against anode and cathode, as well as the processability, cost, and environmental benignity, have to be considered. Unfortunately, materials that fulfill all mentioned requirements are unavailable. Nonetheless, a considerable selection of solid-state electrolyte materials has been investigated, which can be distinguished into three main groups: (1) oxides: $Li_xPO_yN_z$ (LiPON), $Li_{3x}La_{(2/3)-x}TiO_3$ (LLTO, perovskite), Li_3OCl (anti-perovskite), $Li_{14}ZnGe_4O_{16}$ (LiSICON), $Li_{1.3}Al_{0.3}Ti_{1.7}(PO_4)_3$ (LATP; NaSICON type), $Li_7La_3Zr_2O_{12}$ (LLZO, garnet), (2) sulfides: $Li_{4-x}M_{1-y}M'_yS_4$ (M=Si, Ge; M'=P, Al, Zn, Ga; Thio-LiSICON), Li_6PS_5X (X=Cl, Br, I; Argyrodites), $Li_{10}MP_2S_{12}$, (M=Ge, Sn; LGSP family), and (3) polymers: polyethylene oxide- and poly(ethylene carbonate)-based electrolytes that are often mixed with lithium salts and ceramic additives to improve lithium-ion conductivity, mechanical strength, and interface stability [22,50,57]. For the properties of the individual solid-state electrolyte materials, the interested reader is referred to the mentioned references.

LiPON, or lithium phosphorous oxide nitride, has been shown to be a good choice for the fabrication of thin-film electrolytes for ASSBs. Glassy LiPON thin-films can be deposited to desired substrates by magnetron sputtering of Li_3PO_4 in N_2 atmosphere. It has a poor ionic conductivity of $2.0 \cdot 10^{-6}$ - $3.3 \cdot 10^{-6}$ S/cm. Nevertheless, it can be applied as facile electrolyte material by reducing its film thickness, diminishing the internal resistances. Further, LiPON is characterized by a negligible reactivity against lithium and very low electrical conductivities of $8 \cdot 10^{-14}$ S/cm. [50,58,59].

2. Battery Manufacturing

2.1. Lithium-Ion Battery Electrode Fabrication

A significant drawback for the success of conventional LIBs in *e.g.* the electromobility sector and stationary energy storage applications, is their high production cost of <$1000/kWh [5,18,60,61]. To store renewable energy without government subsidy in stationary LIB systems, Cho *et al.* reported that the cost must be lower than $200/kWh [5]. Nevertheless, based on a cost projection of intercalation-based state-of-the-art LIBs, Berckmans *et al.* predicted that a price threshold of $100/kWh will be achieved until 2025-2030. A great contribution to the cost reduction will be the forecasted growth of the electric and hybrid electric vehicle market (factor of 52 until 2030), and the accompanied investments in battery manufacturing that will lead to a mass-manufacturing situation [62]. These drops in battery costs are essentially based on innovations in LIB fabrication itself [18,61,63–65].

In LIB manufacturing, battery-cell architectures and designs include cylindrical cells, pouch-cells and prismatic cells [66]. Independent of battery-cell design, conventional LIB-cell manufacturing comprises three major steps: electrode preparation, battery-cell assembly, and formation and aging [61,62]. Among them, the electrode construction is often considered as the most complex and labor-intensive step [67–69]. In fact, LIB electrode fabrication contributes to more than 50% of the overall LIB production costs, mostly due to the expensive active materials [61,62].

Starting with purchased electrode active materials, conventional LIB electrode fabrication involves: (1) slurry production in which an electrode active material, carbon additive (enhances electrical conductivity) and binder (improves intrinsic mechanical stability of composite layer and its adhesion to current collector) are mixed and fabricated into a paste by means of a solvent, (2) doctor blading of the paste on a current collector, (3) drying of the coated layer to remove the solvent, and (4) calendering of the dried composite layer to enhance electrical connections within the electrode and to the current collector. The electrodes are (5) slit to width and (6) dried for a final time to remove humidity, prior to battery-cell production in water-free atmosphere [23,61,62,67]. The individual processing steps and the required components, as well as the anticipated electrode and battery-cell properties, were comprehensively described by Kwade *et al.* [61]. Significant economic progress has been made by fine-tuning the slurry-based electrode production process [69–73]. However, further innovations in electrode processing are required to accommodate the aim of $100/kWh in 2030 [62].

The autonomous synthesis of the active materials using cost-efficient synthesis processes and low-cost precursors, instead of purchasing industrial products, may lead to reductions in electrode fabrication cost. Also the *in-situ* functionalization of the active materials with conductive and binding additives may enhance the production process cost-efficiency.

2.2. Flame Spray Pyrolysis-Synthesized Active Materials

Electrode active materials for LIBs can be synthesized from a variety of techniques. As it was previously indicated for LTO, it is important to reduce active material particle sizes and to carbon-functionalize them for obtaining proper electrode performances. Prominent approaches to obtain carbon-functionalized nano-sized LTO involve solid-state, sol-gel, and hydrothermal synthesis methods, as comprehensively summarized by Yi *et al.* and Sun *et al.* [31,74]. Assembled in LIBs, such LTO composite electrodes showed high rate capabilities with long cycle life. However, these techniques often suffered from tedious multistep processing protocols, including thermal post-treatments with long time and high energy consumption, eventually, ballooning the process cost. In addition, the nature of the carbon species and its distribution was difficult to control.

Flame spray pyrolysis (FSP) is a flame aerosol synthesis technique, known for the reproducible and scalable production of pure, crystalline and uniform oxide nanoparticles with a narrow size distribution. Based on these unique properties, FSP has substantially contributed to the development of new and sophisticated materials for catalysis, optics, photonics, sensors, health care, and more [75–87]. FSP has also recently emerged as a powerful tool for battery electrode material synthesis, as shown for LMO [88], LTO [89], and LFP [90,91]. Especially, its scalability to larger units with high production volumes, makes FSP highly relevant for industrial battery production [32,88–90,92–101].

Principally, the materials in flame aerosol synthesis are produced in the gas-phase, similar to chemical vapor deposition, physical vapor deposition and spray pyrolysis methods [102]. Unlike such techniques, flame aerosol synthesis of particles is independent of an external energy source for precursor conversion such as plasmas, lasers or electrically heated walls, which increases the cost-efficiency of the process. The existing flame aerosol synthesis processes are distinguished based on the state of supplied precursor, *i.e.* vapor-fed or liquid-fed. While they have a clearly higher precursor availability at reasonable cost, liquid precursors turned out to be much more versatile in product synthesis than volatile precursors [102].

In FSP, a liquid precursor mixture of organic solvents and metal organic precursors is atomized by means of conventional air-assisted or ultrasonic nozzles, resulting in fine droplets [78,102]. Since the applied precursor solutions are required to have a high enthalpy-density, it is sufficient to disperse the fine aerosol droplets into a small pilot flame to ignite the spray and sustain combustion [102]. During droplet combustion in the flame spray, nanoparticles are formed based on evaporation, nucleation, surface growth, coagulation, and coalescence at temperatures ≥2000°C. The particle formation parameters are directly influenced by the thermal energy flux, the related temperature profile and the residence time of particles in the high temperature region. Ensuing nanoparticle formation, the aerosol stream is rapidly quenched after exiting the flame. The particles are collected by means of a vacuum pump on an ultra-finely-woven, but air-permeable, glass- or metal-fiber collecting unit. Alternatively, the aerosol can be *in-situ* deposited as porous films on air-impermeable substrates [78].

The rapid quenching allows the formation of homogeneous and crystalline materials and can even lead to the preservation of thermodynamically metastable phases that are difficult to obtain *via* conventional wet-phase or calcination techniques [86,102]. The specific surface area of the product powder can be controlled by varying the liquid precursor feed rate or the oxygen dispersion gas rate in the nozzle. Both parameters directly affect the flame height and, therewith, the high temperature particle residence time [78]. Through a combination of two FSP-reactors, called double flame spay pyrolysis (DFSP), the material design becomes even more versatile. Composite materials with tuned properties (composition, doping, sizes) are realizable by individual control of the respective flame parameters [79,80,88,102–111].

2.3. Flame Spray Pyrolysis-Synthesized $Li_4Ti_5O_{12}$

Various groups have attempted to synthesize phase-pure and nanoparticular LTO *via* FSP using different precursor solvent combinations, resulting in different physicochemical and electrochemical properties [32,89,92,93,95–98,112]. Ernst *et al.* prepared a LTO precursor solution by blending lithium *tert*-butoxide (LTB) dissolved in tetrahydrofuran (THF) and titanium *tert*-isopropoxide (TTIP) mixed with xylene, in a molar Li/Ti ratio of 0.8 and final metal concentration of 1.65 M. After FSP synthesis, the nano-sized (d_{XRD}=21 nm) LTO powder showed a LTO phase purity of 85 wt%. Electrochemical measurements were not reported [89]. Karhunen *et al.* reported the first phase-pure ultra-fine (d_{XRD}=9.9 nm) LTO synthesis *via* FSP by mixing lithium acetylacetonate (LAA) and TTIP, both dissolved in an equal volume mixture of toluene and 2-ethyl hexanoic acid (EHA), in a stoichiometric ratio of 4 to 5 and a metal concentration of 0.5 M. Electrochemical measurements were not presented [112]. Bresser *et al.* synthesized nano-sized (d_{XRD}=20-30 nm) LTO particles with phase impurities. The amount of impurities was significantly reduced after a thermal post treatment at 800°C, accompanied by particle growth (d_{XRD}=1000-2000 nm). The nano- and micro-LTO powders were galvanostatically cycled in LIB half-cells and revealed significantly enhanced rate capabilities for nano-sized LTO. Along with excellent coulombic efficiencies of ≥99.9%, the nanostructuring of the LTO powder entailed significant improvements in dis-/charge kinetics *e.g.* due to shorting of lithium-ion and electron diffusion pathways [32]. Kim *et al.* synthesized nano-structured (d_{TEM}=23 nm) LTO powders from a 0.5 M spray solution consisting of TTIP and lithium nitrate (LNT) with 15% lithium excess, dissolved in a mixture of ethyl alcohol and distilled water. The LTO powder still had impurities (unquantified) after thermal post-treatments of 600 and 700°C which, however, disappeared after calcining at 800°C. Increasing the calcination temperature, led to reductions in initial irreversible capacity losses, attributed to increasing phase purity and particle growth (submicron-sized). Despite slight rutile impurities, nano-sized LTO (d_{TEM}=47 nm) calcined at 700°C showed higher discharge capacities than pure micron-sized LTO (d_{TEM}=23 nm). While cycling occurred at a relatively low rate of 0.1C, this indicated the beneficial effect of particle size reduction on the electrode performance of LTO. Birrozzi *et al.* synthesized four nano-sized (d_{SEM}≤20 nm) LTO batches *via* up-scaled FSP, using different precursor solvent combinations. Either lithium acetate dihydrate or lithium hydroxide, and titanium *tert*-2-ethylhexanoate were applied as lithium and titanium precursors, respectively. They were mixed in organic solvents of either pure methanol or, a mixture of xylene, acetonitrile, acetic acid, and ethanol (EtOH). All four samples contained traces of impurities whereas the highest LTO purity of 86 wt% was obtained by using the variable components lithium acetate dihydrate and methanol in a lithium/titanium ratio of 4 to 6. Applying carboxymethyl cellulose as binder, and copper as current collector, resulted in specific discharge capacities of 133, 131,129, 127, 124, and 115 mAh/g for C-rates of 1C, 2C, 5C, 10C, 20C, and 50C, respectively [92]. Kavan *et al.* reported that LTO particles sizes below 20 nm experienced increased stress, induced by mutual lithium-ion repulsion during de-/intercalation processes. This in turn led to a drop in diffusion coefficient by orders of magnitudes. Depending on the dis-/charge rates, Kavan *et al.* suggested LTO particle sizes of 20-80 nm as most robust and suitable to meet the requirements in high rate capability [95]. To improve the performance of FSP-synthesized LTO particles, Karhunen *et al.* implemented the particle size concept and refined their previous FSP setup [112] by mounting a vertical tube flow oven in the down-stream direction of the reactor. The heating element was used to prolong the high temperature particle residence time. The LTO phase had TiO_2-impurities (10 wt%), enhanced crystallinity and increased particle sizes, *i.e.* ~40 nm. Upon rate testing, it has been shown that the LTO particles with enlarged particle sizes were roughly matching the performance of a commercial LTO sample up to a rate of 5C. At 10C, however, the synthesized LTO sample showed superior specific capacities which was ascribed to the "still" relatively short diffusion path lengths [93].

The previous reports demonstrate the facile synthesis of crystalline LTO nanoparticles *via* FSP. Obtaining phase-pure material was difficult in some cases. FSP-synthesized nano-LTO showed enhanced power capabilities in LIBs compared to conventional micron-sized LTO. This was attributed to the increased lithium-ion diffusion coefficients in smaller particle sizes. It was also shown that deceeding a critical value can be adverse either.

Additional improvements in high power capability can be obtained by carbon-functionalization of nano-sized LTO particles. The feasibility of producing carbon-functionalized platinum clusters *via* FSP has been illustrated by Ernst *et al.* [113]. *In-situ* carbon-functionalization of the platinum clusters has been carried out in two possible ways: first by, dissolving the platinum precursor in xylene and spraying the solution at under-ventilated conditions to obtain carbon from incomplete combustion, and second, by using DFSP, with one carbon and one platinum cluster solution, of which the aerosol streams were intersecting in one point, leading to physical mixing of carbon and platinum clusters [113].

2.4. Flexible Thin-Film Battery Fabrication

Similar to LIBs, the successful market implementation of ASSBs will require a mass production situation. Disregarding all the diverse electrochemical stability and performance challenges, the processability and manufacturing costs for high-quality solid-state electrolyte materials have to reach a comparable level to conventional LIBs. Highly automated, continuous and scalable production routes with high throughput are inevitable. A direct transfer of laboratory preparation techniques to industrial scale is, however, infeasible yet. The approaches for large-scale format solid-state electrolyte production are few, including wet-coating, screen-printing, and tape casting techniques. Up-scaling of required materials, as well as the mass reduction of inactive components, are of major importance for realizing industrial-scale fabrication of ASSBs [22,23].

Next to the production of bulk-type ASSBs, the fabrication of micro-sized and/or flexible ASSBs requires customized manufacturing processes. One of the currently most promising approaches to realize leak-proof, light-weight and efficient miniaturized ASSBs, is the fabrication of all-solid-state two-dimensional thin-film LIBs with overall thicknesses of less than 20 μm [3,4]. If deposited on thin polymer sheets, the fabrication of mechanically flexible thin-film ASSBs cells, *i.e.* flex-TFBs, becomes viable [114]. To reduce resulting overpotentials in the pure electrode thin-films due to long diffusion pathways, the functional layer thicknesses are limited to a few microns. Advantageously, the fabrication process of flex-TFBs is thus independent of compositing electrode active materials with conductive and binding additives. Excluding these additives, diminishes the overall ASSB cell production costs and increases the energy density [3,4]. Despite all these striking advantages and encouraging prospects, the technological possibilities for the large-scale production of flex-TFBs are limited. This is due to the complicated formation process of both the solid-state electrolytes and the flexible thin-film electrodes.

Two famous approaches for preparing high quality thin-film electrodes (independent of substrate and electrolyte type) are magnetron sputtering and pulsed laser deposition [1]. Magnetron sputtering and pulsed laser deposition are high-vacuum-based physical vapor deposition methods, in which the desired materials are ablated and deposited onto given substrates *via* ion-bombardment or high-intensity laser radiation, respectively [10]. While both methods are capable of preparing uniform and dense thin-film electrodes with proper electrochemical performance, the obtained thin-films are generally amorphous. Due to reports on the obstructive effect of imperfections in a crystal structure to lithium-ion diffusion, crystalline active materials are often preferred [11]. To effectively crystallize electrode thin-films, derived from magnetron sputtering or pulsed laser deposition, heating steps above 500°C or more are required during or after the synthesis, as shown *e.g.* for LTO [12–16], LCO [17,18], LFP [19,20], or LMO-based electrodes [21,22]. Heating steps, however, may destroy flexible substrates which are mostly temperature-sensitive. Koo *et al.* [11] reported a successful strategy to produce crystalline electrode active material thin-films on flexible substrates for flex-TFBs. Amorphous LCO was sputtered onto heat-resilient sacrificial mica substrates. High-temperature post-treatment resulted in LCO crystallization. LiPON and lithium were deposited on top before the mica was removed layer by layer using a sticky tape. Subsequently, the battery-cell was transferred to a flexible Polydimethylsiloxan substrate [11,32]. Eventually, the battery-cell provided a capacity of 106 µAh/cm², but involved complex multistep processing.

2.5. Flexible Thin-Film Electrode Fabrication *via* Flame Spray Pyrolysis

The fabrication of flexible LTO electrodes was, hitherto, focused on rather thick electrodes for liquid-electrolyte based LIB cells [24–30]. Still, polycrystalline LTO thin-film electrodes have been successfully produced on temperature-resilient silicon-based substrates, after either (1) pre-heating of substrates (*e.g.* radio-frequency sputtering at 500-700 °C [12], direct current sputtering at 600°C [13], plasma laser deposition at 650°C [14]), or (2) post-annealing of the deposited thin-films (PLD at 700°C [15,16]). However, such high process temperatures (≥500°C) exclude the use of flexible polymer substrates due to their low decomposition temperatures [3,31]. Consequently, innovative approaches for deposition of crystalline electrode materials to flexible temperature-sensitive substrates are required to realize LTO flex-TFBs.

According to the knowledge presented previously, FSP is a useful tool (1) for the synthesis of electroactive crystalline nanoparticles of homogeneous sizes, shapes, and high purities, and (2) in combination with a compression technique, for producing electrode active material films with controlled porosities [96,97]. The FSP-typical residual porosities may in fact be of advantage: as indicated earlier, the arising mechanical stresses during cycling in high voltage cathode materials such as LMO or LCO, lead to electrode pulverization and related contact losses [115]. Since electrical and ionic conductivities in flex-TFB electrodes are solely dependent on the intrinsic electrode contact area, it is very important to mitigate the effect of undesired volume expansion upon cycling. Introducing a controlled layer porosity as present in compressed FSP-layers, may thus beneficially act as a buffer for internal stresses from lithium de-/intercalation. A reasonable porosity would lie between exaggerated high porosities, which would result in poor charge transport, and, extremely low porosities that are prone to mechanical electrode pulverization [115]. The direct FSP deposition of polycrystalline thin-films to temperature-sensitive flexible substrates has, to the best of the authors knowledge, not been reported yet. However, *in-situ* deposition of porous thin-films or micro-patterned layers for sensor applications with FSP was demonstrated [44–49]. Based on this, Chew *et al.*, presented a FSP *in-situ* deposition method to prepare electroactive nanostructured LMO electrode films (~7 μm) for LIBs. The LMO particles were directly deposited on cooled temperature-resilient substrates (<500°C) mounted directly above the flame. The films were post-annealed with a particle-free xylene-fed flame to improve adhesion and to prompt crystal growth [116].

2.6. Microstructural Simulations of Polydisperse Particle Layers

FSP-synthesized powders typically comprise aggregated nano-sized primary particles. Deposited as films, these layers exhibit porosities of up to 98.9% with a well-defined pore-size distribution [117,118]. Such high porosities are often accompanied by low mechanical resistance. Compression of such films was shown to improve the mechanical strength but also the electrical conductivity due to an increased number of electrical percolation paths. Microstructural simulations can help to understand the effect of compression to the restructuring of primary particles, aggregates and agglomerates. A model that is able to quantify compression-force-dependent changes in porosities and pore-size distributions, may serve as a prediction-tool for structure-related properties such as percolation, pore structure, heat transfer and electrical conductivity [118].

Discrete element method (DEM) simulations can provide dynamic information about particulate systems. The dynamic behavior of such systems is very complicated due to the complex interactions between individual particles and the surrounding gas, liquid, or walls. In DEM, a finite number of discrete particles are considered that are interacting by means of contact and non-contact forces, in which every considered particle has the possibility to move by translation or rotation [119]. Aggregates, in contrast to single primary particles, are able to rearrange *via* mutual detachment, rolling, or sliding events, in dependence to the prevailing non-covalent and humidity-related interactions. The existence of non-covalent particle-particle contact forces between aggregates has been previously shown [120–122]. The effect of compression on the mechanical strength of covalent sinter bridges between primary particles, was, however, difficult to determine.

In 2019, Baric *et al.* have pursued DEM simulations to understand the restructuring mechanisms of FSP-synthesized thin-films under applied loads. The investigated nanoparticle network comprised aggregated polydisperse and hydrophilic TiO_2 particles. They developed a novel sinter-bridge model which was able to correctly reproduce experimental porosities and pore size distributions upon mechanical compaction of FSP-synthesized aggregates [118]. This model may help to understand the correlation of an electrode microstructure and the related charge transport capabilities.

3. Contributions of This Work

3.1. Electrochemical Performance of High-Purity $Li_4Ti_5O_{12}$

FSP offers the autonomous, fast and efficient synthesis of nano-sized active materials with narrow particle size distributions, suitable for high rate applications. LTO is an interesting battery active material to fabricate LIBs with long cycle-life and high-rate capability. It is suitable for FSP-synthesis, however, issues on phase purity were reported in a number of studies. To obtain the desired nanoscale LTO particles in a phase-pure state *via* FSP, the choice of precursors and solvents is crucial.

In this thesis, three high purity FSP-based LTO powders from different precursor solvent combinations were provided for electrochemical testing. It was hypothesized that the underlying precursor solvent combination was indifferent to the electrochemical performance of the LTO powder.

FSP-synthesized LTO powders were physicochemically investigated with X-ray diffraction (XRD), Brunauer-Emmett-Teller surface area analysis (BET), Thermogravimetric analysis with differential calorimetry and coupled mass-spectrometry (TGA-DSC-MS), and transmission electron microscopy

(TEM), before they were manufactured into electrodes *via* conventional doctor blading procedure. The electrodes were tested electrochemically in LIB half-cells using galvanostatic cycling with potential limitations (GCPL) at different rates and cyclic voltammetry (CV).

The validation of the hypothesis would enable the battery manufacturer to choose the most cost-efficient precursor materials for the FSP-synthesis of high-purity LTO. This is possibly true for any other given battery active material that can be synthesized with FSP.

3.2. Electrode Fabrication *via* DFSP/Transfer-Lamination

The carbon-functionalization of nano-sized active materials can lead to improved electrochemical performances. A binder-free synthesis process that allows a facile *in-situ* carbon-functionalization may contribute to increased energy densities and decreased LIB fabrication costs. Especially, the absence of a solvent will significantly decrease costs since energy-intensive electrode drying becomes redundant [61].

Based on DFSP, carbon-functionalized active material composites can be synthesized. Instead of applying high voltage cathode materials such as LMO that exert volume changes upon cycling (~6-7% [123]), zero-strain LTO may be a rewarding prototype material to study a binder-free process [96,97]. The phenomenological electrode integrity upon cycling may thus be investigated while any notable volume expansions are absent.

A binder-free and carbon-functionalized LTO composite (LTO/C) was synthesized *via* DFSP and fabricated into electrodes using a fast one-step transfer-lamination technique. Three batches of LTO/C electrodes were prepared by using different transfer-lamination pressures. It was hypothesized that increments in compression, lead to a stronger densification of the LTO/C electrode microstructures. Larger intrinsic contact areas, in turn, will enhance the LTO/C layers' electrical conductivity and, thus, their electrochemical performance.

The produced LTO/C composite powder was physicochemically investigated with XRD and TEM. The effect of transfer-lamination pressure on the microstructure, mechanical stability and electrochemical performance was investigated with scanning electron microscopy coupled with focused ion beam (SEM-FIB). To evaluate whether the avoidance of binders and solvents caused any beneficial or detrimental effects, the transfer-laminated layers were microstructurally and electrochemically (GCPL at different rates) compared to a batch of doctor bladed LTO/C electrodes.

A facile process without the need for binding-additives and solvents for paste fabrication will increase the energy density, cost-efficiency and environmental benignity of LIBs. Once the microstructural features and the electrochemical performance of transfer-laminated binder-free LTO/C electrodes is better understood, the technique could be applied for the synthesis of carbon-functionalized high-voltage cathode materials, to realize LIBs with large energy densities.

3.3. Polycrystalline Flexible $Li_4Ti_5O_{12}$ Thin-Film Electrode Fabrication

Electrode fabrication for flex-TFBs is complicated since the active materials often require heat-treatments for crystallization. The involved heat can cause thermal decomposition of temperature-sensitive flexible polymer substrates. FSP allows the direct deposition of active materials to a given substrate. It was hypothesized that FSP-produced crystalline particle thin-films can be directly deposited to flexible and temperature-sensitive polymer substrates. Thermal decomposition of the substrates will be avoided by active cooling of the sample holder. Assembled into flex-TFBs, electrodes will provide reversible capacities in flat and bent condition. Zero-strain LTO was applied as model material for flex-TFB electrode manufacturing. The absence of active material volume expansion upon cycling, will facilitate to study the effect of static cell-bending on the electrochemical performance of binder-free LTO thin-film electrodes. The fabricated LTO thin-film electrodes were mechanically consolidated *via* lamination-compression to reduce the ultra-high porosity [117] and to enhance their mechanical stability [124].

Assembled into flex-TFBs, the compressed electrodes were electrochemically tested *vs.* lithium with CV and GCPL at different rates. Topography and morphology of the compressed LTO films and the individual battery component layers were examined *via* laser-scanning-microscopy (LSM) and SEM-FIB, respectively. First scientific evidences on the cyclability of FSP-based LTO flex-TFBs in bent condition were collected.

This FSP-based *in-situ* deposition method, will constitute a technological alternative for the facile fabrication of flexible electrode production in the field of flexible ASSBs. The absence of any heating steps for LTO crystallization makes the process fast and simple, resulting in a cost-advantage to other thin-film deposition techniques.

3.4. Improved Utilization of Porous $Li_4Ti_5O_{12}$ Thin-Films

The electron and lithium-ion transfer in highly porous polydisperse LTO particle networks is restricted to the lithium-atomic sites in the LTO crystals [98]. A strong compression of such porous layers will hypothetically lead to reductions in residual porosity of LTO thin-films, causing larger interparticle contact areas. Additional diffusion pathways and increased LTO/Cu and LTO/LiPON interface contact areas will improve related conductivities, resulting in enhanced discharge capacities and practicable capacities [125].

To solely consider the effect of pressure on the practicable capacities, the FSP setup was optimized for LTO thin-film loading reproducibility. The produced LTO thin-films were compressed either at comparatively low or high pressures.

The two batches were probed for roughness, microstructure, layer thickness, and electrical sheet resistivity, using LSM, SEM-FIB, and Van der Pauw measurements, respectively. Assembled in flex-TFB cells, electrodes were electrochemically characterized *via* GCPL at distinct rates. DEM simulations were applied to derive information about porosities and pore size distributions, particle coordination number and particle contact densities at the LTO layer interfaces.

A better understanding of the relationship between microstructures and the electrochemical performance, will help to design flex-TFBs with long cycle life and enhanced energy and power densities.

II. Experimental

4. Methods and Materials

4.1. Flame Spray Pyrolysis Synthesis of $Li_4Ti_5O_{12}$

The lithium and titanium precursors were dissolved with adjusted metal concentrations of 0.5 M. **Fig. 4.1a** exemplarily illustrates LAA (97%, Sigma-Aldrich) and TTIP (97%, Sigma-Aldrich) individually dissolved in EHA (≥99%, Sigma-Aldrich). The two solutions were mixed in Li/Ti ratio of 4 to 5, resulting in a 0.5 M LTO solution (**Fig. 4.1b**). Loaded into a syringe (**Fig. 4.1c**), the solution was delivered to the FSP nozzle (highlighted by the yellow rectangle), at a rate of 5 mL/min. The LTO solution was dispersed with oxygen gas (5 L/min, pressure drop of 1.5 bar) into very fine droplets. The aerosol was promptly ignited by a pilot flame composed of methane (1.5 L/min) and oxygen (3.2 L/min) gas, resulting in droplet combustion and flame spray formation (**Fig. 4.1d**) [96–98]. The produced LTO nanoparticles were thermophoretically separated from the gas phase with a glass-fiber particle collector unit, using the suction effect of a vacuum pump. After quenching the flame, the white-bluish LTO particles were scratched off from the recovered particle collector (**Fig. 4.1e**) and sieved with a mesh size of 150 µm (**Fig. 4.1f**), to clean the product from glass-fiber residues.

Three LTO powders were previously prepared in a high-throughput screening by Meierhofer *et al.*, using three different precursor solvent combinations [96]. Since the electrochemical characterization of the LTO powders is part of the current dissertation, the underlying solution chemistry is shortly described in the following. The three precursor solutions comprised either LNT, LTB or LAA as the respective lithium precursors. LNT was dissolved in EtOH, while LTB and LAA were individually dissolved in EHA. TTIP served as the invariable titanium precursor and was in each case dissolved in EHA. The three final precursor solvent combinations were produced by mixing the lithium and titanium precursor solutions in the combinations of $LNT_{EtOH}+TTIP_{EHA}$, $LTB_{EHA}+TTIP_{EHA}$ and $LAA_{EHA}+TTIP_{EHA}$ in a Li/Ti ratio of 4 to 5. Based on their lithium-precursors, the produced LTO powders derived from $LNT_{EtOH}+TTIP_{EHA}$, $LTB_{EHA}+TTIP_{EHA}$ and $LAA_{EHA}+TTIP_{EHA}$, are further abbreviated as LTO_{LNT}, LTO_{LTB} and LTO_{LAA}, respectively.

Flex-TFBs were prepared from LTO_{LAA}, while a second batch of flex-TFBs was analogously prepared from a fourth precursor-solvent combination involving LAA dissolved in EHA, and TTIP mixed with xylene, *i.e.* $LAA_{EHA}+TTIP_{xylene}$ [96].

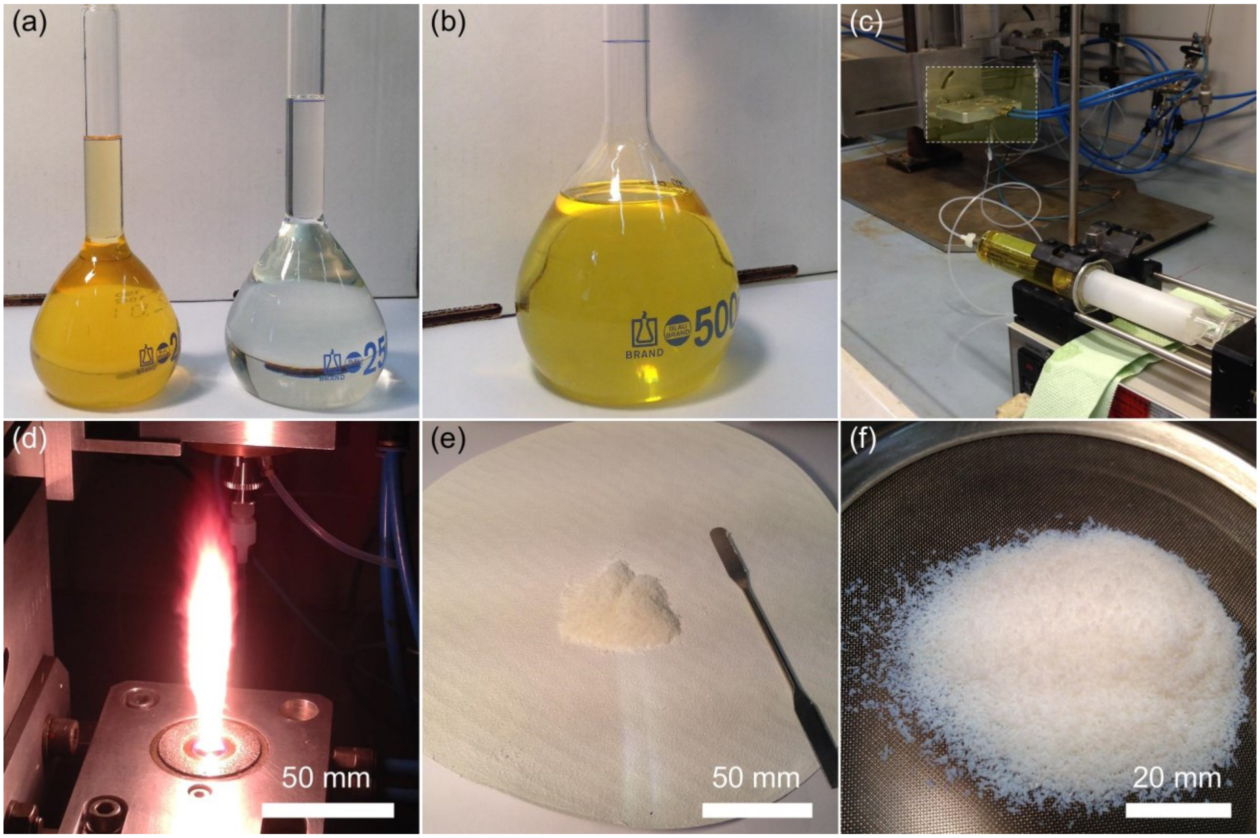

Fig. 4.1 LTO synthesis *via* FSP, **(a)** LAA (left, 200 mL) and TTIP (right, 250 mL), each dissolved in EHA, **(b)** lithium and titanium based solutions were mixed in a ratio of 4 to 5, providing the 450 mL LTO solution (LAA_{EHA}+$TTIP_{EHA}$), **(c)** LTO solution loaded in a 50 mL syringe, was delivered to the nozzle (highlighted in yellow) and **(d)** dispersed in a pilot flame resulting in the LTO flame spray, **(e)** After spraying, the collected LTO nanoparticles were scratched off from the recovered glass-fiber particle collector unit and **(f)** sieved to remove any glass-fiber residues.

4.2. Electrode Fabrication *via* Doctor Blading

LIB electrodes were prepared using a conventional doctor blading technique. The LTO powders, *i.e.* LTO_{LNT}, LTO_{LTB} and LTO_{LAA}, were each blended with a carbon additive (Super PLi, Timcal) and a polymeric binder (Polyvinylidene fluorid, PVDF, Kynar ADX111 Green, Timcal) in a ratio of 80:15:5 (wt%) (**Table 1**). The powder mixtures were ball-milled (Retsch, PM 100) for 30 min with a rotation speed of 400 rpm. To obtain a spreadable paste, the milling procedure was repeated, including N-methyl-2-pyrrolidon (NMP, C_5H_9NO, Roth) as solvent. Using a slit size of 90 µm and a velocity of 7.5 mm/s, the slurries were doctor bladed on copper foils (SE-CU58, hard type; 0.02 mm ± 10%, ~58 $m\Omega/mm^2$; surface treatment, IPC 4562A, Schlenk) using a Coatmaster 509 MC (Erichsen). The solvent was evaporated and the PVDF binder thermally activated by heating the electrode sheets subsequently at 80 (30 min) and 120°C (90 min), respectively. Quadratic 20x20 mm^2 pieces were punched out from the dried electrode sheets, serving as LTO electrodes. As shown in **Table 1**, the electrode loadings of

LTO_{LNT}, LTO_{LTB} and LTO_{LAA} were 7.1, 8.0 and 8.4 mg/cm², and the samples were calendered with line pressures of 75.0, 66.7 and 66.7 N/mm, respectively. As determined with a mechanical profilometer (Mahr Millimar C 1208), the three electrode types resulted in film thicknesses of 11, 12 and 13 µm, for LTO_{LNT}, LTO_{LTB} and LTO_{LAA}, respectively. Prior to LIB cell assembly in pouch-cells, the electrodes were vacuum dried overnight at 120°C and stored in an argon-filled glovebox (O_2, H_2O levels <0.1 ppm).

Table 1

Characteristics of manufactured electrodes (adapted with permissions of [96,97])

Sample	Electrode fabrication method	Active material: carbon:binder [wt%]	Doctor blade slit size [µm]	Loading per area [mg/cm²]	Calendering/ Lamination pressure	Film thickness [µm]
LTO_{LNT}	Doctor blading	80:15:05	90	7.1	75.0 N/mm†	11
LTO_{LTB}	Doctor blading	80:15:05	90	8.0	66.7 N/mm†	12
LTO_{LAA}	Doctor blading	80:15:05	90	8.4	66.7 N/mm†	13
LTO/C(1.5)	Lamination	75:25:00	-	1.7‡	1.5 N/mm²	23
LTO/C(2.6)	Lamination	75:25:00	-	1.4‡	2.6 N/mm²	26
LTO/C(3.3)	Lamination	75:25:00	-	1.7‡	3.3 N/mm²	23
LTO/C(DBap)	Doctor blading	69:23:08	60	1.5	-	11
LTO/C(DBc)	Doctor blading	69:23:08	60	1.5	92.3 N/mm†	8

† samples were calendered using a line-pressure

‡ total mass loading is affected by glass fiber residues due to lamination procedure

4.3. Electrode Fabrication *via* Pressure-Based Transfer-Lamination

A LTO/C composite with a composition of 75/25 (wt%) was produced using a DFSP setup (**Fig. 4.2a**). LTO_{LAA} was sprayed at standard conditions, while carbon was produced from a second flame spray, fed with xylene. To realize elemental carbon production, the oxygen in the xylene-fed flame spray was reduced to a minimum, causing incomplete carbon combustion. The nozzles of the LTO and carbon aerosol streams were facing at an angle of 20°, each. Accordingly, the particle streams were physically mixed at the intersection point before collection on a glass-fiber unit. The distance of the nozzles to the particle collector unit was 600 mm. The deep black LTO/C composite layers, still on the glass-fiber collecting unit, were cut into stripes and placed upside-down onto pieces of dendritic copper current collector foil. By means of two compressible parallel rollers (Hot role-to-role laminator HL-101, ChemInstruments), the LTO/C particle layers were transfer-laminated onto copper current collectors, followed by pull-off removal of the glass-fiber collecting units (**Fig. 4.2b**). Three individual transfer-lamination pressures were applied, *i.e.* 1.5, 2.6 and 3.3 MPa, further identified as LTO/C(1.5), LTO/C(2.6) and LTO/C(3.3), respectively (**Table 1**). The three transfer-laminated electrodes showed fairly similar loadings (1.4-1.7 mg/cm²) and film thicknesses (23-26 µm) [97].

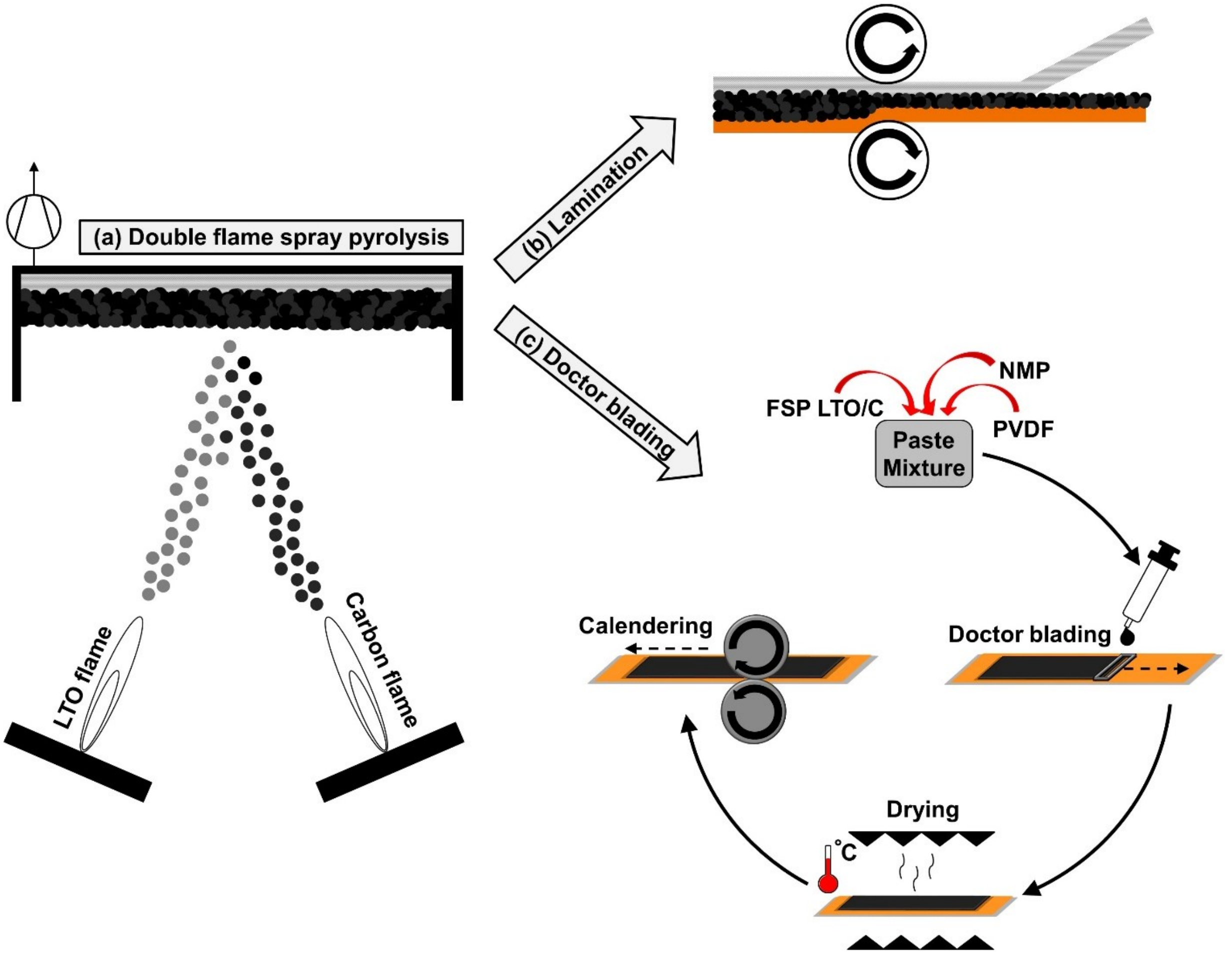

Fig. 4.2 LTO/C synthesis and electrode fabrication *via* transfer-lamination and doctor blading [97], **(a)** flame spray produced LTO and carbon aerosol streams were physically mixed prior to thermophoretical deposition on a glass-fiber filter, **(b)** the glass-fiber unit, along with the attached LTO/C particles, was placed upside down on a copper current collector. The LTO/C particle layer was transferred to the copper foil by means of two parallel pressurized rollers. The glass-fiber unit was removed, revealing the finished LTO/C electrode, **(c)** the LTO/C powder from the particle collector in (a), was scratched off and fabricated into a paste including NMP and PVDF. The paste was spread on a copper foil, dried, and in case of LTO/C(DBc), calendered (adapted with permission from [97]).

From the same LTO/C composite, electrodes were prepared by doctor blading technique. An illustration of the LTO/C doctor blading procedure, in direct comparison to the transfer-lamination technique, is presented in **Fig. 4.2c**. Since the LTO/C composite already contained carbon, only PVDF binder (Kynar ADX111 Green, Timcal) needed to be added in a LTO/C:PVDF ratio of

92:8 wt% (**Table 1**). The resulting paste was bladed with a slit size of 60 µm onto copper foil. One batch of the doctor bladed LTO/C electrodes was kept in as-prepared state, *i.e.* LTO/C(DBap). A second batch of the LTO/C electrode was subsequently calendered, *i.e.* LTO/C(DBc), with an application-related pressure of 100 N/mm. The film thicknesses of LTO/C(DBap) electrodes were 11 µm, which was three times less than for transfer-laminated electrodes (23-26 µm). Ensuing calendering, the film thicknesses of LTO/C(DBap) have further decreased to 8 µm for LTO/C(DBc) [97].

4.4. Pouch-Cell Assembly and Electrochemical Characterization

To electrochemically characterize the fabricated electrodes, they were assembled into battery pouch-cells. **Fig. 4.3a** shows an open polymer-coated aluminum pouch-cell, held in place with magnets for LIB half-cell fabrication.

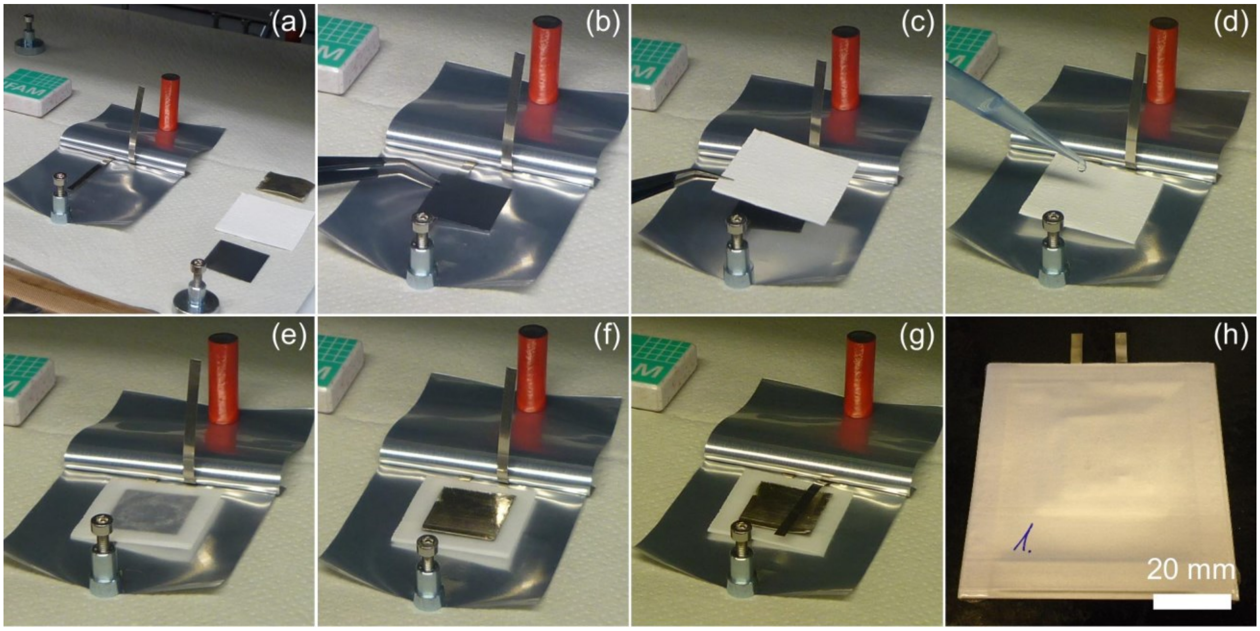

Fig. 4.3 (a) opened pouch-cell with a bent-down nickel arrester was loaded with **(b)** 20x20 mm^2 LTO electrode, **(c)** separator, **(d)** sprinkled and **(e)** soaked with liquid electrolyte, and **(f)** polished lithium foil, before **(g)** bending down the second nickel arrester and **(h)** vacuum-sealing the pouch-cell (adapted with permission from [96]).

Upon manufacturing, one of the two nickel arresters was bent down and the LTO electrode, with the copper-side facing downwards, was placed on top (**Fig. 4.3b**). A glass-fiber separator (30x30 mm^2, Whatman GF/A, **Fig. 4.3c**), sprinkled (**Fig. 4.3d**) and soaked with 350 µL 1M LiPF6 in EC/DEC 50/50 (v/v) electrolyte (MERCK, **Fig. 4.3e**), a polished lithium counter electrode (20x20x0.38 mm^3, **Fig. 4.3f**) and a piece of copper foil (20x20 mm^2, not shown), were stacked on the LTO electrode before the second nickel arrester was bent down (**Fig. 4.3g**). Finally, the three edges of the pouch-cells were vacuum-sealed at a final pressure of 10 mbar (**Fig. 4.3h**) [96,97].

4.5. Thin-Film Electrode Fabrication by Direct Layer Deposition

Nanostructured LTO particles were synthesized from LAA$_{EHA}$+TTIP$_{EHA}$ at standard conditions, using the single-nozzle FSP setup. The particle downstream was directed to a water-cooled copper block sample holder, mounted 320 mm vertically above the nozzle. Mechanically flexible polyimide foils (Kapton® 300HN, 20x20 mm^2, 75 µm thickness, DuPont) served as the LTO substrates. In an argon filled glovebox (O_2, H_2O levels <0.1 ppm), the flexible foils were coated with custom-made copper current collectors (~150 nm, Ø=10 mm), using a radio-frequency sputtering method with argon processing gas and a 4" copper target [55,98,126]. The copper-coated polyimide substrates are further denoted as "KaCu". A custom-made shadow mask was designed to fix four samples, exposing only the circular part of the copper current collectors (**Fig. 4.4a**) for particle deposition.

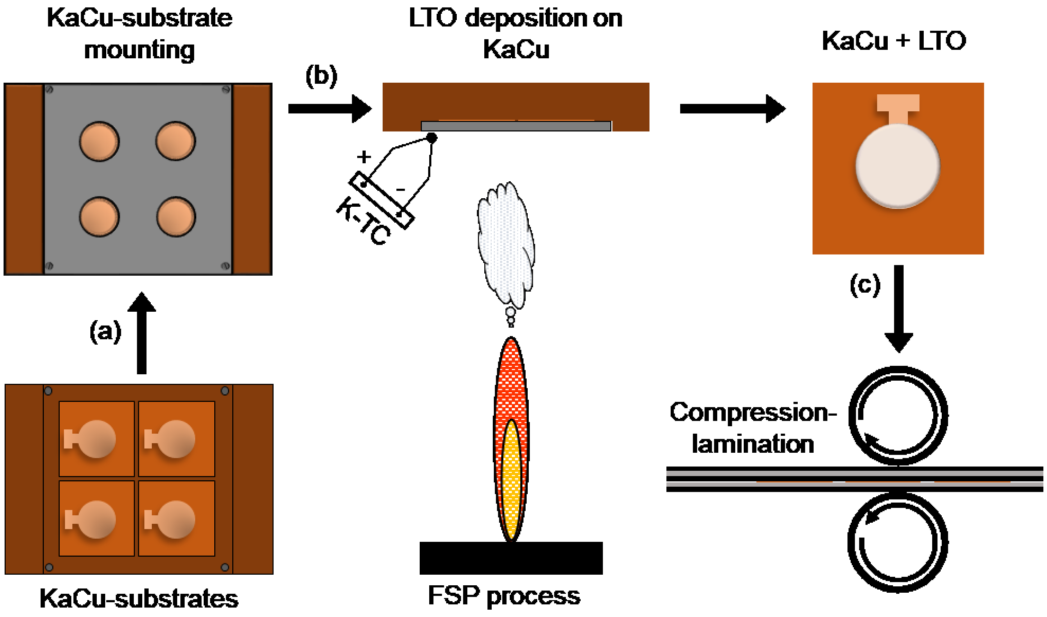

Fig. 4.4 LTO flex-TFB preparation *via* FSP and lamination-compression, **(a)** four KaCu substrates were mounted on a water-cooled copper sample holder and fixed with a shadow mask, exposing only the copper for particle deposition, **(b)** loaded sample holder was mounted in FSP reactor where the LTO particle thin-films (Ø=10 mm) were deposited onto the substrates. The *in-operando* deposition temperature was determined with a k-type thermocouple (K-TC), **(c)** the recovered coated substrates were compacted *via* lamination-compression (adapted with permission from [98]).

The flame spray, emerging from the combustion of 20 mL of LTO solution, was directed to the KaCu substrates, coating them with thin LTO layers (**Fig. 4.4b**). The deposition temperature was determined with a Pt/Rh thermocouple (K-type, Voltcraft K202). The temperature at the vicinity of the KaCu substrates and at the backside of the substrates (within copper block) was 200-230°C and 65-80°C, respectively. The excess LTO particles that passed the *in-situ* holder, were collected on the glass-fiber filter unit (600 mm above the nozzle) for further characterization. The as-deposited highly porous LTO electrodes were removed from the reactor and mechanically compressed to increase the physical contact and adhesion between LTO particle layers and substrates (**Fig. 4.4c**). Unlike to the transfer-lamination procedure of LTO/C composite layers, the lamination instrument was applied for compression, *i.e.* "lamination-compression", of LTO thin-films. During lamination-compression, the electrodes were embedded in the sequence of rubber/steel, LTO electrode, polytetrafluorethylen (PTFE), rubber/steel/rubber, to provide an equal pressure distribution. The PTFE tape (60 µm), directly placed on the LTO thin-film, was indispensable to avoid partial detachment of the weakly adhered LTO particles. Lamination-compression was carried out at room temperature with a pressure of 3.3 MPa, *i.e.* LTO(3.3), and a velocity of 7.5 mm/s [98,124,125]. LTO electrode loadings were determined by weighing the electrodes before and after LTO deposition and showed significant variations from 13 to 29 µg (20.4 ± 6.2 µg).

4.6. Pressure-Dependent Thin-Film Electrode Optimization

A new batch of porous LTO thin-film electrodes was prepared to understand the impact of low and high pressures on their morphological and electrochemical properties. To obtain 100% phase purity, LTO was synthesized by spraying a 0.5 M LTO solution prepared from $\mathrm{LAA_{EHA}}$+$\mathrm{TTIP_{xylene}}$. The four KaCu substrates (**Fig. 4.5a**) were placed on the water-cooled copper substrate holder. A newly prepared shadow mask (**Fig. 4.5b**) was applied to enhance LTO thin-film loading reproducibility. The modified shadow mask design (2 mm thickness) exhibited hole sizes of 9 mm that were conically edged at 45°, to ensure copper support for LTO thin-films, and to reduce shadow effects in vicinity of the hole edges, respectively. The sample holder was mounted into the FSP reactor and a laser pointer device was utilized to vertically align both the nozzle (**Fig. 4.5c**) and the electrode holder (**Fig. 4.5d**). The horizontal alignment of the substrates was controlled using a bubble level. The sprayed solution volume for LTO deposition was set to 42 mL to reduce the relative error in LTO loading statistics (cf. **section 4.5.**). When starting and stopping the FSP *in-situ* deposition process, the flame spray (**Fig. 4.5e**) was occasionally burning inhomogeneously. To obtain reproducibility, the substrates were shielded from the first and last sprayed milliliters. Thus, LTO thin-films (**Fig. 4.5f**) were effectively deposited from the combustion of 40 mL LTO solution [126].

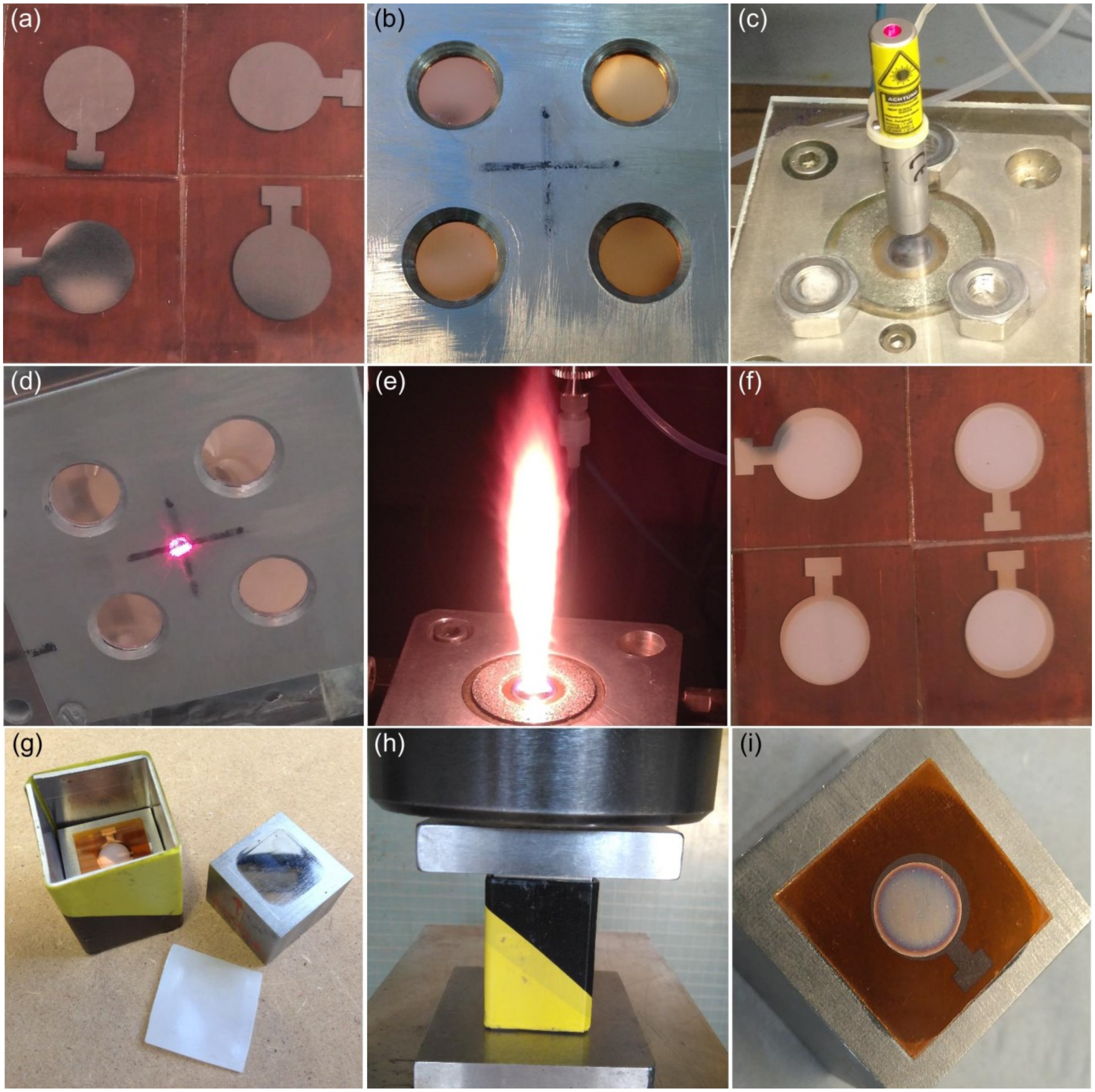

Fig. 4.5 Crystalline LTO thin-film production and compression. The deposition of LTO was pursued on 20x20 mm²-sized custom made **(a)** KaCu substrates ($Ø_{Cu}$=10 mm) that were fixed using **(b)** a steel shadow mask with conical holes of 9 mm diameter, **(c)** a laser pointer was applied for nozzle alignment directly below the center of the **(d)** mounted shadow mask, loaded with KaCu electrodes, **(e)** flame aerosol particle production occurred with flame height of ~10 mm, **(f)** fabricated LTO(ap) thin-films attached to the KaCu substrates, after detachment of shadow mask, **(g)** LTO(ap) electrodes were placed, covered with a piece of PTFE foil, between two polished $42CrMo_4$ steel cubes, encased with a metal frame for uniaxial compression, **(h)** uniaxial compression using 300 MPa pressure, **(i)** successfully compressed LTO(300) film on KaCu. Dark spots on copper in *e.g.* (a,d) were due to reflections in the mirror-like metal surfaces (adapted with permission from [126]).

Two LTO thin-film electrode batches were prepared using different compression forces. One batch of LTO(ap) thin-films was compressed using lamination-compression at 3.4 MPa, *i.e.* LTO(3.4). The other batch was compressed with an uniaxial press, applying 300 MPa, *i.e.* LTO(300). For the latter, two polished $42CrMo_4$-cubes (28x28x25 mm^3) were used for uniaxial compression, to reduce possible artifacts upon compression (**Fig. 4.5g**). The PTFE tape (60 µm), which was used for lamination-compression, was avoided due to its stability failure under high mechanical loads. Instead, pieces of more stable PTFE foils (250 µm) were applied. Uniaxial compression was carried out in a metal frame, tightly encompassing all the components, to prevent lateral dislocations and associated film detachment during pressure application. The bottom cube, LTO(ap) electrode, PTFE foil, and top cube, were carefully inserted inside the metal frame, followed by uniaxial compression at 300 MPa (**Fig. 4.5h**) for five seconds. **Fig. 4.5i** shows a LTO(300) thin-film located within the perimeter of the underlying copper current collector. Therefore, overall LTO thin-film particles were electrically supported [126].

4.7. Flexible Thin-Film Battery Assembly

To prepare flex-TFBs, the compressed LTO thin-film electrodes were inserted in an argon-filled glovebox (O_2, H_2O levels <0.1 ppm) (**Fig. 4.6a**).

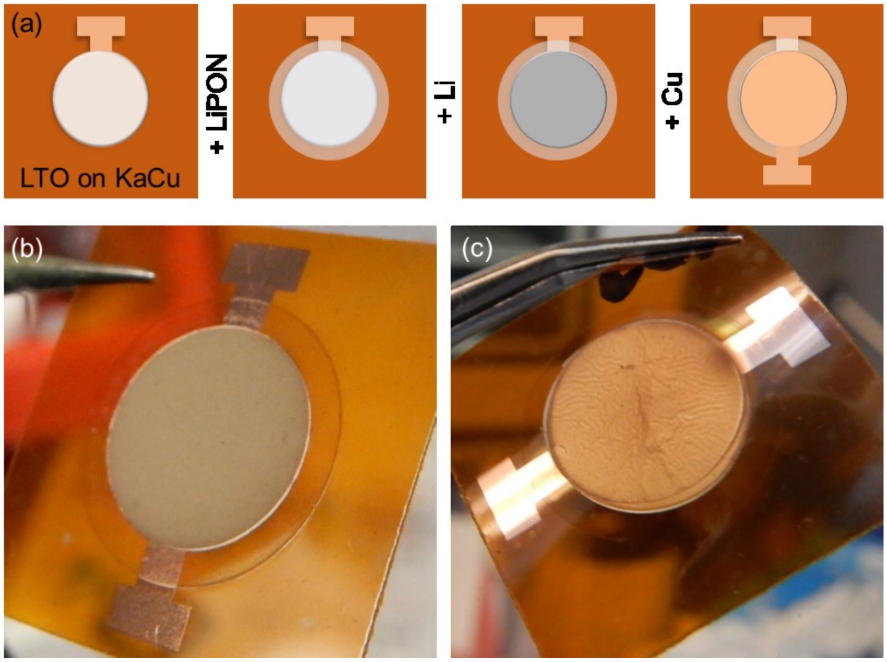

Fig. 4.6 **(a)** Within an argon-filled glovebox, the deposited and compressed LTO layers were subsequently coated with LiPON (Ø=13 mm), lithium and copper layers (each Ø=10 mm), resulting in **(b)** finished LTO flex-TFB cells, **(c)** uncompressed LTO(ap) electrodes were inapplicable for flex-TFB assembly due to weak mechanical adhesion.

LiPON was applied as model-type solid-state electrolyte to study the performance of the compressed LTO thin-films in ASSBs. The LiPON thin-films (~1.5 µm, Ø=13 mm) were sputtered on top of the LTO layers, using a 4" Li_3PO_4 target and N_2-processing-gas. The metallic lithium counter electrodes (~2 µm, Ø=10 mm) and copper current collectors (~150 nm, Ø=10 mm), were deposited by thermal flash evaporation and sputtering, respectively [55,98,126]. An exemplary flex-TFB, ready for electrochemical characterization, is shown in **Fig. 4.6b**. As side note, flex-TFBs that were assembled from uncompressed LTO thin-film electrodes, showed great mechanically instability and resulted inevitably in short circuiting (**Fig. 4.6c**).

5. Physicochemical Property Characterization

5.1. X-ray Diffraction

The LTO crystal structure properties were characterized using a MiniFlex600 (Rigaku) XRD diffractometer configured for Bragg-Brentano geometry. The instrument was equipped with a Cu(K_α)-source, primary and secondary Soller slit (2.5°), receiving slit (0.3 mm), fixed (1.25°) and variable divergence slit, and a scintillation counter detector (SC-70) with graphite monochromator. A continuous scan was carried out from 5-100°2θ with step size of 0.1°2θ and step duration of 20 seconds.

The LTO/C powder was characterized with a Bruker D-8 Advance with a Johannson-type primary monochromator, fixed divergence slit (0.29°), primary and secondary Soller slit, and a Lynxeye position-sensitive detector (3° aperture, 0.0156°/channel). The scan was carried out from 15°–100°2θ.

Rietveld refinement on the measured XRD data has been carried out using "BRASS"-program, to obtain information on crystalline powder composition, LTO unit cell parameters, density, and particle size. Contributions of the diffractometer to peak broadening were considered by implementing the instrumental parameters of crystalline LaB_6. The background parameters, sample displacement, scale factor, unit cell parameters, isotropic and anisotropic Gaussian and Lorentzian peak width parameters, as well as overall temperature factor were simultaneously refined for convergence. Rietveld refinement quality was evaluated based on the residual factors (R-factors). Volume weighted average crystallite sizes (d_{XRD}) were determined based on a line broadening analysis (Scherrer formula) [96–98,126–129].

5.2. Nitrogen Adsorption Experiments

Specific surface area analysis and average particle size of LTO (d_{BET}) were determined using nitrogen adsorption in a Quantachrome NOVA 4000e gas sorption system [130]. The LTO powders were degassed for three hours at 200°C in vacuum, followed by a five-point measurement (P/P_0-range: 0.1-0.3) in flowing nitrogen at 77°K (cooled by liquid nitrogen).

Specific surface area and pore structure of compressed LTO(300) and LTO(3.4) were obtained from nitrogen adsorption and desorption isotherms. While the LTO(300) mass deposited to the KaCu substrates was insufficient for gas adsorption experiments, LTO(300) pellets (Ø=10 mm, 125 mg) were produced at 300 MPa, using uniaxial compression (**Fig. 5.1**). The pellets served as viable analogue to study the porosities and pore size distributions of LTO(300) electrodes. For pellet production, a die was top-loaded with a circular blank Kapton® sheet, LTO powder, PTFE foil (250 µm) and the top cylinder, to resemble similar conditions to LTO thin-film compression on KaCu substrates.

The pellet procedure was inappropriate for low-compressed LTO(3.4) electrodes due to insufficient sensitivity of the press. Hence, additional LTO particles were synthesized from a larger LTO solution volume, *i.e.* 100 mL, *via* FSP. The loaded particle collector unit was cut into two segments and placed on top of each other, with the LTO-bearing faces inside. This set was compressed with 3.4 MPa *via* lamination-compression, resulting in a LTO(3.4) sandwich [126].

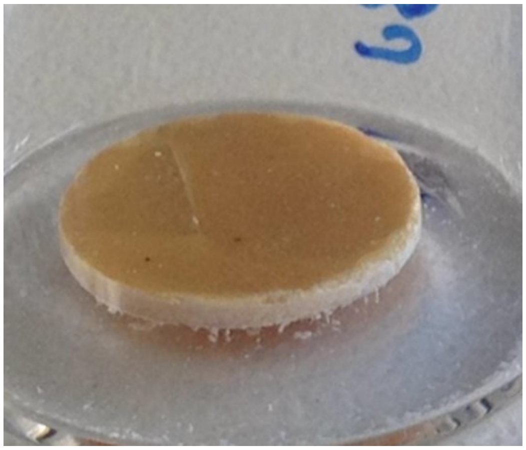

Fig. 5.1 LTO powder compressed at 300 MPa into 10 mm sized LTO(300) pellets (adapted with permission from [126]).

Pore structures of LTO(300) pellets and LTO(3.4) sandwich were determined from nitrogen adsorption and desorption isotherms using an Autosorb-1 (Quantachrome) [124]. After transferring the samples into the Autosorb-1, they were degassed for 24 hours, followed by recording the nitrogen adsorption and desorption isotherms (P/P_0 from 0.025 to 0.995). Pore size distributions were calculated from the desorption isotherm by applying the Barrett-Joyner-Halenda method [131]. The adsorption film thicknesses were derived from the t-curve method [126,132].

5.3. Thermogravimetric Analysis

Thermogravimetric characterization of LTO powders was carried out in air using a TGA-DSC, STA 449 F1 Jupiter® to investigate the amount of possible gaseous adsorbents. Approximately 8 mg of LTO powder were filled into Al_2O_3 crucibles. The samples were heated in synthetic air (Ar/O_2 4:1) at a rate of 5 K/min from 35 to 900°C. The evolving gases have been qualitatively characterized using a calibrated coupled mass spectrometer (TG/STA-QMS 403 D Aëolos®) [96,98].

5.4. Transmission Electron Microscopy

The LTO powder crystallinity and morphology was investigated, using a FEI Tecnai F20 S-TWIN TEM. The instrument was operated with an accelerating voltage of 200 kV using a field emission gun and a point resolution of 2.4 Å. The TEM images were recorded with a 1k slow-scan CCD camera integrated in a GATAN GIF2001 [97,98].

5.5. Scanning Electron Microscopy

The microstructure, thickness and interface morphologies of LTO thin-films and overall battery-cell components were investigated by preparing cross-sectional cuts *via* SEM-FIB (FEI Helios NanoLab™600 DualBeam™). To guard the layers from the ionic beam, a platinum patch was deposited on the LIB surfaces prior to ion-etching. Energy dispersive X-ray spectroscopy (EDX, Oxford X-Max 80 EDX SD-Detector) was applied to approximate the elemental distribution in the distinct battery-cell layers [97,98,126].

5.6. Laser Scanning Microscopy

The arithmetic surface roughnesses (R_a) of LTO(ap), LTO(300) and LTO(3.4) were determined using a LSM (VK-9700K, Keyence). A height profile was recorded and averaged R_a have been determined from at least six different surface-sections per sample [98,126].

5.7. Electrical Sheet Resistivities of Compressed $Li_4Ti_5O_{12}$ Thin-Films

Differences in electrical sheet resistivities of LTO(300) and LTO(3.4) were examined using Van der Pauw measurements at room temperature [133,134]. To determine the sheet resistivities, a current was applied to two diagonally opposite contacts while a resulting voltage was measured from the other two contacts. To prepare suitable samples, LTO(ap) films were prepared on bare Kapton®, using the *in-situ* FSP deposition setup. After either LTO(300) or LTO(3.4) film preparation, four equidistant copper squares (6x6 cm^2) were sputtered on the compressed films, serving as electrical contacts as shown in **Fig. 5.2** [126].

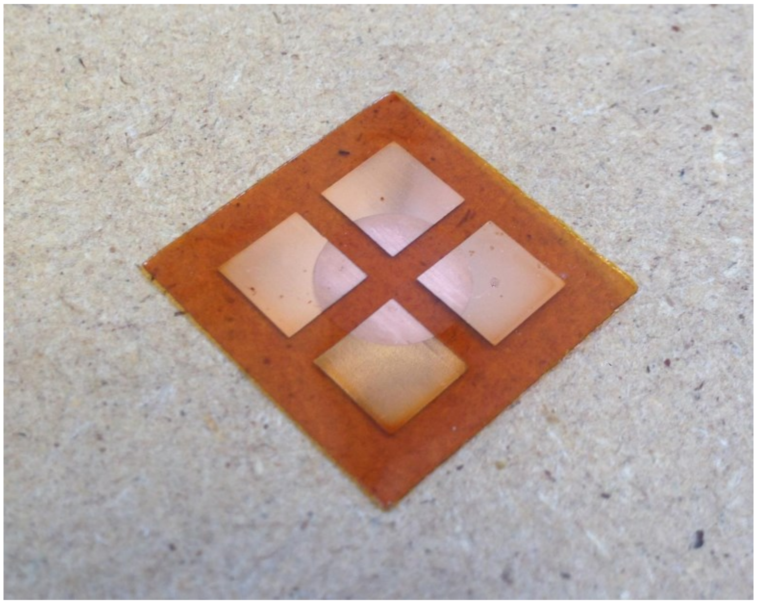

Fig. 5.2 Representative Kapton® substrate (20x20 mm²), deposited with LTO(300) or LTO(3.4) thin-films, and four sputtered copper contacts for electrical conductivity measurements. Copper rectangles showed alteration as the picture was taken weeks after preparation (adapted with permission from [126]).

5.8. Microstructural Simulation of Compressed $Li_4Ti_5O_{12}$ Thin-Films

The experimentally derived information on differently compressed microstructures such as film thicknesses, porosities and pore size distributions of LTO(3.4) and LTO(300), was compared to simulations of compressed polydisperse nanoparticular microstructures [126]. The LTO(ap) microstructure was simulated using DEM, considering 600,000 primary particles, configured in aggregates of typical 10-128 primary particles each, as typical for FSP-synthesized particles [118,126,135]. DEM simulations were carried out by Valentic Baric, IWT Bremen, using LIGGGHTS-PUBLIC v3.8 (https://github.com/UniHB-IWT/Liggghts-nano). Primary particle interactions within aggregates were modelled using the particle bond model of Potyondy and Cundall with a Young's Modulus and tensile/shear strength of 56 and 8 GPa, respectively [136]. The primary particles followed a size distribution of 3-23 nm for LTO [96]. Assuming that the interaction mechanisms are valid for all hydrophilic materials in this size range, unbonded particle interactions were computed using contact model described by Laube *et al.* [122] which was validated for FSP-synthesized TiO_2 nanoparticles [118,126].

After ballistic deposition of the aggregates in a 2.0x2.0x6.6 μm³ simulation box, the particle network films were continuously compacted at 0.5 m/s (periodic boundary conditions for lateral boundaries), using a static wall underneath and a movable compacting wall above the deposited particles. At the pressures of 3.4 or 300 MPa, the motion of the compacting wall was stopped to calculate the contact density of LTO particles with the walls. Subsequently, the compacting wall was lifted to fully relax the film for computing the porosity and pore size distribution of the unconstrained particle films. Further information about coordination numbers of LTO particles and contact densities to the interfaces was obtained [126].

6. Electrochemical Characterization

6.1. Galvanostatic Cycling with Potential Limitations

Cycle-dependent dis-/charge behavior of assembled LIB-cells and flex-TFBs was investigated with GCPL. Three LIB-cells per electrode batch were fabricated into pouch bags and tested galvanostatically at room temperature in a voltage window of 1.0-2.0 V (BaSyTec CTS-Lab-XL). LTO_{LNT}, LTO_{LTB} and LTO_{LAA} battery-cells were cycled for 450 cycles at 1C, where 1C corresponds to full dis-/charge of a battery-cells capacity in one hour. To cycle each battery-cell at 1C, the respective battery-cell capacity was determined by normalizing the LTO mass fraction within the electrode composite to the theoretical maximum capacity of LTO, *i.e.* 175 mAh/g. The capacity was implemented into the BaSyTec software to compute the current, required for fully dis-/charging a battery-cells capacity in one hour. Rate performances of the three batches, *i.e.* the reversible capacity at various currents of different magnitudes, were determined by applying various rates of C/5, C/2, 1C, 2C, 5C, 10C and 25C, immediately after cycling tests. Rate tests were always completed by repeating the first applied rate, to understand whether high-rate application led to irreversible capacity losses. Battery-cells fabricated from LTO/C(1.5), LTO/C(2.6) and LTO/C(3.3), as well as LTO/C(DBap) and LTO/C(DBc) were cycled at 1C for 200 cycles. Rate tests were performed at C/5, C/2, 1C, 2C, 5C, 10C and 25C [96,97].

Flex-TFB cells were investigated with the same BaSyTec system with potential limitations of 1.0-2.0 V. Flex-TFBs assembled from LTO(3.3) were galvanostatically cycled in flat condition for 30 cycles with 2 μA (1C) at room temperature to prove reversible cycling. One battery-cell was cycled for more than 200 cycles to evaluate long-term stability. Rate tests were performed at 1, 2, 4, 6 and 10 μA, corresponding to 0.5C, 1C, 2C, 3C and 5C, respectively, with four full-cycles at each rate. After cycling and rate testing in flat condition, two random battery-cells were bent (radius 7.5 mm) and cycled for 30 cycles, followed by 30 more cycles in flat condition. Cycling stability of flex-TFBs assembled from LTO(300) and LTO(3.4) were investigated with GCPL in flat condition at a current of 2 μA (C/5) at a constant temperature of 35°C. Rate tests were conducted at 2, 8, 16, 48, 96 and 2 μA, corresponding to C/5, C/2.5, 1.8C, 5.4C, 10.8C and C/5 (four full-cycles per rate), respectively. Long-term performances were examined using a 12 µA (1.3C) rate for additional 100 cycles, after rate testing [98,126].

6.2. Cyclic Voltammetry

Reaction kinetics of LIB-cells and flex-TFBs were characterized with CV. LIB-cells were tested with a Gamry reference 600 potentiostat using scan rates of 0.2, 0.5 and 1.0 mV/s in a potential window of 1.0-2.0 V [96,97]. Flex-TFBs were investigated using the same parameters, however, with a Biologic Potentiostat SP-300 (Science Instruments) [98,126].

III. Results and Discussion

7. Physicochemical Characterization of $Li_4Ti_5O_{12}$

7.1. X-ray Diffraction

The provided powders, *i.e.* LTO_{LNT}, LTO_{LTB} and LTO_{LAA} had high LTO phase purities of 94.4, 98.3 and 97.7 wt%, with particle sizes of 7.0, 6.4 and 6.4 nm, respectively, as shown by Meierhofer *et al.* [96]. In the current work, the three LTO powder batches were fabricated into LIB electrodes and electrochemically characterized in LIB half-cells. The LTO_{LAA} powder was reproduced in this work and crystallographically characterized as shown in **Fig. 7.1**. The Rietveld refinement proved that the LTO_{LAA} powder was predominantly composed of cubic spinel LTO (space group: *FD-3m*, ICSD 160655). The major reflections at 2θ of 18.7°, 35.8°, 43.5°, 47.6°, 57.5°, 63.2°, 66.4°, and 79.7° were assigned to the crystal planes (111), (113), (004), (133), (111), (044), (135), and (444), respectively [96,97]. Low intensity reflections at 26, 28 and 55°2θ indicated the presence of TiO_2 species. A convincing refinement for the impurity phases was, however, difficult due to the small area beneath. It was concluded that the LTO purity was ≥99 wt%. The Rietveld refinement revealed LTO unit cell parameters of 8.36 Å for a, b, c, and 90° for α, β, γ, with average crystallite size of 6 nm and a density of 3.48 g/cm³.

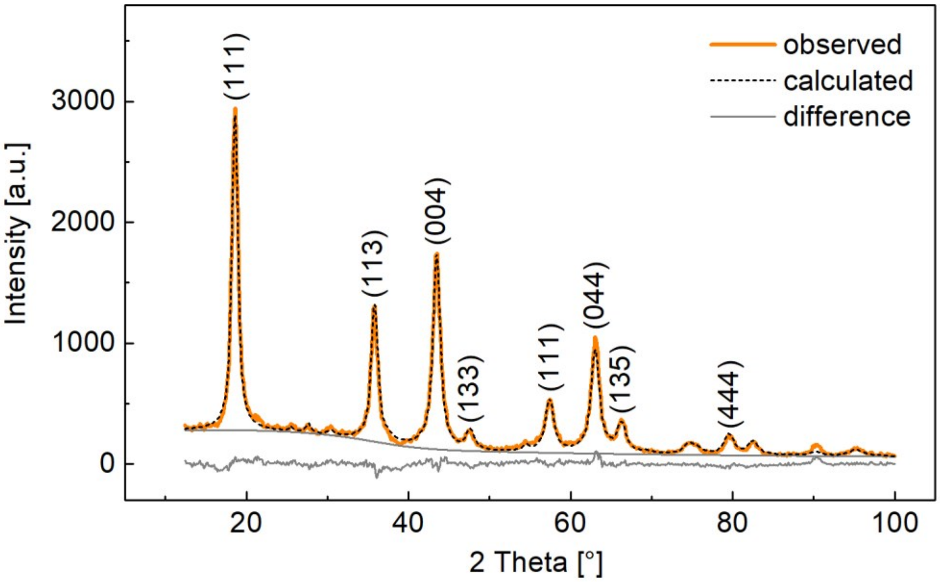

Fig. 7.1 Exemplary diffractogram of FSP-prepared LTO_{LAA} powder with denoted Miller indices (adapted with permission from [98]).

The Rietveld refinement for the *in-situ* mixed LTO/C composite in **Fig. 7.2**, shows the same reflections as the non-functionalized LTO sample (c.f. **Fig. 7.1**). Clear indications of a crystalline carbon phase were absent. The LTO unit cell parameters were comparable to single-flame LTO with 8.35 Å for a, b, c, and 90° for α, β, γ. The LTO density was 3.49 g/cm^3 and the average crystallite size was found to be d_{XRD}= 9 nm. The larger LTO crystallite sizes compared to single flame-prepared LTO, may be due to the additional heat of the second flame spray (xylene) in the reactor upon synthesis, supporting crystallite growth.

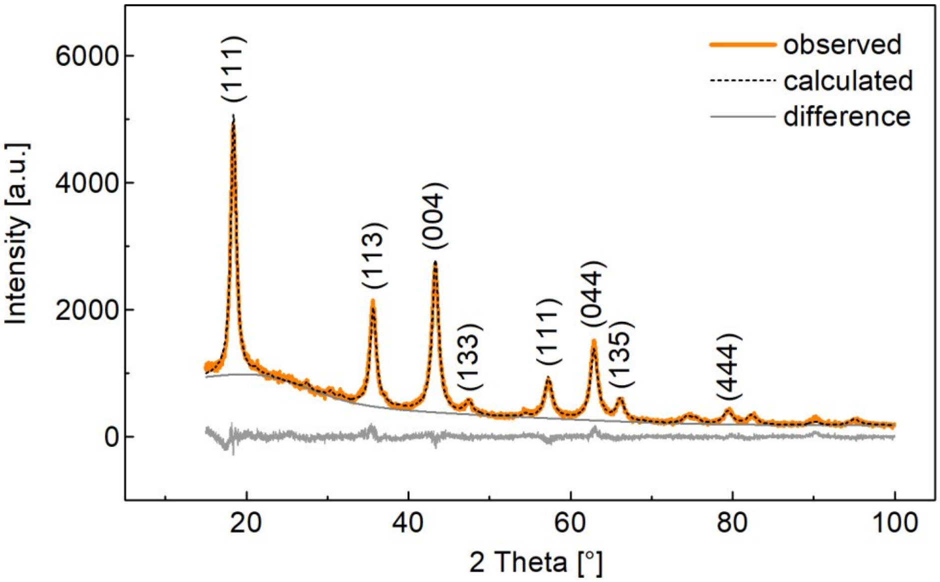

Fig. 7.2 Diffractogram of FSP-prepared LTO/C powder with denoted Miller indices.

Flex-TFBs comprising LTO(3.3) electrodes were prepared from LTO$_{LAA}$. Contrary, LTO(300) and LTO(3.4) electrodes were prepared from LAA$_{EHA}$+TTIP$_{Xylene}$, targeting a LTO phase purity of 100 wt% [96]. Indeed, the Rietveld refinement of LTO powder produced from LAA$_{EHA}$+TTIP$_{Xylene}$ revealed a LTO phase purity of 100 wt% without any indications of concomitant phases (**Fig. 7.3a**). The corresponding LTO unit cell parameters were 8.36 Å for a, b, c, and 90° for α, β, γ. The density and average crystallite size of the LTO powder were 3.47 g/cm^3 and 7 nm, respectively.

Rietveld refinement of the pellet (300 MPa) prepared for porosity investigations, is presented in **Fig. 7.3b**. The investigated pellet had a diameter of 10 mm and thus filled the 20x20 mm^2 XRD sample holder only incompletely. Less involved LTO powder compared to the powder sample (**Fig. 7.3a**), may explain the lower observed count intensities. The LTO phase purity and unit cell parameters of the pellet were unaltered after compression, *i.e.* a, b, c and α, β, γ, of 8.36 Å and 90°, respectively. The determined density and average crystallite size of LTO pellets (300 MPa) were 3.48 g/cm³ and 6.6 nm [126].

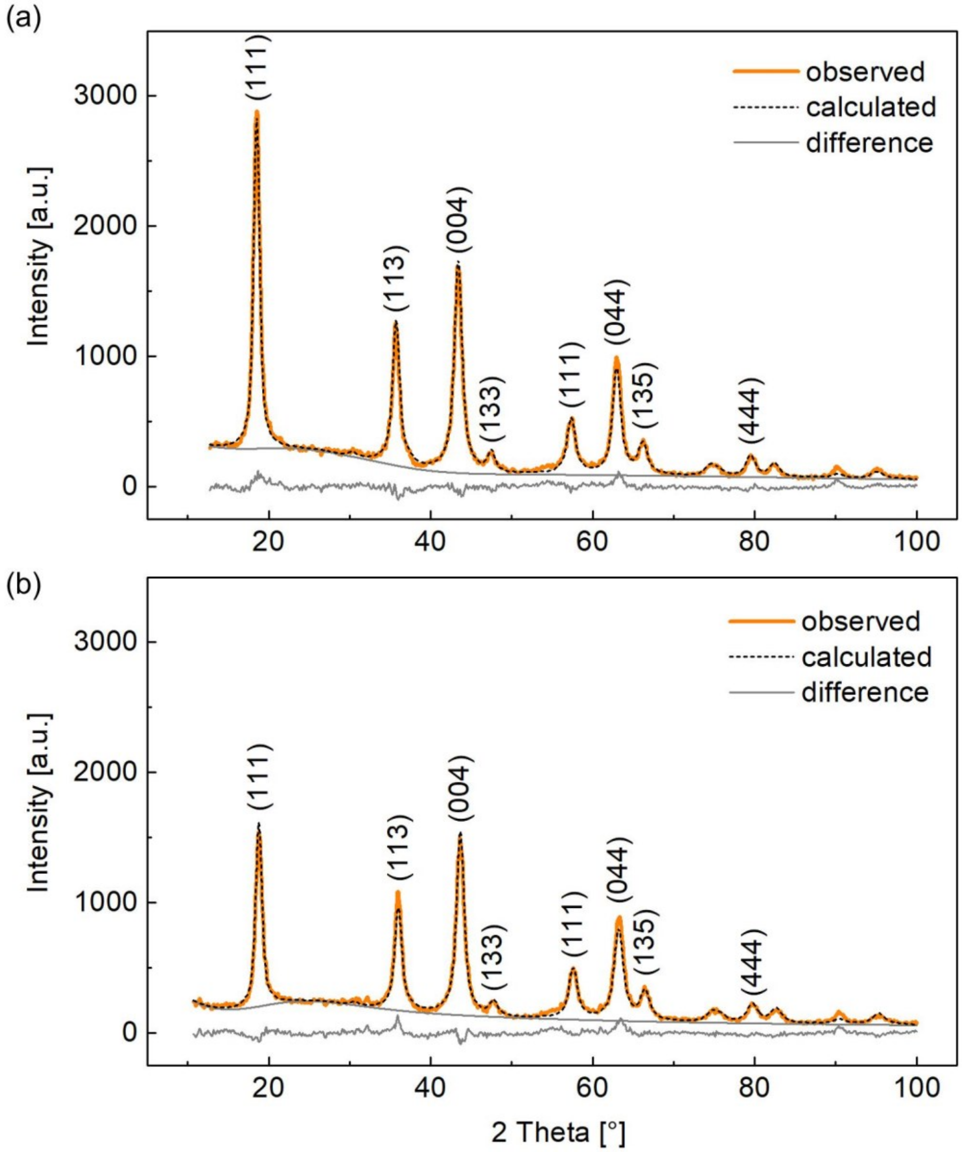

Fig. 7.3 Rietveld refinement plots of **(a)** FSP produced LTO powder and **(b)** compressed LTO(300) pellet, showing pure LTO material. Miller indices are indicated above the prominent LTO reflections adapted with permission from [126].

7.2. Nitrogen Adsorption Experiments

The specific surface area of as-prepared LTO powder was determined to 170 ± 2 m²/g with a BET average particle size of d_{BET}= 10.2 ± 0.2 nm. Together with the average crystallite size d_{XRD}= 6.6 nm, this confirms the presence of ultra-fine FSP-synthesized LTO particles [126].

7.3. Thermogravimetric Analysis

In search of possible adsorbed impurities such as incompletely combusted hydrocarbons or surface water, as-prepared LTO powder was characterized with TGA-DSC-MS. The sample experienced a total weight loss of 7.1 wt% (**Fig. 7.4a**) [98].

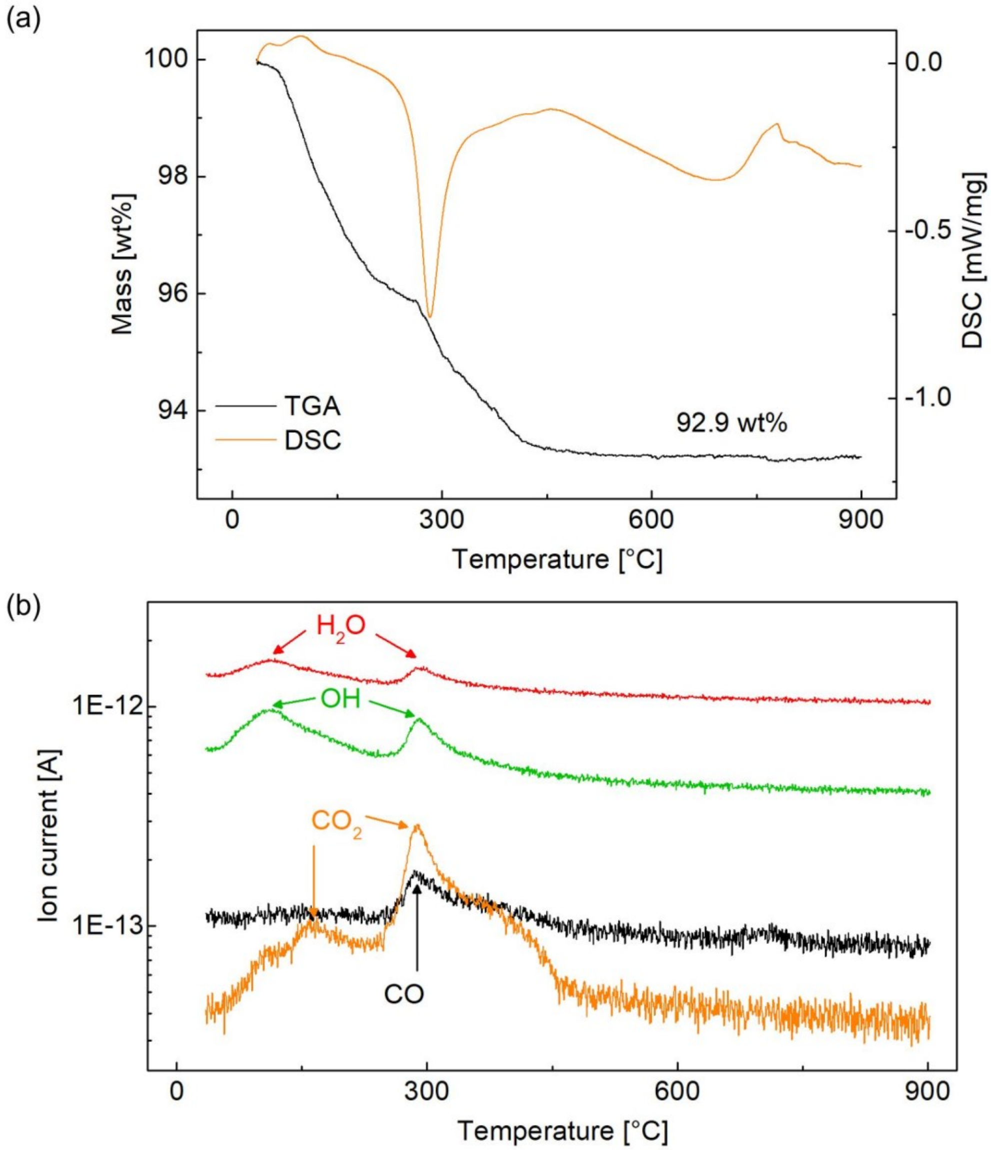

Fig. 7.4 (a) TGA and DSC data obtained from LTO powder heated in synthetic air, and **(b)** MS signals from the evolving gases obtained *in-operando* (adapted with permission from [98]).

The mass reduction occurred between 65-475°C, which was, according to the DSC signal and the MS data (**Fig. 7.4b**), ascribed to the release of the physically adsorbed species H_2O, -OH and CO_2. Such impurities are readily adsorbed due to the high surface area of the FSP synthesized powders and their high sensitivity to surface reactions. Meierhofer *et al.* suggested that the amount of such carbon-based impurities was related to a shortage of oxygen during flame spray synthesis [96,98].

7.4. Transmission Electron Microscopy

The particle morphology of as-prepared LTO powders was investigated with TEM. The low-resolution TEM image in **Fig. 7.5a** depicts the presence of spherical aggregated FSP-produced nanoparticles. The high-resolution TEM image in **Fig. 7.5b**, presents several crystalline nanoparticles. The particle in the center had a lattice spacing of 0.48 nm. This was in agreement with d_{111}= 0.48 nm as derived from XRD (18.6°2θ), thus confirming the depicted particles to be LTO [97].

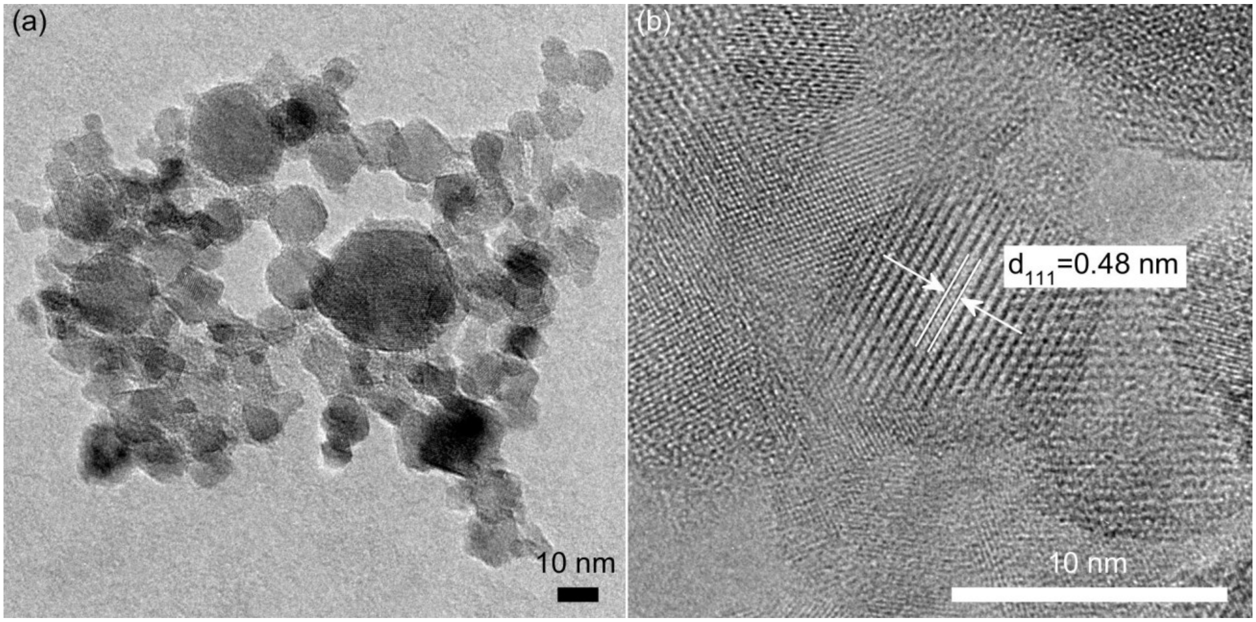

Fig. 7.5 (a) Typical low resolution TEM image of as-prepared LTO particle aggregates, **(b)** high-resolution TEM image of aggregated LTO particles. The lattice spacing of 0.48 nm is indicated, corresponding to the (111) interplanar spacing of LTO.

The DFSP synthesized LTO/C composite comprised highly aggregated particles, as shown in the low-resolution TEM image in **Fig. 7.6a**. The mean particle size of LTO was d_{TEM}= 10.4 ± 2.4 nm (135 counted particles), which is in accordance with d_{XRD}= 6-9 nm and d_{BET}= ~10 nm. The carbon phase was rather present as an interconnected matrix [97]. A re-evaluation of the TEM data presented in reference [97], revealed that the individually found carbon particles displayed a concentrical structure composed of basal graphite planes (**Fig. 7.6b**). The parallel arrangement of these graphite units increased towards the particles perimeter. The graphite units exhibited average lattice spacings of d_{002}=0.39 ± 0.02 nm (**Fig. 7.6c**) with minima and maxima of 0.35-0.42 nm, respectively. Since these carbon structures had d_{002}-spacings larger than 0.34 nm between two adjacent planes, they were defined as turbostratic [97,137]. Similar to the ABAB stacking sequence in hexagonal graphite, turbostratic carbon structures are also stacked, however, the layers may rotate at random around the normal of the stack [138,139]. Despite the existence of graphite units, observable reflections in the XRD data were absent. This was ascribed to the large d_{002}-spacing and the lack in long-range parallel arrangement of the graphite units [140]. Similar carbon morphologies as those reported in the current work, were considered to be typical for soot obtained from hydrocarbon combustion of various sources [141,142]. An appropriate perspective 3D-drawing of such soot particles was presented in Heidenreich *et al.* [143].

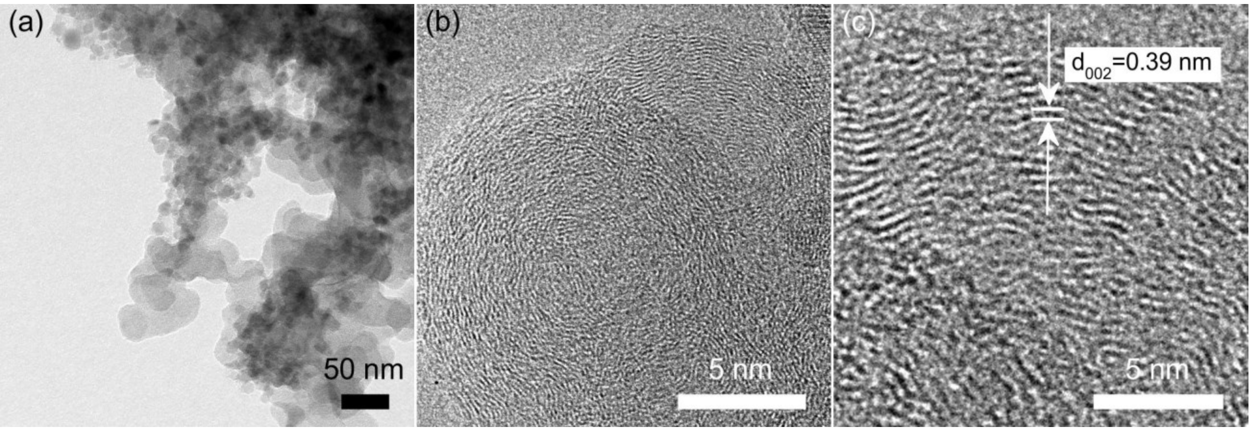

Fig. 7.6 (a) low-resolution TEM image of the aggregated LTO/C composite, **(b)** carbon particles, **(c)** close-up of carbon structure ((b-c) adapted with permission from [97]).

8. Morphological Characterization of $Li_4Ti_5O_{12}$ Layers

8.1. Effect of Compression on $Li_4Ti_5O_{12}$/Carbon Layers

Fig. 8.1a illustrates the surface of a laminated LTO/C electrode with attached glass-fiber residues. Electrochemically, these residues were unobjectionable since they comprised the same material (glass-fibers) as common separators in LIB preparation [97]. However, they were obscuring the real electrode loadings. **Fig. 8.1b-d** illustrate cross-sections of LTO/C(1.5), LTO/C(2.6) and LTO/C(3.3), respectively, characterized by remarkably regular and porous particle networks. Under close consideration of the cross-sections, it was found that increments in pressure caused denser particle networks. The least porous and most regular network was found for the strongest compressed layer, *i.e.* LTO/C(3.3). **Fig. 8.1e** demonstrates the microstructure of LTO/C(DBap), featuring a significantly less regular and less porous microstructure than the laminated electrodes. Highly densified domains, possibly the binder, were found embedded in the LTO/C(DBap)-matrix, as highlighted with the white dashed lines. **Fig. 8.1f** shows the microstructure of LTO/C(DBc), which was highly dense due to the calendering step. In the electrochemical section it will be shown how the different microstructures affect the cycling performance in a LIB half-cell.

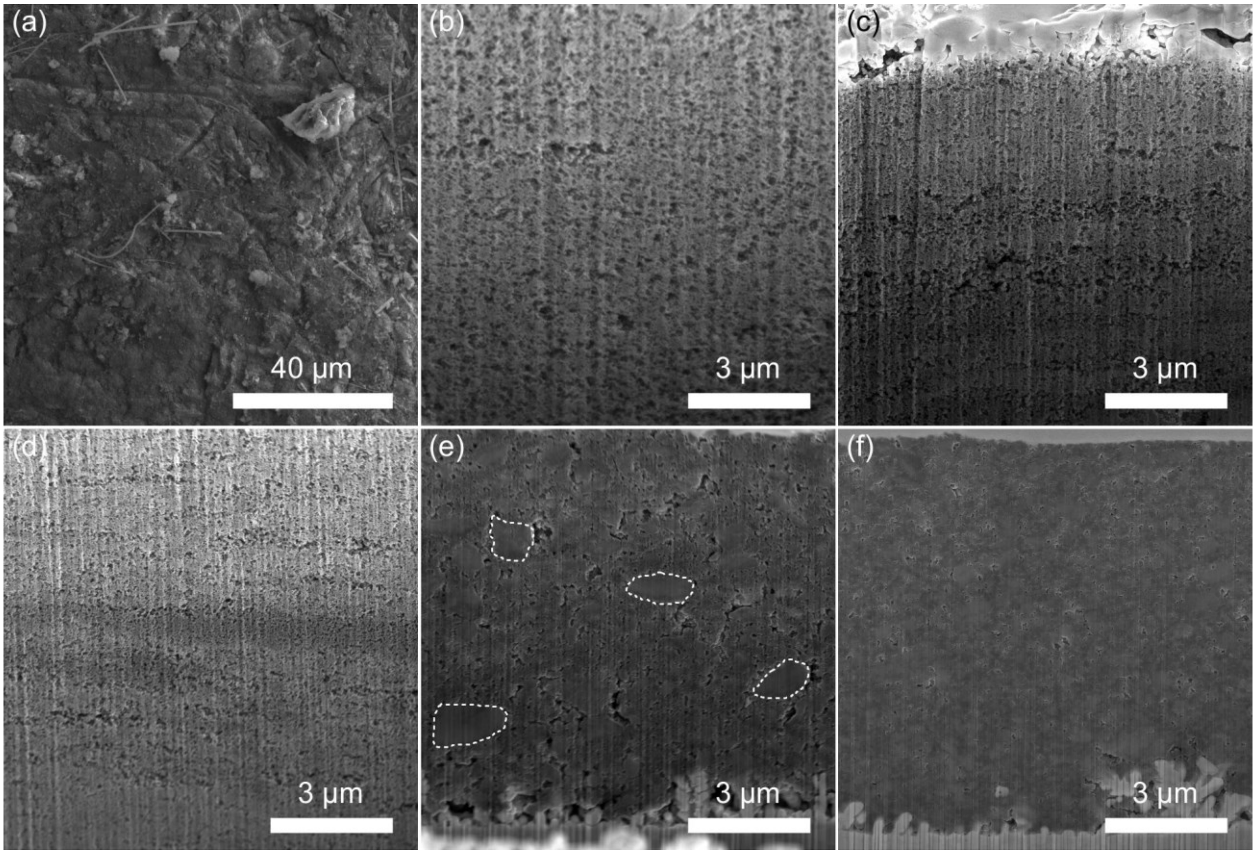

Fig. 8.1 (a) SEM surface image of a typical laminated electrode with attached glass-fiber residues. Cross-sectional cuts recorded from **(b)** LTO/C(1.5), **(c)** LTO/C(2.6) **(d)** LTO/C(3.3), **(e)** LTO/C(DBap), and **(f)** LTO/C(DBc). Laminated electrodes featured a homogeneous porous network, and porosity reduction upon compression. Doctor bladed electrodes appeared dense and irregular, comprising highly dense domains (white dashed lines). LTO/C(DBap) porosity reduced drastically after calendering, *i.e.* LTO/C(DBc) ((b-f) adapted with permission from [97]).

8.2. $Li_4Ti_5O_{12}$ Thin-Film Topography and Microstructure

A representative photography of LTO(3.3) electrodes, is presented in **Fig. 8.2a**, showing a macroscopically homogeneous LTO surface. The KaCu substrate was successfully covered with a thin polycrystalline LTO(3.3) nanoparticle layer. The temperature-sensitive polymer substrates endured the LTO deposition process without any damage. Complementing the XRD results, this result confirmed that FSP method enables the fast *in-situ* deposition of crystalline and phase-pure LTO nanoparticles to temperature-sensitive polymer substrates. This is an interesting finding, since common thin-film synthesis methods such as magnetron sputtering and pulsed laser deposition often face substrate decomposition at the increased temperatures which are needed for crystallization of amorphous active materials. It has to be considered though, that the FSP-produced thin-films comprised highly porous nanoparticle networks, instead of dense homogeneous layers. This could have adverse effects regarding energy density and charge transport, but also advantageous in terms of buffering typical volume changes upon reversible battery-cell cycling, or retaining the mechanical layer stability during cell-bending. As a drawback of the deposition process, the LTO(3.3) films (Ø=10 mm) were occasionally shifted with respect to the equally-sized underlying copper current collector. **Fig. 8.2b** shows a secondary electron image of a LTO(3.3) electrode surface, presenting a highly porous LTO(3.3) particle network. As a side-note, the porosity of the compressed LTO(3.3) thin-films clearly resembled the porous network structure of the transfer-laminated LTO/C electrode cross-sections shown in **Fig. 8.1b-d**.

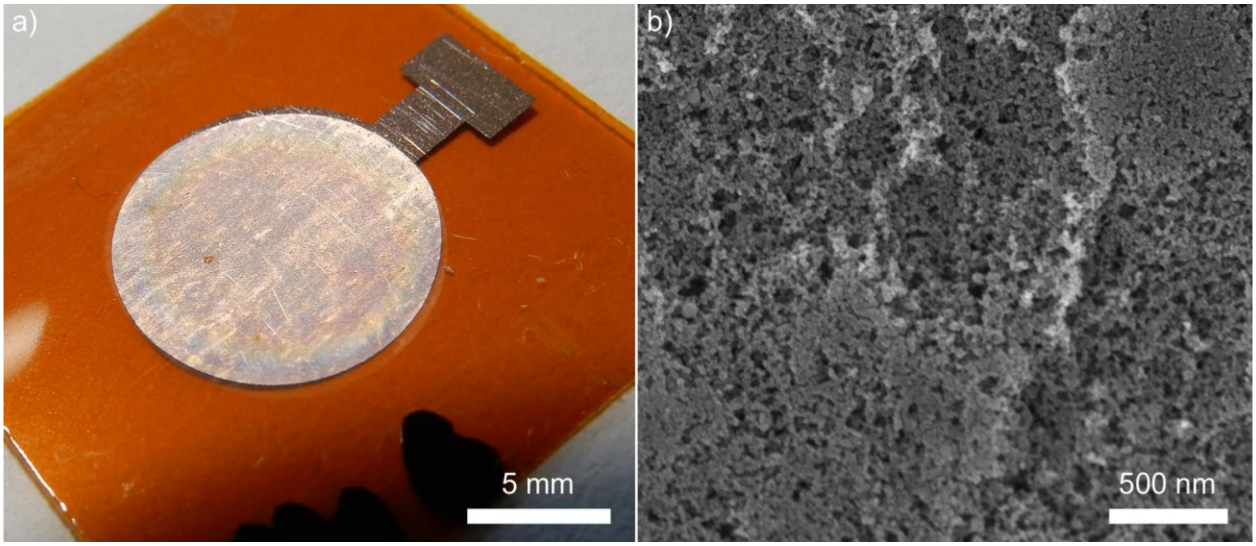

Fig. 8.2 (a) representative photographical and **(b)** SEM images of LTO(3.3) electrode layers on KaCu substrates (adapted with permission from [98]).

A surface topographical investigation of LTO(3.3) electrode thin-films was performed with LSM. **Fig. 8.3a and Fig. 8.3b** show typical 2D-surface and 3D-images of a 50x50 μm^2-section of the LTO(3.3)-electrode, respectively. The position of a representative height profile was marked in both images. The height profile data was normalized to the lowest measured data point (2.294 µm) and is illustrated in **Fig. 8.3c**. Maximum and average height as well as average arithmetic mean roughness (R_a) of the height profile were 0.608, 0.361 and 0.034 µm, respectively. Surface roughness characterization at twenty-one different 2D surface-sections, resulted in R_a of 115 nm. This value was slightly higher than for the height profile due to the larger considered surface area. Nevertheless, the measured arithmetic roughness indicated fairly smooth LTO(3.3) surfaces. Smooth surfaces were of major importance to thoroughly cover the LTO films with LiPON, avoiding pinhole formation and short circuiting with the lithium anode [98].

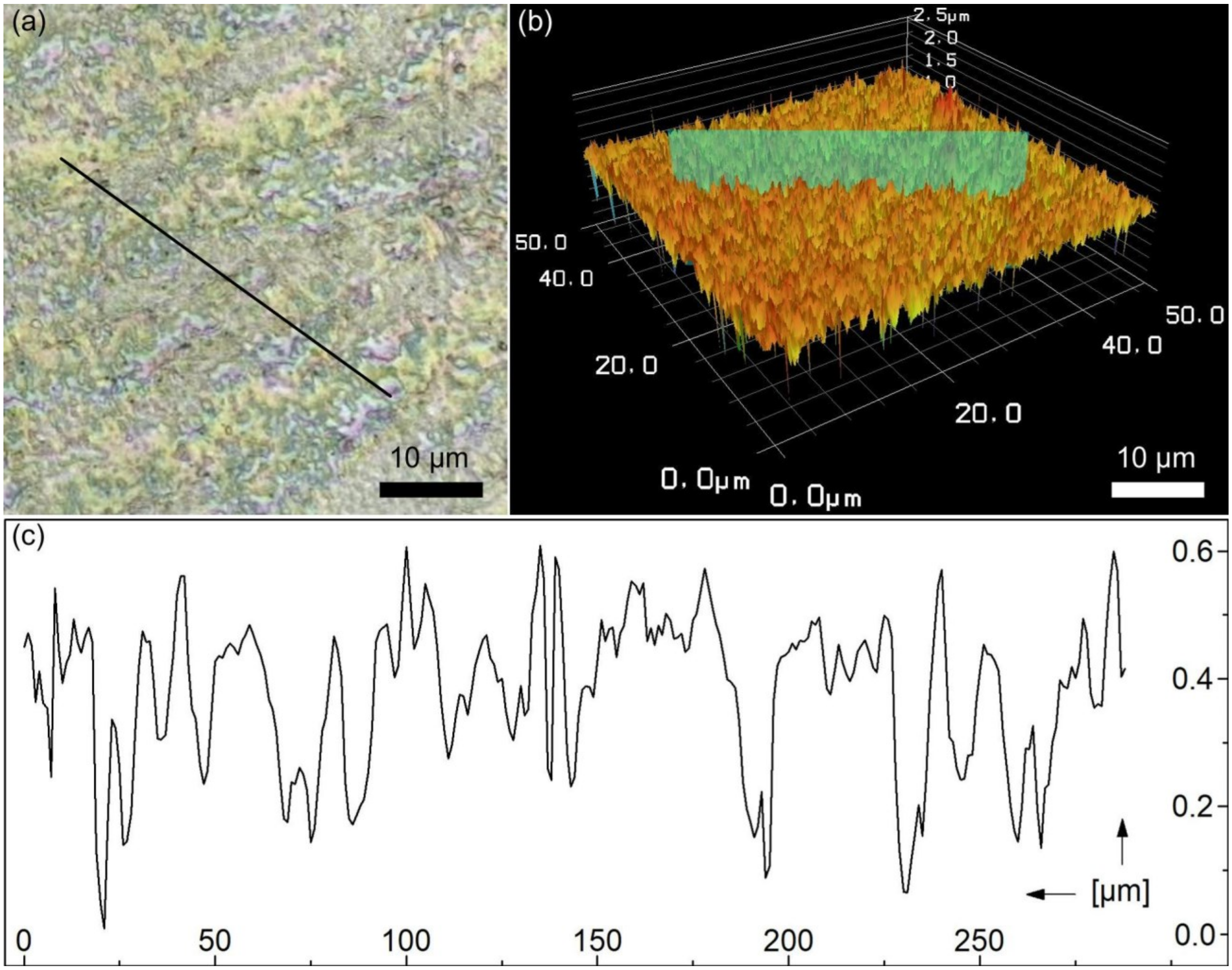

Fig. 8.3 (a) LSM image of a 2D- (color and laser) and **(b)** 3D-image of a random surface-section with indicated height profile and **(c)** corresponding profile data (adapted with permission from [98]).

Using the optimized FSP setup and shadow mask, LTO(ap), LTO(300) and LTO(3.4) were investigated with LSM to characterize the LTO thin-film topographies. Surface illustrations of LTO(ap), LTO(300) and LTO(3.4) electrodes are represented as 2D images in **Fig. 8.4a**-**c**, and 3D images in **Fig. 8.4d**-**f**, respectively. According to the 2D and 3D images, the LTO(ap) electrodes (**Fig. 8.4a,d**) revealed predominantly smooth surfaces with few island-like elevations. Unlike LTO(ap), both LTO(300) (**Fig. 8.4b,e**) and LTO(3.4) (**Fig. 8.4c,f**) revealed more irregular surfaces. The topographical surface analysis delivered R_a of 46, 131 and 95 nm for LTO(ap), LTO(300) and LTO(3.4), respectively. Most likely, the PTFE foil for LTO(300) or PTFE tape for LTO(3.4) shifted or detached certain LTO film areas after its removal, explaining the larger roughnesses. Nevertheless, both compression techniques resulted in low-roughness topographies. The surfaces of all three electrode types showed even lower R_a values, *i.e.* smoother surfaces, than the LTO(3.3) electrodes fabricated from the prototypical FSP setup [126].

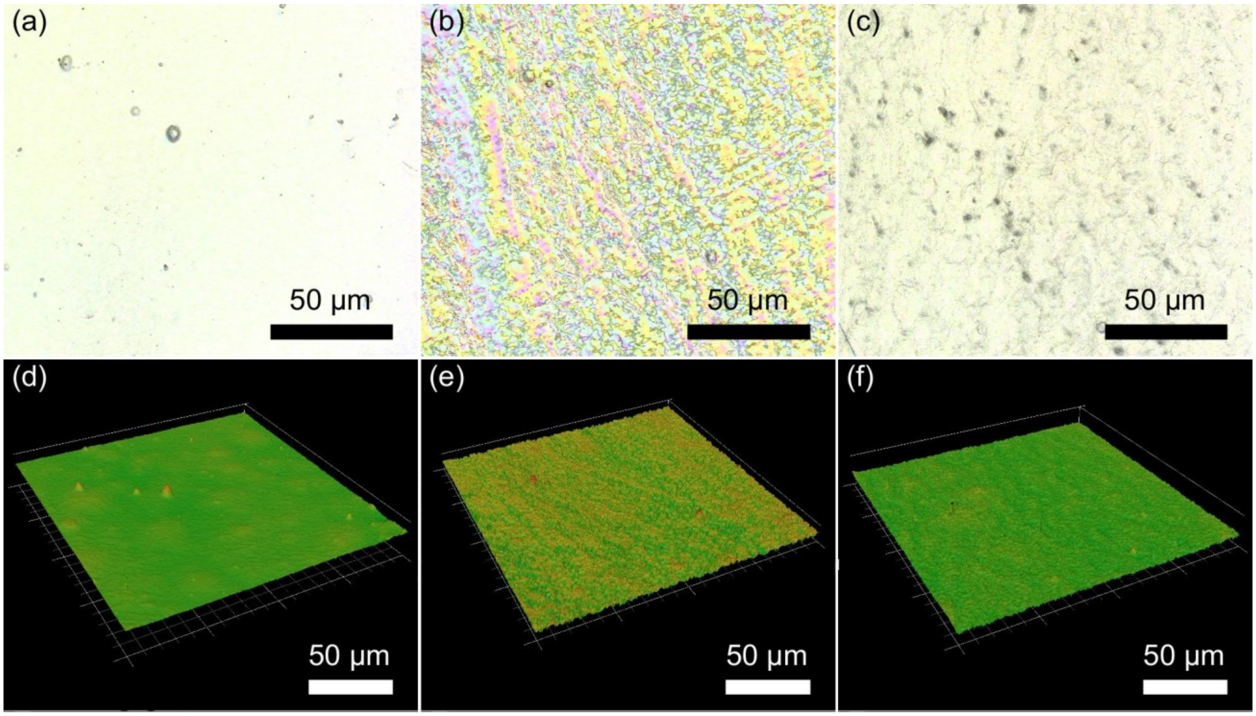

Fig. 8.4 2D and 3D representations of surface-sections from LTO(ap), LTO(300) and LTO(3.4). **(a, d)** LTO(ap) featured predominantly smooth surfaces with only few elevations. After compression, **(b, e)** LTO(300) and **(c, f)** LTO(3.4), showed surface structuring but still provided sufficiently smooth surfaces that were thoroughly coatable with LiPON (adapted with permission from [126]).

8.3. $Li_4Ti_5O_{12}$ Thin-Films within Flexible Thin-Film Batteries

Electron microscopy was used to obtain a visual impression of the LTO(3.3) electrodes assembled in flex-TFBs. SEM-FIB-cuts of fabricated LTO(3.3)/LiPON/Li battery-cells are presented in **Fig. 8.5a**, showing the upward layering of Kapton® (75 µm), Cu (0.18 µm), LTO (0.55 µm), LiPON (1.66 µm), Li (~2 µm) and Pt patch. **Fig. 8.5b** presents a close-up of the battery-cells cross-section, revealing a fairly uniform and porous LTO(3.3) structure. Pin-hole formation and consequent shorting of the battery-cell was successfully avoided due to the low-roughness surface (115 nm) of the LTO(3.3) layer (cf. **Fig. 8.3a-c**). To investigate the LTO(3.3)/LiPON interface, qualitative elemental distribution analysis of the battery-cells cross-section was carried out using EDX. Due to a low resolution for the EDX mapping with a minimum of 1 µm², an accurate statement on the elemental distribution between the LiPON and the thin (0.55 µm) and porous LTO(3.3) film was difficult. Nevertheless, **Fig. 8.5c** depicts a homogeneous distribution of titanium and oxygen in the LTO(3.3) layer and phosphorous, oxygen and nitrogen in the LiPON layer. **Fig. 8.5d** shows an elemental profile investigation of the battery-cell cross-section and the determined elemental (Ti, O, N, P) count intensity [98].

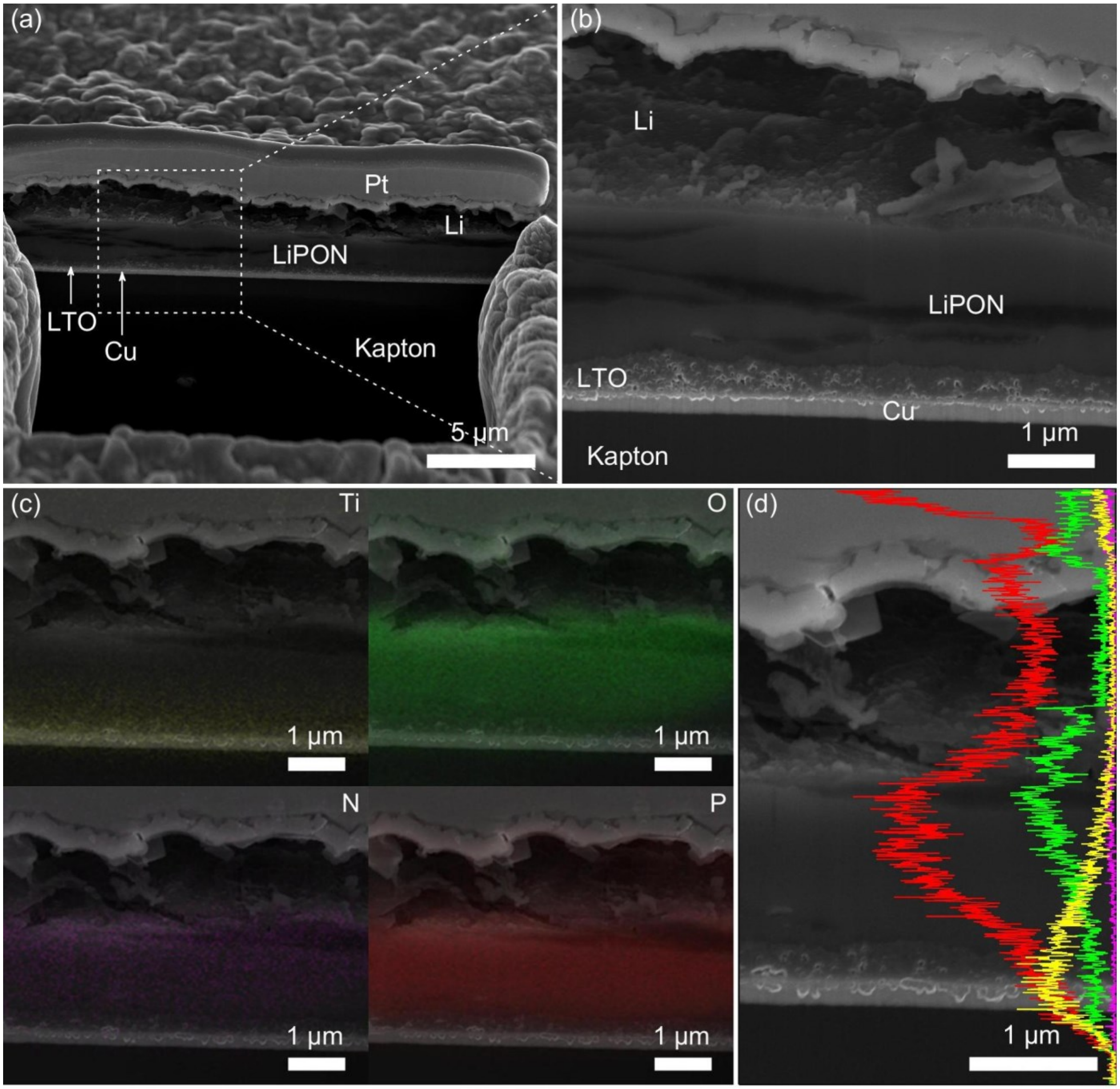

Fig. 8.5 Illustrative cross-section of a LTO(3.3)/LiPON/Li battery-cell, **(a)** SEM-FIB-produced cross-sectional image, **(b)** a magnified section is revealing a fairly uniform and porous LTO(3.3) layer, **(c)** elemental mapping investigation and **(d)** elemental profile characterization of the LTO(3.3) cross-section. Profile colors in (d) correspond to those in (c) (adapted with permission from [98]).

The FIB-SEM imaging of the LTO(300) and LTO(3.4) electrodes, revealed significant differences in porosities and film heights (**Fig. 8.6**). LTO(300) was uniformly embedded in between the copper and LiPON layers (**Fig. 8.6a**). In a magnified view (**Fig. 8.6b**), the LTO(300) layer exhibited a dense and homogeneous microstructure with a thickness of 415 nm. The LTO(3.4) film in **Fig. 8.6c** was, likewise, safely embedded in between the adjacent functional layers. However, it showed varying film thicknesses ranging from 700 to 1300 nm. The larger film heights of LTO(3.4), compared to LTO(3.3) with 550 nm, were ascribed to the two times larger sprayed LTO solution volume. The magnified area of LTO(3.4) in **Fig. 8.6d**, revealed clearly higher layer porosities, similar to LTO(3.3), than observed for LTO(300). LTO(3.4), furthermore, featured a crack in close vicinity to the LTO/copper interface. This was attributed to the lower degree of compression and poorer connections within the particle network. Such physical disturbances in a layer will kinetically inhibit the intrinsic electrical and ionic transport properties, further contributing to hindrances in dis-/charge reaction kinetics [126].

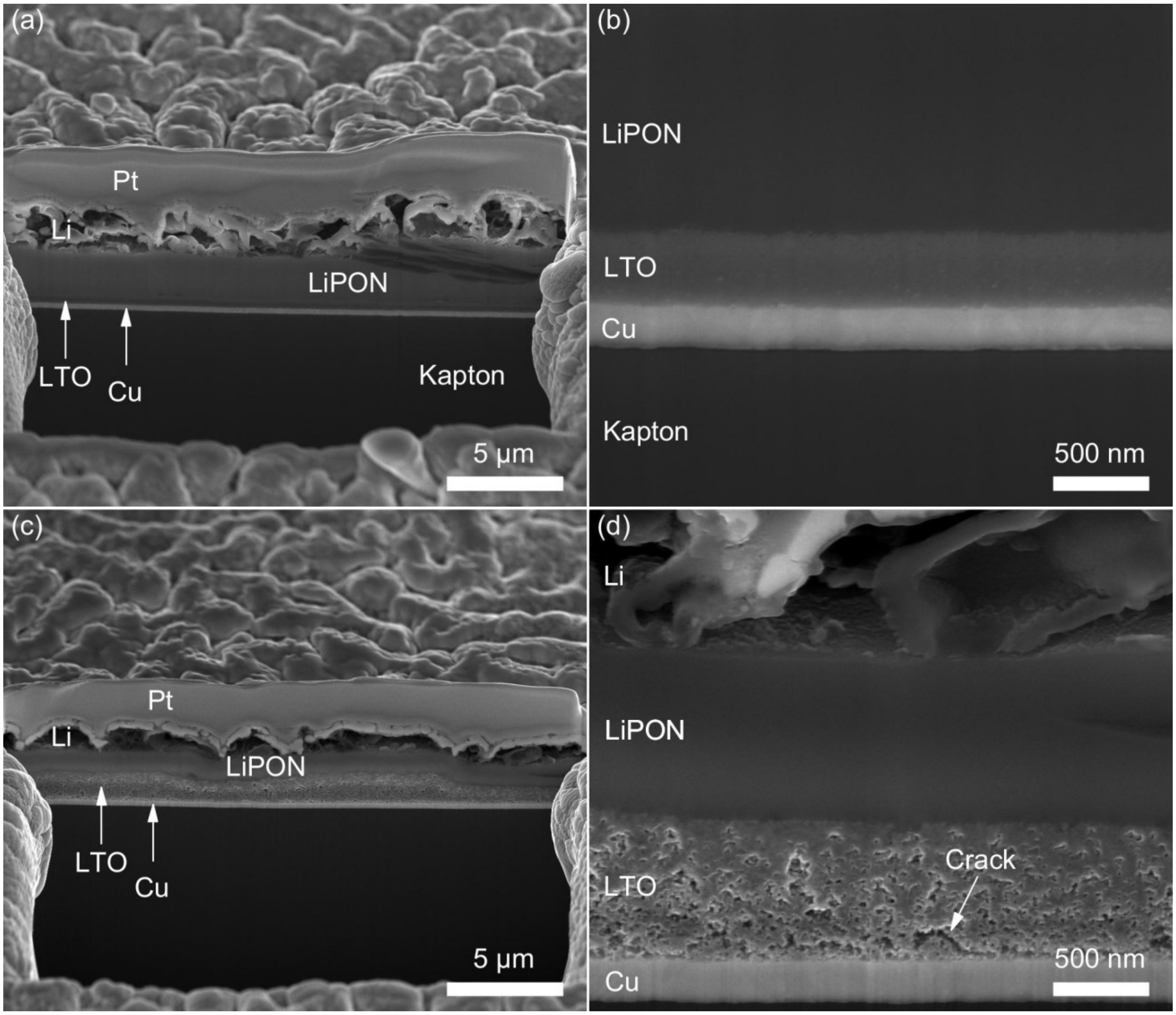

Fig. 8.6 Flex-TFB overview and LTO close-up images of SEM-FIB cuts for LTO(300) and LTO(3.4) are shown in **(a)**, **(b)** and **(c)**, **(d)**, respectively. The higher compressed LTO(300) layer appeared to be dense, homogeneous and thin, whereas the less compressed LTO(3.4) layer was highly porous, more irregular and thicker. The LTO(3.4) microstructure featured cracks close to the copper substrate (adapted with permission from [126]).

8.4. Porosity Determination of $Li_4Ti_5O_{12}$ Thin-Films

Understanding the properties of the *in-situ* deposited LTO thin-films such as porosities and pore-size distributions was crucial to relate microstructural effects to electrochemical performances. As reported previously, Mädler *et al.* determined the porosity of thermophoretically collected nanoparticle-aggregates, comprising twenty primary particles of 10 nm to around 98.9% [117]. A comparable porosity was expected for the as-prepared, uncompressed LTO thin-film electrodes. It was unknown to which extent the porosity of the LTO electrodes has reduced upon compression for LTO(3.3), LTO(300) and LTO(3.4).

To provide a first estimation of the actual LTO(3.3) layer porosity, the mass of the circular LTO thin-film was calculated using LTO density (3.48 g/cm³), film radius (5 mm) and film height from SEM-FIB cuts (0.55 μm), assuming a completely dense layer. From the determined mass (150 μg) and the mass difference to the actual weighted mass (13-29 μg), a roughly estimated porosity of ~80-91% was determined, suggesting highly porous LTO(3.3) microstructures [98]. At such high LTO(3.3) layer porosities, it may be evident that the overall lithium-ion reaction site accessibility in an all-solid-state LIB system without an ionically conductive electrolyte was limited. Consequently, the overpotentials upon dis-/charging may have become more dominant for electrodes with higher loadings.

Autosorb measurements were conducted to approximate the porosities and pore size distributions of LTO(300) and LTO(3.4) electrodes. LTO(300) pellets and glass-fiber filter sandwiches compressed at 3.4 MPa, revealed experimental porosities of 46.6% and 76.7%. As shown in **Fig. 8.7**, the simulated porosities of LTO(300) and LTO(3.4), were in reasonable agreement with 46.4% and 75.9%, respectively. The experimentally derived median pore diameters (horizontal lines in the boxes) of LTO(300) and LTO(3.4) were 3.5 and 18.4 nm, respectively. This was lower than the simulated observations, *i.e.* 8.4 and 27.0 nm, respectively. The experimental information of the inner 50% of all pore sizes (d50, box heights) were comparable to the simulations. The whiskers in **Fig. 8.7** depict the size distribution of the inner 95% (d95) of the pore size population. Comparing the determined porosities and pore size distributions of LTO(300) with those of LTO(3.4), clearly indicated that a compression with almost two magnitude higher pressures, led to significantly thinner and denser layers, accompanied by smaller pore diameters [126].

Interestingly, the simulation of LTO(3.4) and LTO(300) microstructures, revealed increased LTO particle coordination numbers from 3.5 to 5.5, respectively. Also LTO particle contact densities at the compacting wall grew from 850 (LTO(3.4)) to 5094 1/μm² (LTO(300)). Both observations indicated that the LTO(300) particle network exhibited a significantly larger contact area among the LTO particles, but also at the interfaces with the adjacent layers (LiPON and current collector). This potentially promoted charge transfer and efficient use of the LTO active material for higher compressed LTO(300) [126].

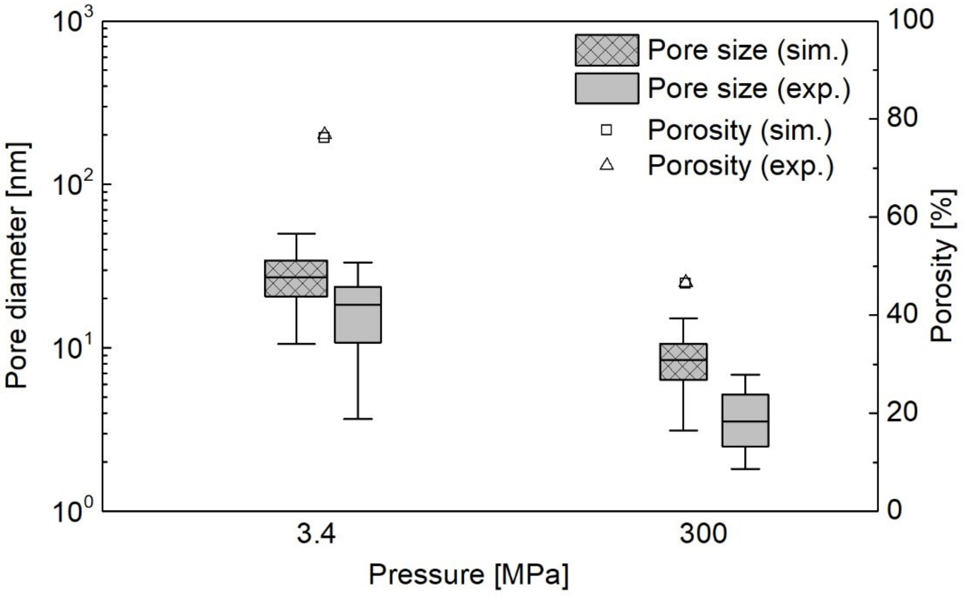

Fig. 8.7 Simulated and experimental porosities and pore size distributions derived from LTO(3.4) and LTO(300) (adapted with permission from [126]).

The four point Van der Pauw method was applied to LTO(300) and LTO(3.4) layers, to understand whether denser microstructures favorably affected the electrical sheet resistivities. Indeed, it was found that the LTO(300) revealed significantly lower sheet resistivities than LTO(3.4) with 6 and 150 k**Ω**, respectively. Based on the previous results, the improved electrical transport was attributed to the larger LTO particle coordination numbers and contact densities in the thinner and denser LTO(300) electrode [126]. The same phenomena may have led to the improved electrochemical performances of previously mentioned transfer-laminated LTO/C(3.3)-based LIBs [97].

9. Electrochemical Performance Characterization

9.1. Effect of Precursor-Solvent Combination on Electrochemical Performance

In the LTO_{LNT}, LTO_{LTB} and LTO_{LAA}-based pouch-cells, LTO was applied as cathode and lithium foil as anode. Since the LTO cathodes were assembled in delithiated state, *i.e.* $Li_4Ti_5O_{12}$, the battery-cells were charged first. Upon charging, electrons flew from the lithium anodes, through the external wiring, into the LTO composite, while the conductive carbon additive in the cathodes promoted facile electron transport to the LTO reaction sites. The electrons were attracted by the most electropositive species in the $Li_4Ti_5O_{12}$ compound, *i.e.* Ti^{4+}, and reduced three cations out of five to Ti^{3+} [74]. To maintain charge neutrality in both electrodes, the LTO structures intercalated adjacent lithium cations from the surrounding electrolyte, while the lithium anodes were delithiated.

The dis-/charge profiles, *i.e.* voltage *vs.* specific discharge capacity (SDC, capacity normalized to LTO loading) of LTO_{LNT}, LTO_{LTB} and LTO_{LAA}, are presented in **Fig. 9.1** [96]**.** It shows the performance of the battery-cells in the 1st, 2nd and 450th cycle, recorded within a potential range of 1.0 to 2.0 V. In the first discharge cycle, the potentials for all battery-cells decreased smoothly from 2.0 to 1.6 V, entered a flat plateau region at 1.55 V, and continued dropping from 1.5 to 1.0 V.

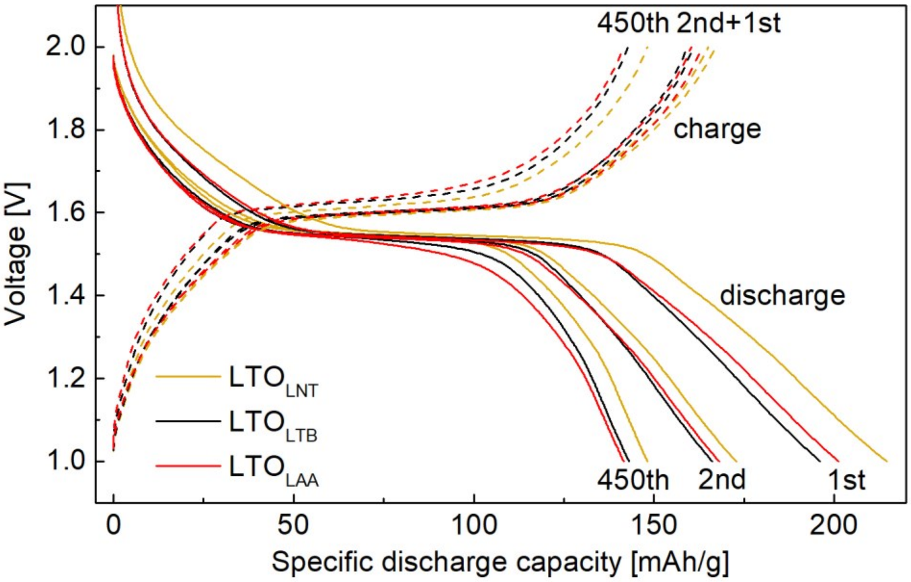

Fig. 9.1 Dis-/charge curves of pouch-cells comprising LTO_{LNT}, LTO_{LTB} and LTO_{LAA} in the 1st, 2nd and 450th cycles (adapted with permission from [96]).

The initial voltage drop upon lithiation was due to formation of a solid solution phase that prevailed the identical phase structure of $Li_4Ti_5O_{12}$ [27,30]. The solid solution reaction is given as:

$$Li_4Ti_5O_{12} + \alpha Li^+ + \alpha e^- \leftrightarrow Li_{4+\alpha}Ti_5O_{12} \tag{9.1}$$

where a represents the fraction of incorporated lithium-ions and electrons. The smooth drop continued with ongoing lithium-ion insertion until the single-phase saturation was reached for all particles. Subsequently, the rock-salt $Li_7Ti_5O_{12}$ phase started forming according to the reaction:

$$Li_4Ti_5O_{12} + (3-\beta)Li^+ + (3-\beta)e^- \leftrightarrow Li_{7-\beta}Ti_5O_{12} \tag{9.2}$$

where *β* stands for missing number of lithium-ions and electrons, to complete the phase transition from spinel to rock-salt LTO. The constant potential plateau corresponded to a two-phase coexistence and equilibrium-like transition of LTO particle surfaces from lithium-deficient to lithium-rich phases [35,144]. In this transition, the phase boundary was described to progressively move inside the crystal upon continuing lithiation [145].

Once the particles approached complete phase transition (approaching end of plateau), a single-phase reaction of the lithium-rich phase occurred until the lithium-rich particles were completely transformed to rock-salt LTO. Analogous to the initial voltage drop of the lithium-poor phase, this single-phase reaction explained the final voltage decrease upon discharging. Ultrafine particles and the corresponding large specific surface area are known to cause a significant expansion of the solid-solution region [32]. This explains why the single-phase reaction regions observed in the present study were much shorter than commonly observed for micron-sized LTO particles. The 1st charge profiles have emerged due to the same principles, however, on reverse. It was found that the observed specific charge capacity was lower than in the first discharge cycle due to losses in the plateau region. This indicated the occurrence of irreversible formation reactions such as SEI-formation, between the lithiated LTO particles and constituents of the electrolyte, *i.e.* ethylene carbonate/diethylene carbonate and $LiPF_6$ [30].

The 2nd discharge cycles showed shortened plateau regions for all three battery-cell types with respect to the first discharge cycles. The 2nd charge cycle was almost identical to the 1st charge cycle, implying that initial irreversible reactions may have decreased. After completing 450 cycles, the dis-/charge profiles of all samples showed further reduction in plateau length and specific capacities, suggesting further loss of the active electrode species. Since capacity losses scale with particle specific surface area, Borghols *et al.* suggested two possible origins for capacity decrements at higher cycle numbers: (1) irreversibly bonded lithium-ion capacity at the surface of the ultra-fine particles and (2) mechanical failure of a thin surface area of the particles, which both may passivate the near-surface area of the particles, explaining the irreversible capacity in the plateau region [30].

The coulombic efficiencies and SDCs evolving over cycle number recorded at rates of 1C, are presented in **Fig. 9.2** for the different LTO battery-cells. The coulombic efficiencies for all samples (filled symbols) have exceeded 99.5% in the twentieth cycle. Since the coulombic efficiency is the quotient of discharged and charged capacity, a value approaching 100% indicated highly reversible lithium intercalation reactions, and thus ceasing of SEI-formation on the expense of active material and liquid electrolyte [30,95]. The SDCs of LTO_{LNT}, LTO_{LTB} and LTO_{LAA} (hollow symbols) were 210.9, 193.5 and 202.3 mAh/g in the first, and 156.5, 152.1 and 157.3 mAh/g, in the twentieth cycle, respectively. In the 450th cycle, the SDCs of LTO_{LNT}, LTO_{LTB} and LTO_{LAA} were 146.5, 141.8 and 144.8 mAh/g, respectively.

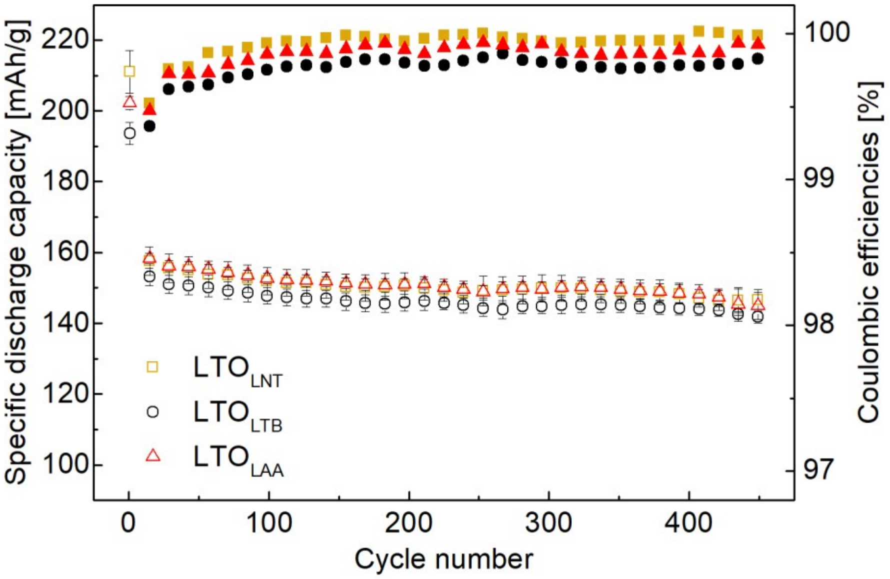

Fig. 9.2 Long-term cycling performance of LTO_{LNT}, LTO_{LTB} and LTO_{LAA} pouch cells (adapted with permission from [96]).

With respect to the 20th cycle, at which the parasitic reaction rate was expected to have ceased, this conformed a capacity fading of 6.4, 6,8 and 8,0% for LTO_{LNT}, LTO_{LTB} and LTO_{LAA}, respectively. The obtained capacities after 450th cycles were around 30 mAh/g lower than the maximum theoretical capacity of LTO (175 mAh/g), however, cycling stability has been proven for all samples. LTO_{LNT} showed the highest specific discharge capacities which was ascribed to slightly lower loadings and film thicknesses (**Table 1**), and thus less pronounced overpotentials, *i.e.* ohmic drop, charge transfer and contact resistances [146]. Also the slightly larger calendering pressure of LTO_{LNT} may have improved the electrochemical performance due to an enhanced electrically conductive network.

Dis-/charge curves for newly prepared pouch cells of LTO_{LNT}, LTO_{LTB} and LTO_{LAA} were derived from rate tests at C/5, C/2, 1C, 2C, 5C, 10C and 25C (**Fig. 9.3a**). With increasing C-rate, the dis-/charge curves of the three samples principally showed similar properties as they did before with increasing cycle number: (1) the reduction of the plateau length was more pronounced, (2) the curved character and the deviation of the profiles from equilibrium potential increased due to growing overpotentials.

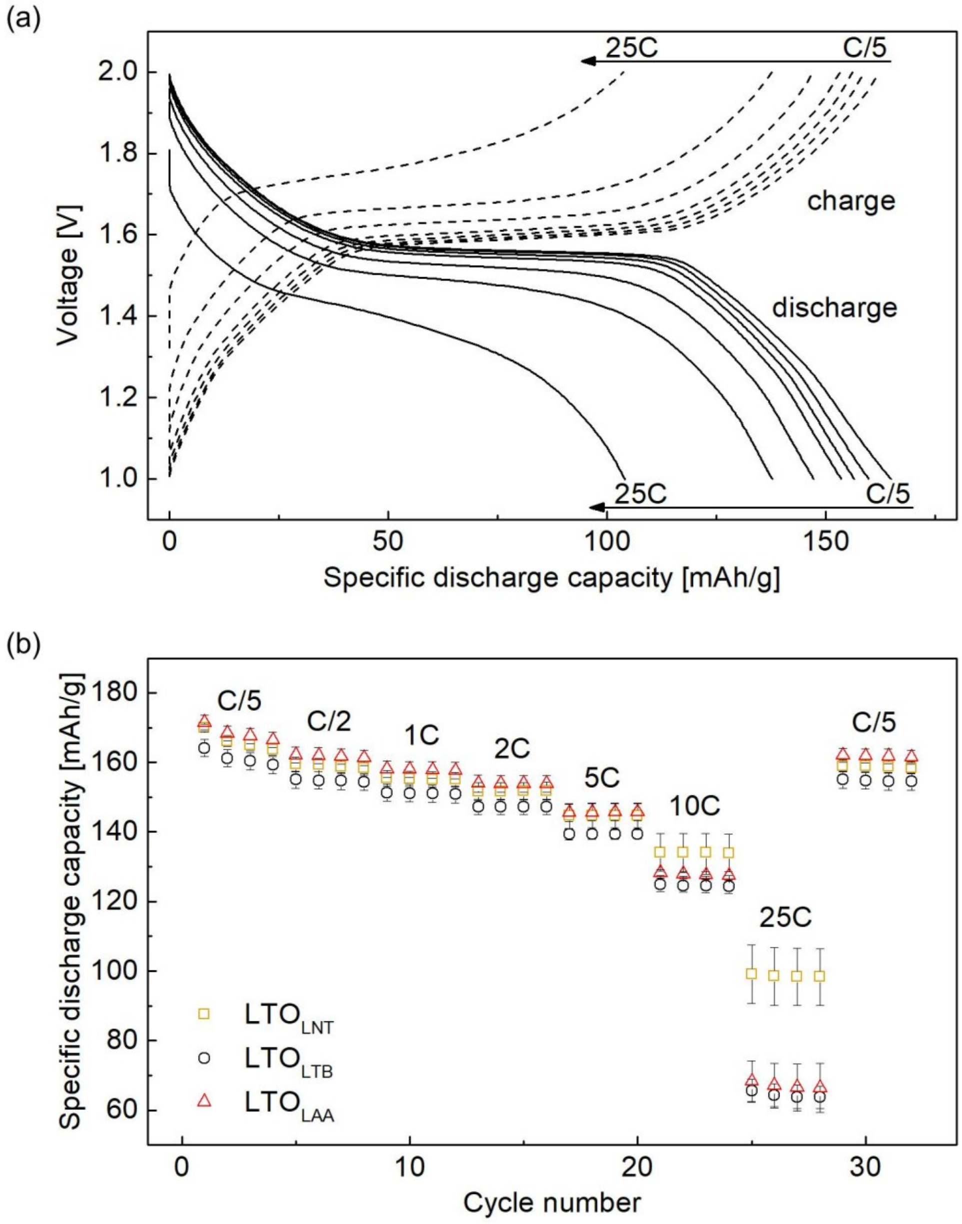

Fig. 9.3 (a) rate-dependent dis-/charge curves, exemplarily shown for $\mathrm{LTO}_{\mathrm{LNT}}$, and **(b)** rate capabilities of $\mathrm{LTO}_{\mathrm{LNT}}$, $\mathrm{LTO}_{\mathrm{LTB}}$ and $\mathrm{LTO}_{\mathrm{LAA}}$ pouch cells recorded at C/5, C/2, 1C, 2C, 5C, 10C and 25C (adapted with permission from [96]).

The SDCs at the lowest rate of C/5 in **Fig. 9.3b**, showed 163.8, 159.3 and 166.4 mAh/g for $\mathrm{LTO}_{\mathrm{LNT}}$, $\mathrm{LTO}_{\mathrm{LTB}}$ and $\mathrm{LTO}_{\mathrm{LAA}}$, respectively. These SDCs at C/5 and C/2 were exceeding those observed in cycling tests conducted at 1C (**Fig. 9.2**) due to lower overpotentials. Since these values were close to the maximum theoretical capacity of LTO (175 mAh/g), this indicated a good material quality of FSP-synthesized LTO. The SDCs at rates of C/2, 1C, 2C, 5C, 10C and 25C were, exemplarily for $\mathrm{LTO}_{\mathrm{LNT}}$, 158, 155, 152, 145, 134 and 98 mAh/g. $\mathrm{LTO}_{\mathrm{LNT}}$ revealed superior rata capability at 25C compared to LTO_{LTB} and LTO_{LAA} with 64 and 67 mAh/g, respectively. A final cycle at C/5 for LTO_{LNT}, showed a SDC of 158.5 mAh/g, proving absence of detrimental effects after high rate application.

In summary, the three distinct precursor solvent combinations of provided LTO_{LNT}, LTO_{LTB} and LTO_{LAA} resulted in LTO powders with comparable electrochemical performances. At 25C, the rate capability of LTO_{LNT} was improved compared to LTO_{LTB} and LTO_{LAA}. The slightly better performance of LTO_{LNT} was attributed to lower film loadings, thicknesses, enhanced electrical conductivity, and thus lower overpotentials [96].

9.2. Effect of $Li_4Ti_5O_{12}$/Carbon Microstructure on Electrochemical Performance

The electrochemical performance of transfer-laminated electrodes LTO/C(1.5), LTO/C(2.6) and LTO/C(3.3), dis-/charged at 1C for 200 cycles, is illustrated in **Fig. 9.4**. Since the glass-fiber residues made an accurate determination of the actual loadings difficult, all determined capacities were presented as relative capacity retention (RCR). The capacity of the 2nd cycles represented the basis for normalization, to avoid the largest contribution of irreversible formation reactions.

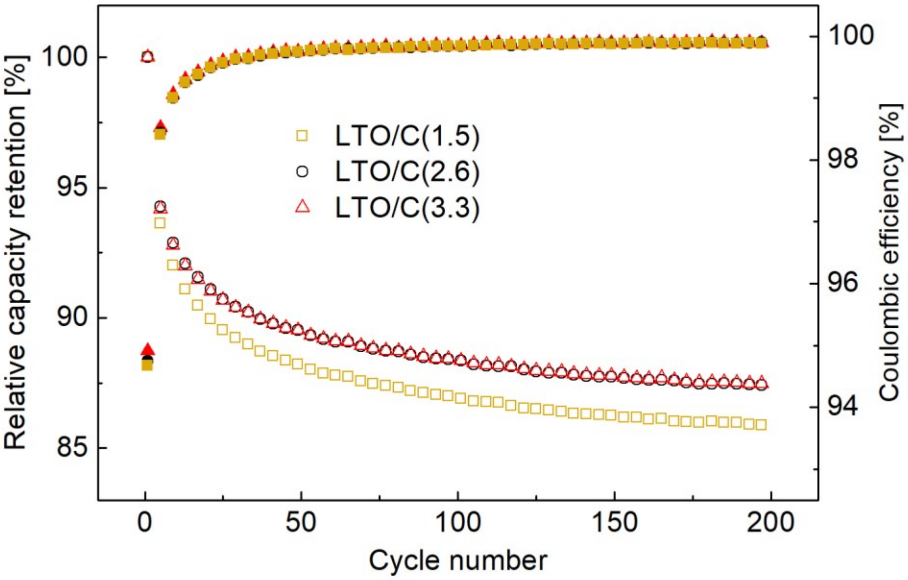

Fig. 9.4 Long-term cycling data obtained from the laminated electrodes dis-/charged at 1C. The RCRs are represented by hollow, and corresponding coulombic efficiencies by filled symbols (adapted with permission from [97]).

Similar to doctor bladed LTO_{LNT}, LTO_{LTB} and LTO_{LAA}, pouch cells with transfer-laminated electrodes experienced capacity losses in the first cycles due to irreversible formation reactions. After 20 cycles, the capacity drop was alleviating and the coulombic efficiencies were approaching >99.5%, indicating declining irreversible reactions and improving reversibilities. Upon completing 200 cycles, LTO/C(2.6) and LTO/C(3.3) exhibited slightly higher capacity retentions (both 87.4%) than LTO/C(1.5) (85.1%). The continuous slight decrease in RCR on progressive cycling was ascribed to (1) gradually increasing overpotentials due to nanoparticle degradation and lattice quality [30,95], and (2) contact losses within the LTO/C layer and at its layer interfaces (mechanical electrode degradation) in absence of a binder [92]. Although the applied carbon in LTO/C was determined to be adequately graphitized [97], the excessive carbon content of ~25 wt% may have increased overpotentials due to additional lithium-ion diffusion barriers [147–149].

The observed performance differences among the three laminated electrodes (**Fig. 9.4**), were imputed solely to the different compaction pressures since the same LTO/C material was applied. As derived from **Fig. 8.1b-d**, stronger transfer-lamination pressures caused denser microstructures. As it was shown for the flex-TFB electrodes of LTO(300) in **section 8.2**, the stronger densification of FSP-prepared LTO networks, resulted in larger particle coordination numbers and contact densities to the interfaces. The same phenomena were expected for the stronger compressed LTO/C layers. In consequence, the electrically and ionically conductive network has been extended for stronger compressed electrodes, resulting in lower overpotentials and improved RCRs [97]. Changes in the ionic conductivity of the particle network, however, may have been less important due to the presence of the liquid electrolyte.

The inset of **Fig. 9.5** exemplarily shows a differential curve diagram, *i.e.* dQ/dU *vs.* U, for LTO/C(1.5) in the 200th dis-/charge cycle at 1C. The peak maxima for oxidation and reduction were indicated with the dashed lines. The distance between the potentials of half-reactions for oxidation and reduction was designated as ΔU. In an ideal battery-cell without any overpotentials, ΔU must be zero, in a practical battery-cell, however, occurrences of overpotentials are inevitable. According to **Fig. 9.5**, overpotentials were varying for the three transfer-laminated electrodes. The ΔU, was largest for LTO/C(1.5), intermediate for LTO/C(2.6), and smallest for LTO/C(3.3), with ΔU=56, 50 and 44 mV, respectively. The error bars for LTO/C(1.5) were larger than for LTO/C(2.6) and LTO/C(3.3), indicating poor reproducibility for transfer-lamination electrodes produced at low pressures. In case of LTO/C(1.5), the removal of the glass-fiber filter from the low compressed LTO/C layers may have lifted or detached more LTO/C agglomerates than for stronger compressed LTO/C layers.

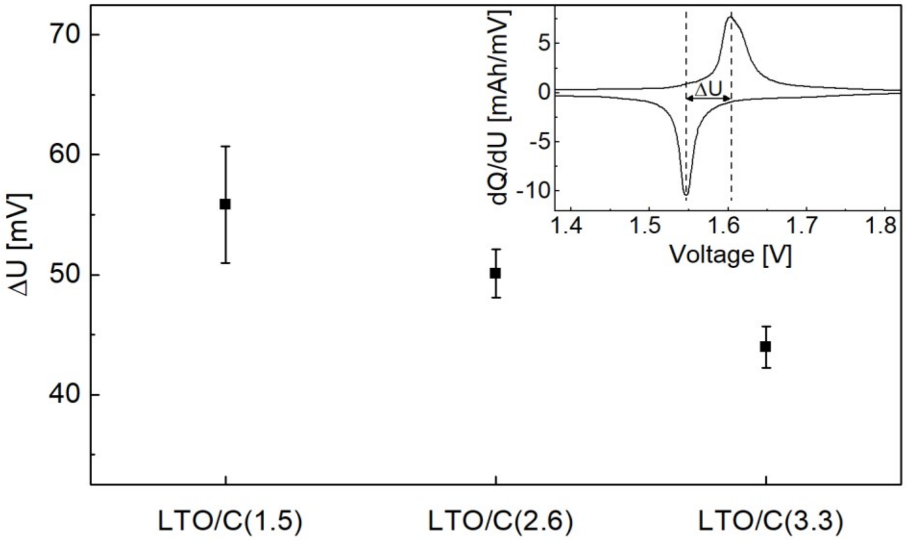

Fig. 9.5 The inset shows a differential plot of LTO/C(1.5) (200th cycle, 1C) exemplary for the transfer-laminated electrodes. The main figure shows the difference (Δ*U*) between oxidation and reduction peaks for LTO/C(1.5), LTO/C(2.6) and LTO/C(3.3) (adapted with permission from [97]).

Galvanostatic dis-/charge potential profiles for the laminated electrodes, obtained at rates of 1C and 10C, are presented in **Fig. 9.6a**. Discharge at 1C, resulted in flat voltage plateaus at ~1.55 V for all three samples, corresponding to the two-phase lithiation reaction of LTO [74,92,150,151]. Also the curved voltage profile, as typical for nano-sized LTO [30,92], was comparable for all three laminated electrodes. At 10C, the shortening of the plateau length and the curved profile character was more pronounced for all three laminated electrodes compared to 1C. While comparing the three battery-cell types at 10C, increasing transfer-lamination pressures led to (1) less developed deviation from the voltage plateau position (~1.55 V), (2) less pronounced profile curving, (3) and larger RCR.

The RCRs at dis-/charge rates of C/5, C/2, 1C, 2C, 5C, 10C and 25C are displayed in **Fig. 9.6b**. All laminated electrodes experienced capacity fading upon rate increments due to increasing overpotentials [39,152]. The drops were comparable among the three electrode types at low C-rates of C/5-2C. At higher C-rates of 5C-25C, overpotentials were smaller for greater transfer-lamination pressures. Exemplarily, at 25C, LTO/C(1.5), LTO/C(2.6) and LTO/C(3.3) achieved RCRs of 43, 66 and 75%, respectively, indicating best high rate reaction kinetics for strongest compressed LTO/C(3.3). Analogous to the discussion on **Fig. 9.4**, the lower overpotentials for higher compressed samples observed in differential curves (**Fig. 9.5**), galvanostatic cycling (**Fig. 9.6a**) and rate tests (**Fig. 9.6b**) were attributed to the improved long-range electrical conductivities in the denser LTO/C particle networks.

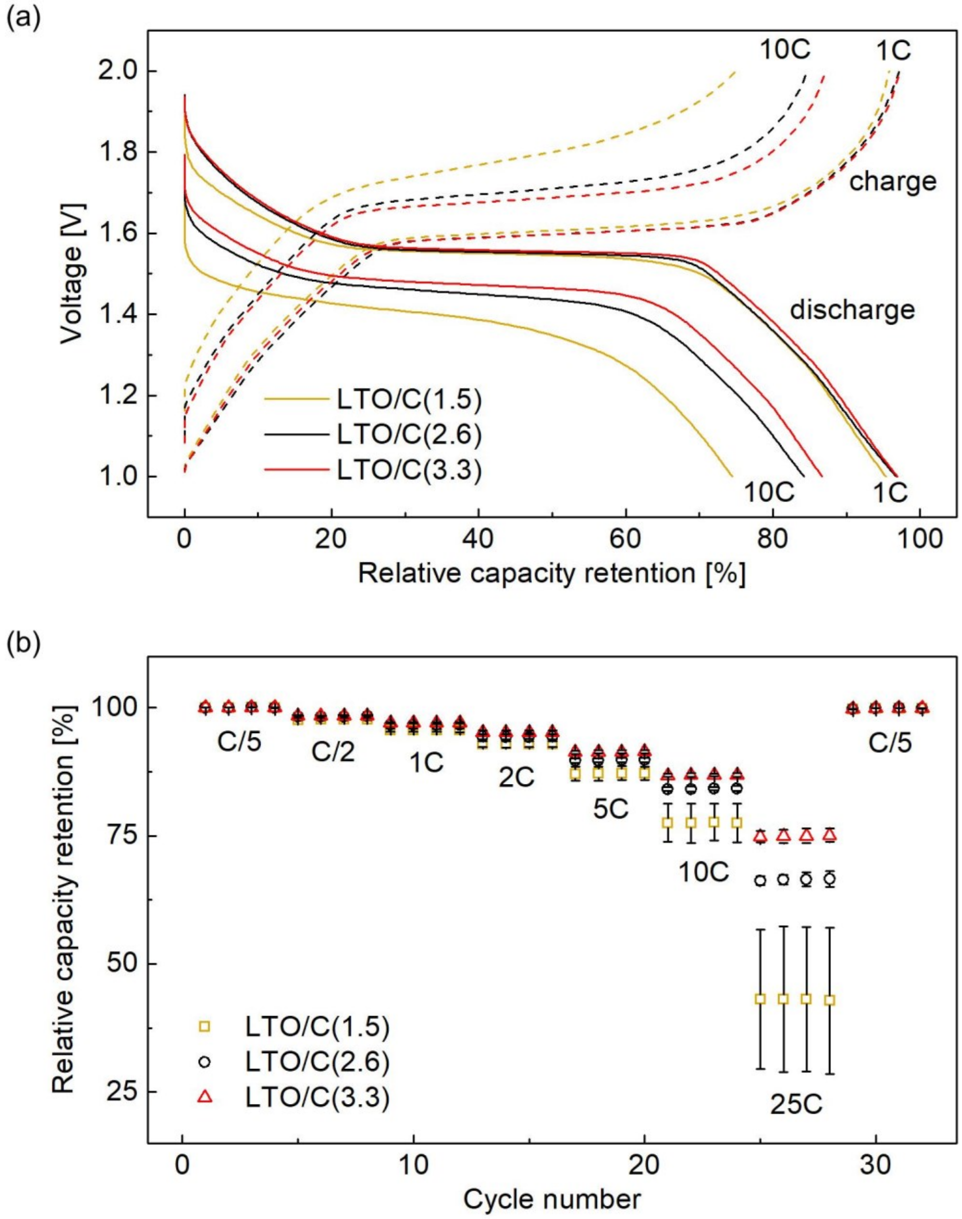

Fig. 9.6 (a) dis-/charge curves of laminated LTO/C(1.5), LTO/C(2.6) and LTO/C(3.3) at 1C and 10C, **(b)** rate performance of laminated electrodes spanning C-rates from C/5 to 25C (adapted with permission from [97]).

To assess the viability and competitiveness of the proposed one-step solvent and binder-free transfer-lamination technique, the battery-cell performance of LTO/C(3.3) was compared to electrodes manufactured by state-of-the-art, slurry-based doctor blading technique. The applied pressures for the fabrication of transfer-laminated electrodes were fairly low compared to industrially applied calendering pressures of 6-80 tons [153]. Therefore, doctor bladed electrodes were electrochemically characterized in as-prepared (LTO/C(DBap)) and calendered (LTO/C(DBc)) condition. The comparison of long-term performances at 1C, derived from LTO/C(3.3), LTO/C(DBap) and LTO/C(DBc), is depicted in **Fig. 9.7a**. The doctor bladed electrodes experienced a capacity fading behavior similar to those of the transfer-laminated sample LTO/C(3.3). After 200 cycles, LTO/C(3.3) performed better than LTO/C(DBap) and slightly better than LTO/C(DBc), with 87.4, 85.1 and 86.6%, respectively. Despite an almost three times higher film thickness than the thinner slurry-based electrodes (**Table 1**), the homogeneous microstructure of LTO/C(3.3) promoted highly beneficial de-/intercalation kinetics.

The rate test performance of LTO/C(3.3) was compared to LTO/C(DBap) and LTO/C(DBc) (**Fig. 9.7b**), to detect effects of microstructural differences on high rate capabilities. A similar trend in RCR losses was perceived for all electrodes at C/5-2C. For rates larger than 2C, LTO/C(3.3) exhibited significantly higher RCR. At 25C, LTO/C(3.3), LTO/C(DBap) and LTO/C(DBc) revealed RCRs of 75.1, 69.6, and 55.1%, respectively.

By comparing the transfer-laminated LTO/C(3.3) microstructure to those of the doctor bladed electrodes, it had to be considered that the overall electrode performance is generally sensitive to electrical and ionic conductivities. While the electrical conductivity is mostly dependent on the contact area of the electrically conductive electrode network, the ionic conductivity is related to electrode active material size [32], pore structure and sufficient electrolyte accessibility [154]. Since the excessive carbon content was 25 wt% in both transfer-laminated and doctor bladed electrodes, the relatively poorer performance of the latter (despite three times thinner electrode layer) was ascribed to meager ionic charge transport properties. In fact, the ionic conductivity in doctor bladed electrodes may have suffered from the partially dense and irregular microstructures (**Fig. 8.1e,f**), as it may have led to a local clogging of lithium-ion diffusion pathways and thus a poor accessibility of lithium-ion intercalation sites. The regular and well-accessible pore structure of LTO/C(3.3), in contrast, was easily permeable to the ionically conductive electrolyte. This allowed good lithium-ion accessibility of LTO de-/intercalation sites [154,155], leading to the relatively improved cycling performance at 1C. Likewise, the beneficial high-rate capability of LTO/C(3.3) was attributed to the homogeneous and accessible microstructure, allowing an advantageous tradeoff between ionic and electrical charge transports.

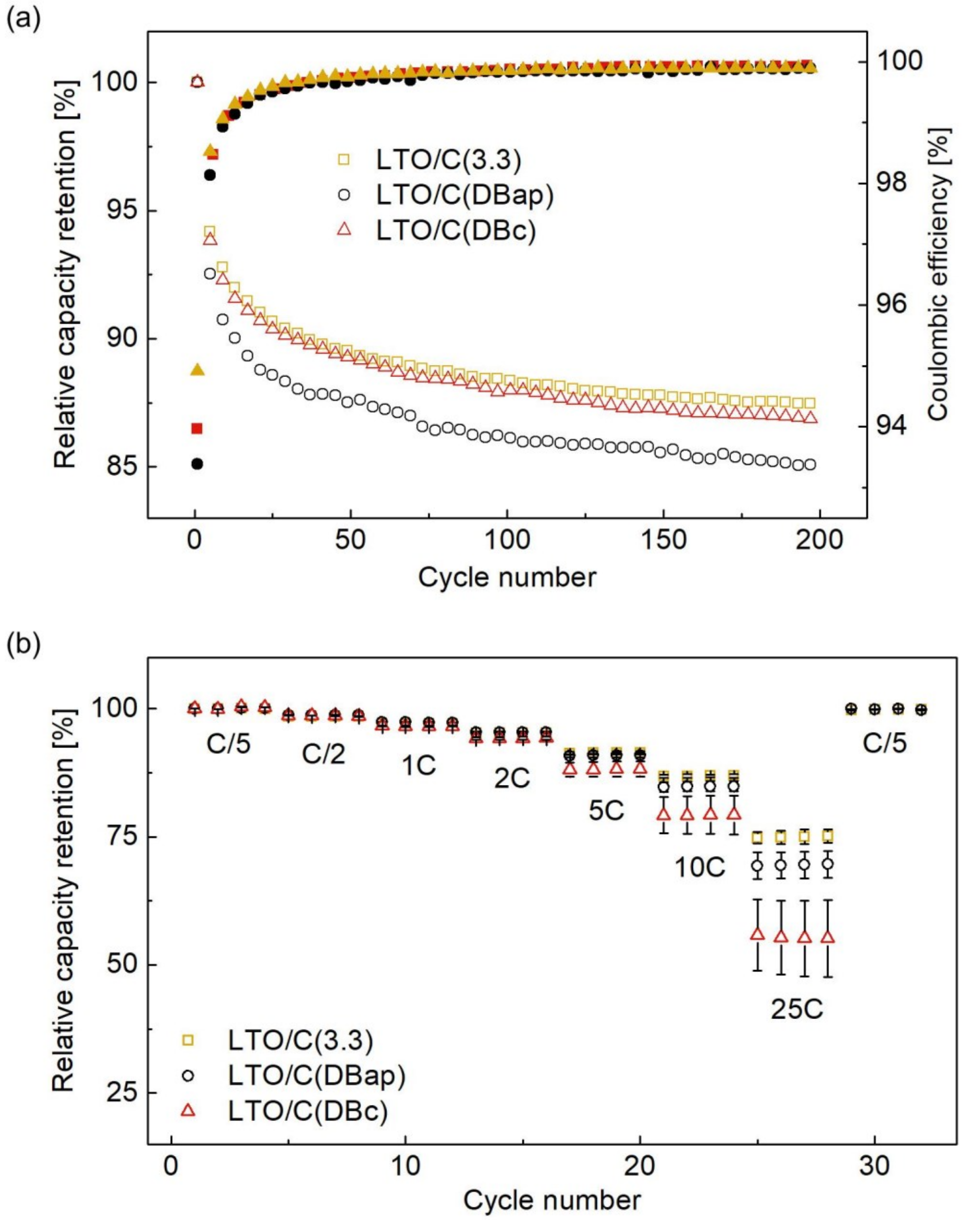

Fig. 9.7 (a) long term cycling and **(b)** rate capability of LTO/C(DBap), LTO/C(DBc) and LTO/C(3.3) (adapted with permission from [97]).

The cycling performance comparison of LTO/C(DBap) and LTO/C(DBc) at 1C (**Fig. 9.7a**), showed an improved RCR for the latter, which most likely stemmed from newly established long-range electrical contacts in the calendered LTO/C layer itself, as well as to the current collector foil [156]. Considering the high-rate measurements (**Fig. 9.7b**), it became evident that the calendering step resulted in poorer rate performances for rates larger than 5C. While the calendering caused slightly improved RCRs at 1C due to an enlarged electrically conductive network, it obviously had a negative effect on the high rate capabilities. The strong densification of the overall LTO/C layer may have created additional lithium-ion diffusion barriers that became a kinetically inhibiting factor, eventually, leading to the lower RCRs at high rates [97].

9.3. *In-situ* Deposited $Li_4Ti_5O_{12}$ Thin-Film Electrodes

The electrochemical performance of the LTO(3.3)-electrodes was characterized in flex-TFB configuration with LiPON as solid-state electrolytes and lithium as negative electrodes. Five LTO(3.3) battery-cells were cycled 30 times with a constant current of 2 μA (~1C) (formation cycle excluded). The respective discharge capacities, normalized to the electrode area, *i.e.* areal discharge capacity (ADC), are shown in **Fig. 9.8** and **Table 2**.

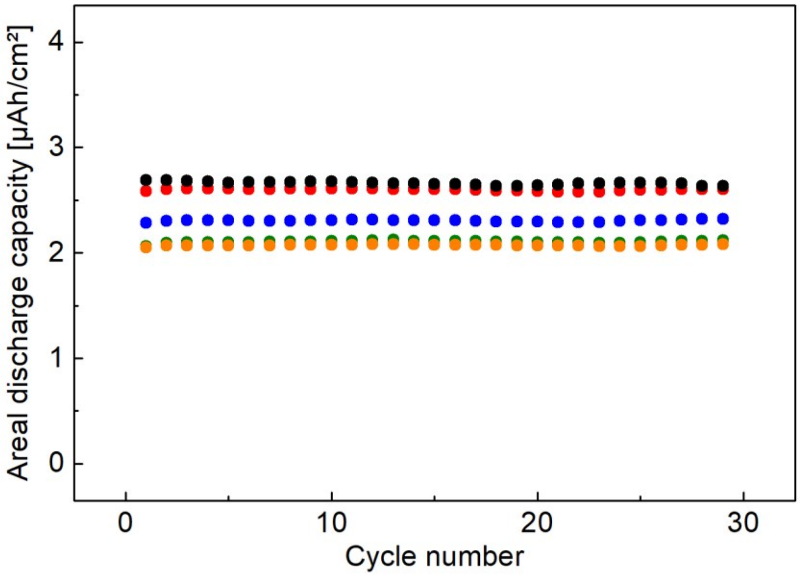

Fig. 9.8 ADCs of LTO(3.3) flex-TFBs *vs.* cycle number, dis-/charged at 2 μA (1C) (adapted with permission from [98]).

Upon cycling, all LTO(3.3) battery-cells revealed remarkably stable electrochemical performances without any indication of capacity fading. However, significant variations in ADCs were observed. **Table 2** contains data related to the five assembled LTO(3.3) flex-TFB cells, including obtained ADCs, LTO(3.3) loadings, maximum possible capacities, actually measured capacities, calculated practicable capacities, and porosities. The best and worst performing battery-cells obtained reversible ADCs of 2.7 and 2.1 μAh/cm², respectively. These deviations were in the first instance ascribed to variations in the LTO loading that were differing significantly from 13 to 29 μg. The inconsistent loadings in turn were attributed to unfavorable interactions of the sample holder geometry and the turbulent FSP aerosol stream. The rather thick shadow mask (2 mm) possibly caused uncontrollable shading effects and related irregular particle deposition in close vicinity to the hole edges. A possible relationship between both the loadings and the observed ADCs for the electrodes was, therefore, investigated. A greater loading, for instance, theoretically provided higher ADCs. By comparing the LTO loadings to the actual ADCs, this assumption was contradicted and the loadings were found unaccountable for the observed deviations. Practicable capacities, *i.e.* percentage of the maximum theoretical capacity to the actually measured absolute capacity in the 2nd cycle, were calculated. First, maximum possible ADCs per electrode were determined by multiplying the LTO loading with the maximum theoretical capacity of LTO, *i.e.* 175 mAh/g. The actually measured ADCs were then divided by the maximum possible ADCs, providing the practicable capacities. In close consideration of the five prepared LTO(3.3) electrodes, the practicable capacities showed that less than 100% of the LTO(3.3) material was involved in de-/intercalation reactions in each case.

Table 2: LTO(3.3) flex-TFB properties (adapted with permission from [98]).

Sample	ADC [µAh/cm²]	LTO(3.3) loading [µg]	Maximum capacity [µAh]	Measured capacity [µAh]	Practicable capacity [%]	Porosity of LTO(3.3) film [%]
1	2.3	13.0	2.3	1.8	78.8	91.3
2	2.1	16.0	2.8	1.6	57.8	89.3
3	2.6	21.0	3.7	2.0	55.2	86.0
4	2.7	23.0	4.0	2.1	52.5	84.7
5	2.1	29.0	5.1	1.6	31.7	80.7

Remarkably, it was found that the practicable capacities were decreasing for increasing loadings. This inverse relationship was related to the overall electron and lithium-ion conduction properties of the LTO(3.3) electrode layers. Additives such as electrically conductive carbon or lithium-ion-conducting electrolyte were absent in the pure LTO(3.3) electrode layer. Necessarily, the higher LTO(3.3) loadings accounted for longer diffusion pathways to the bulk, accompanied by larger overpotentials and thus lower reversible capacities. The high porosities, were accompanied by small conductive contact areas within the particle network, making it kinetically even more problematic to reach overall lithium de-/intercalation sites situated in the bulk.

It was demonstrated that neither the loadings nor the practicable capacities exhibited a linear relationship with the measured ADCs. The LTO(3.3) layer offsets with respect to the copper current collector (cf. **Fig. 8.2a**), may have played a significant role in this aspect. LTO(3.3) particles that were located on insulating Kapton®, instead of the electrically conductive copper current collector, were limited to electron supply *via* the LTO(3.3) particle network. This may have kinetically hindered the electrically unsupported LTO particles, in taking part in electrochemical de-/intercalation reactions. Consequently, the inconsistent variations in ADC and practicable capacities were foremost related to random LTO(3.3) thin-film offsets.

To understand the electrochemical performance of LTO(3.3) flex-TFBs phenomenologically, the electrochemical dis-/charge performance for the battery-cell with the largest ADC is presented in **Fig. 9.9**.

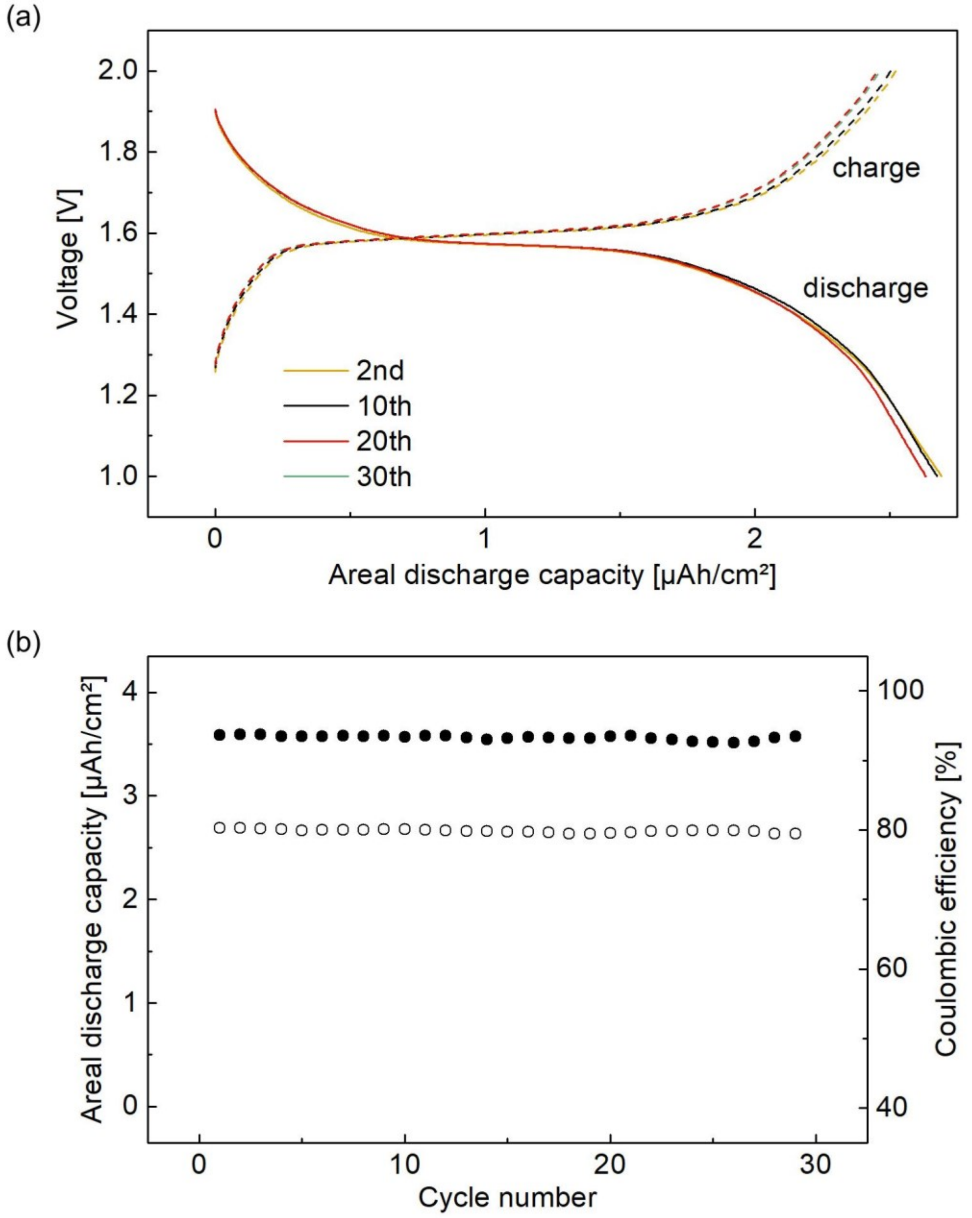

Fig. 9.9 (a) Exemplary dis-/charge curves and **(b)** ADCs (hollow) and coulombic efficiency (solid) of a LTO(3.3) flex-TFB cell (adapted with permission from [98]).

The battery-cell showed extraordinarily reversible potential dis-/charge profiles from 2nd to 10th, 20th and 30th cycles (**Fig. 9.9a**) with a constant ADC of ~2.7 µAh/cm². The coulombic efficiency was stable at around 93 % after the formation cycle (**Fig. 9.9b**). Differential capacity curves in **Fig. 9.10,** also indicated that overpotentials were unaffected by cycle number since oxidation and reduction peak positions, intensities, and widths were coherent.

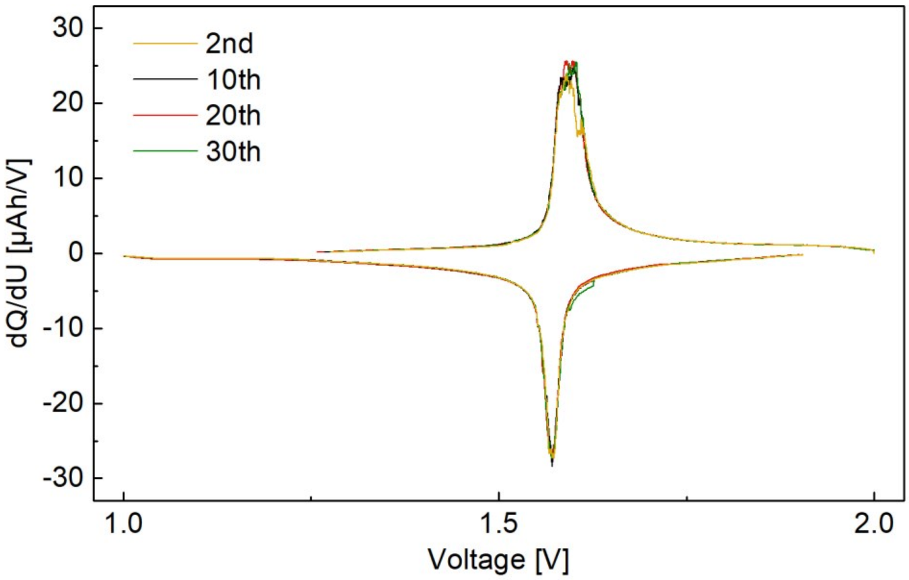

Fig. 9.10 Differential curves obtained from LTO(3.3) in the 2nd, 10th, 20th and 30th cycles at 2 µA (1C) (adapted with permission from [98]).

Application of larger currents (**Fig. 9.11a**) revealed typical susceptibility to overpotentials: the plateau potential increasingly deviated from the original potential of ~1.55 V at 1 µA (0.5C), while the plateau length parallel to the abscissa has clearly reduced. The determined ADCs at currents of 1 µA (~0.5C), 2 µA (~1C), 4 µA (~2C), 6 µA (~3C), 10 µA (~5C) and 1 µA (~0.5C), were 2.9, 2.6, 2.2, 1.9, 1.7 and 2.9 µAh/cm², respectively (**Fig. 9.11b**). Similar ADCs at initial and final cycles indicated high reversibility even after applying higher currents.

LTO(3.3) electrodes were bendable without causing LTO detachment, as shown in **Fig. 9.12a**. **Fig. 9.12b** shows a LTO(3.3) flex-TFB fixed into a custom-made sample holder, designed for static bending tests. To investigate the effect of static flex-TFB bending on the LTO reaction kinetics, two battery-cells were dis-/charged 30 times flat, bent (radius=7.5 mm) and again flat (postbent).

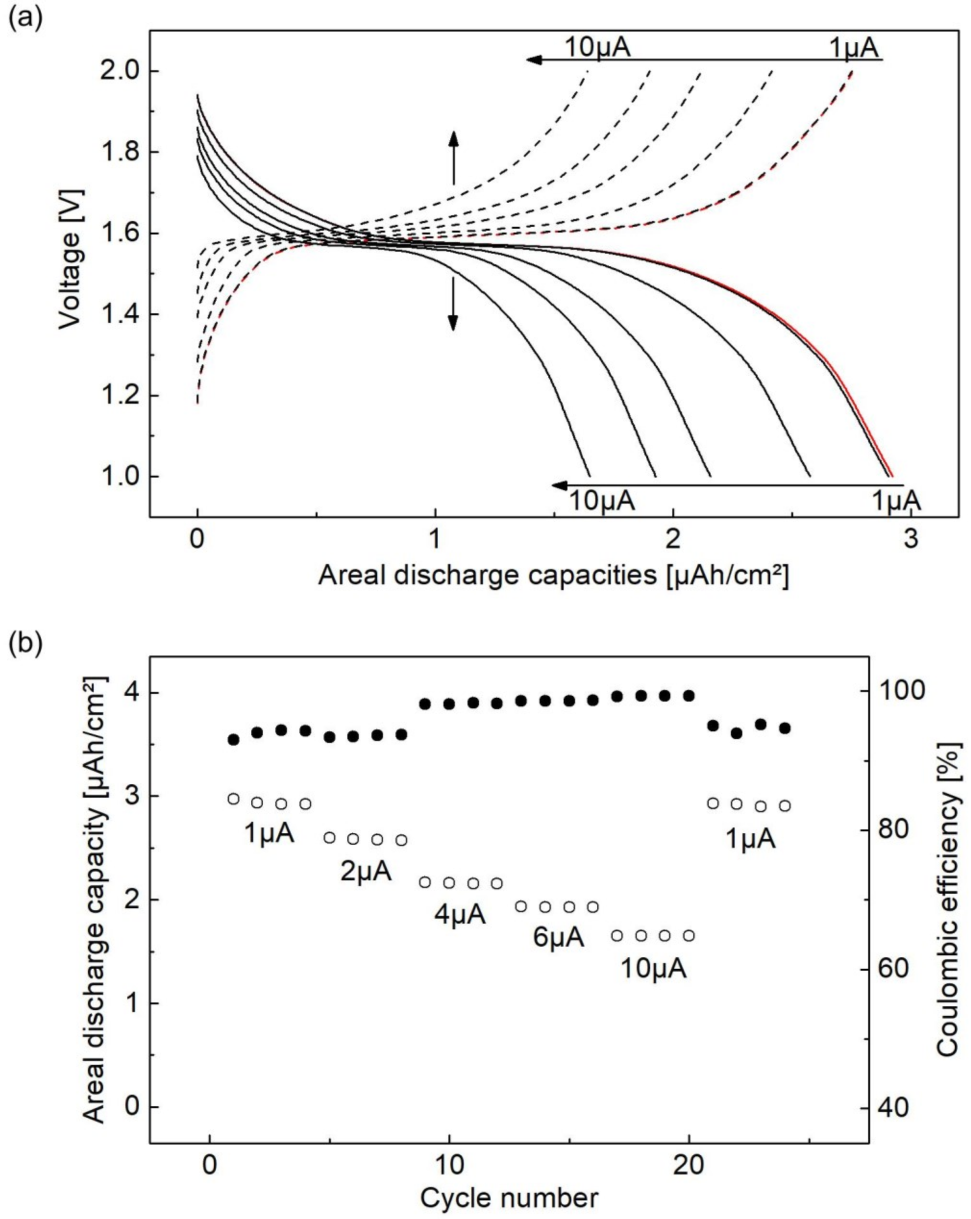

Fig. 9.11 (a) dis-/charge curves and **(b)** ADCs (hollow) and coulombic efficiency (solid) for LTO(3.3) battery-cells dis-/charged at 1 µA (0.5C), 2 µA (1C), 4 µA (2C), 6 µA (3C), 10 µA (5C) and 1 µA (0.5C). The red line in (a) illustrates a final reproducibility cycle at 1 µA (0.5C) (adapted with permission from [98]).

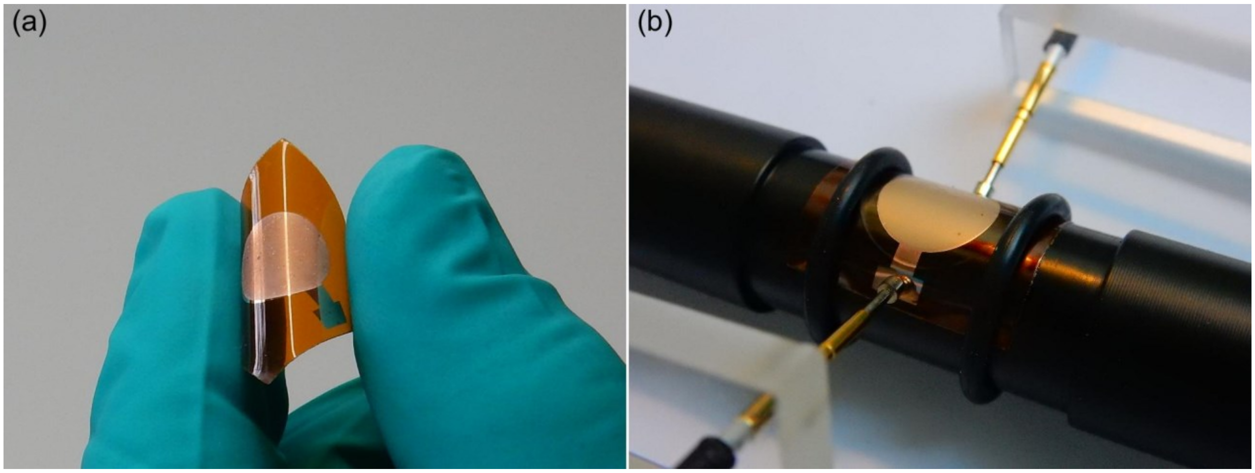

Fig. 9.12 (a) Photographies of a bend LTO(300) electrode and **(b)** a LTO(3.3)-based flex-TFB, fixed in the custom-built mechanical bending apparatus in static condition (adapted with permission from [98]).

As demonstrated in **Fig. 9.13**, ADCs in flat, bent and postbent condition were 2.6, 2.0, 2.1 μAh/cm² and 2.3, 2.1, 2.1 μAh/cm² for the two different battery-cells (differentiated by solid and hollow symbols). The sample holder was changed after 30th and 60th cycle to realize battery-cell measurements in bent and postbent condition, respectively [157]. The observed decrease in ADCs after the 30th cycle, was attributed to contact losses induced by mechanical stresses upon battery-cell bending.

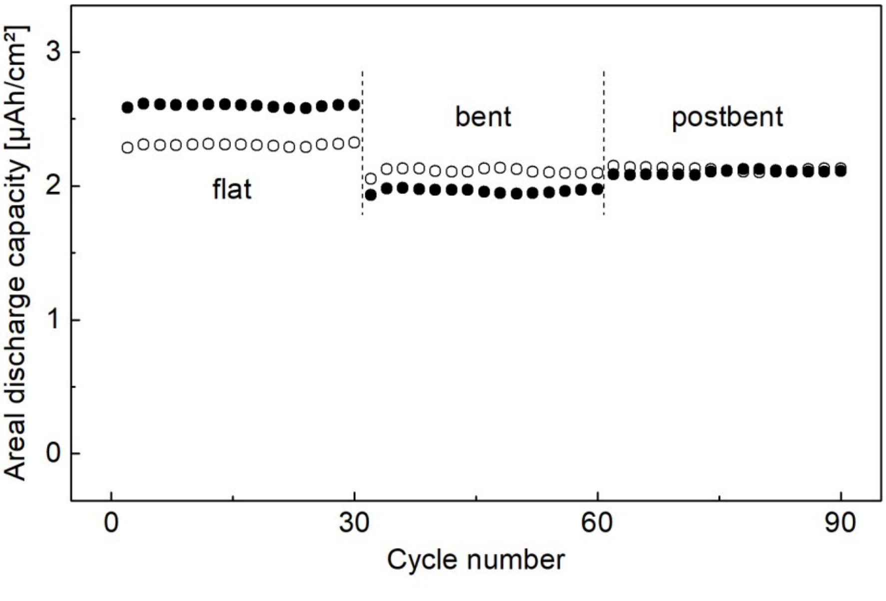

Fig. 9.13 ADCs of LTO(3.3) flex-TFB cells cycled at 2 μA (1C) in pre-bent, bent and postbent condition. Dashed lines indicate change from flat to bent state, and vice versa (adapted with permission from [98]).

In postbent condition (60th cycle), abrupt losses in ADCs were absent. On contrary, instead of ADC drops, the battery-cell represented by filled symbols, showed a slight increase in ADC. This indicated that a certain amount of lost contacts was reconstituted upon stress-release from battery-cell bending. Eventually, bending tests showed feasibility of LTO(3.3) flex-TFB cell bending in static condition.

9.4. Effect of $Li_4Ti_5O_{12}$ Thin-Film Microstructure on Electrochemical Performance

Two battery-cells each, for LTO(300) and LTO(3.4), were electrochemically tested as shown in **Fig. 9.14**. The loadings for the battery-cells were comparable with 50.8 ± 1.8 μg [126].

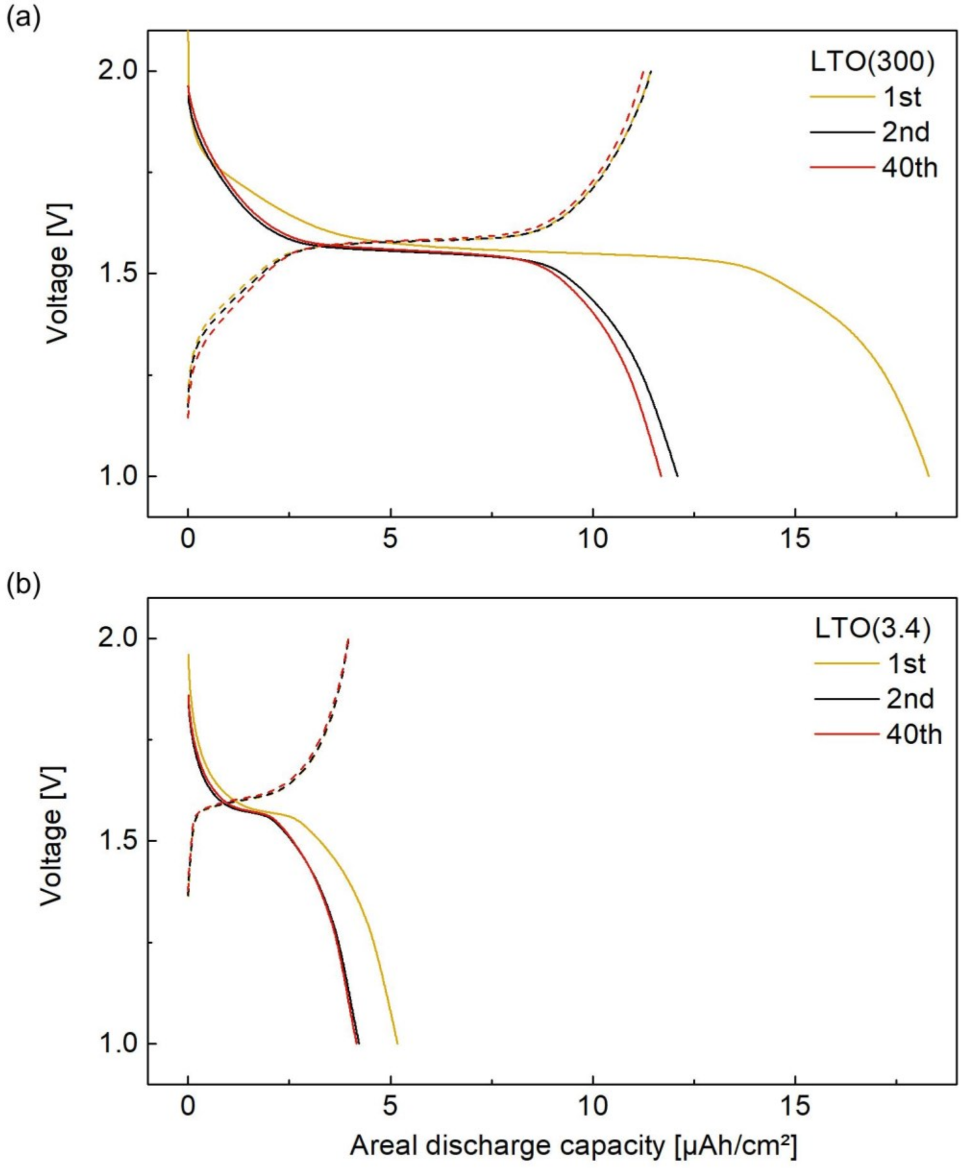

Fig. 9.14 Dis-/charge curves derived at 2 μA for **(a)** LTO(300) in the 1st, 2nd and 40th cycles, showed longer plateaus and larger ADCs than **(b)** LTO(3.4) (adapted with permission from [126]).

The more reproducible loadings were a remarkable improvement compared to the LTO(3.3) electrodes (**Table 2**) and suggested that possible electrochemical performance differences were independent of loading variations. Dis-/charge curves for cycling of LTO(300) and LTO(3.4) are shown for the 1st, 2nd and 40th cycle in **Fig. 9.14a**, and **Fig. 9.14b**, respectively. Succeeding the formation cycle, dis-/charge reaction kinetics were reversible since changes in plateau height and length were negligible. The corresponding ADCs of 2nd and 40th cycle were steady at around 11.6 µAh/cm² for LTO(300), while those of LTO(3.4) were around 4.5 µAh/cm² (**Fig. 9.15a)**.

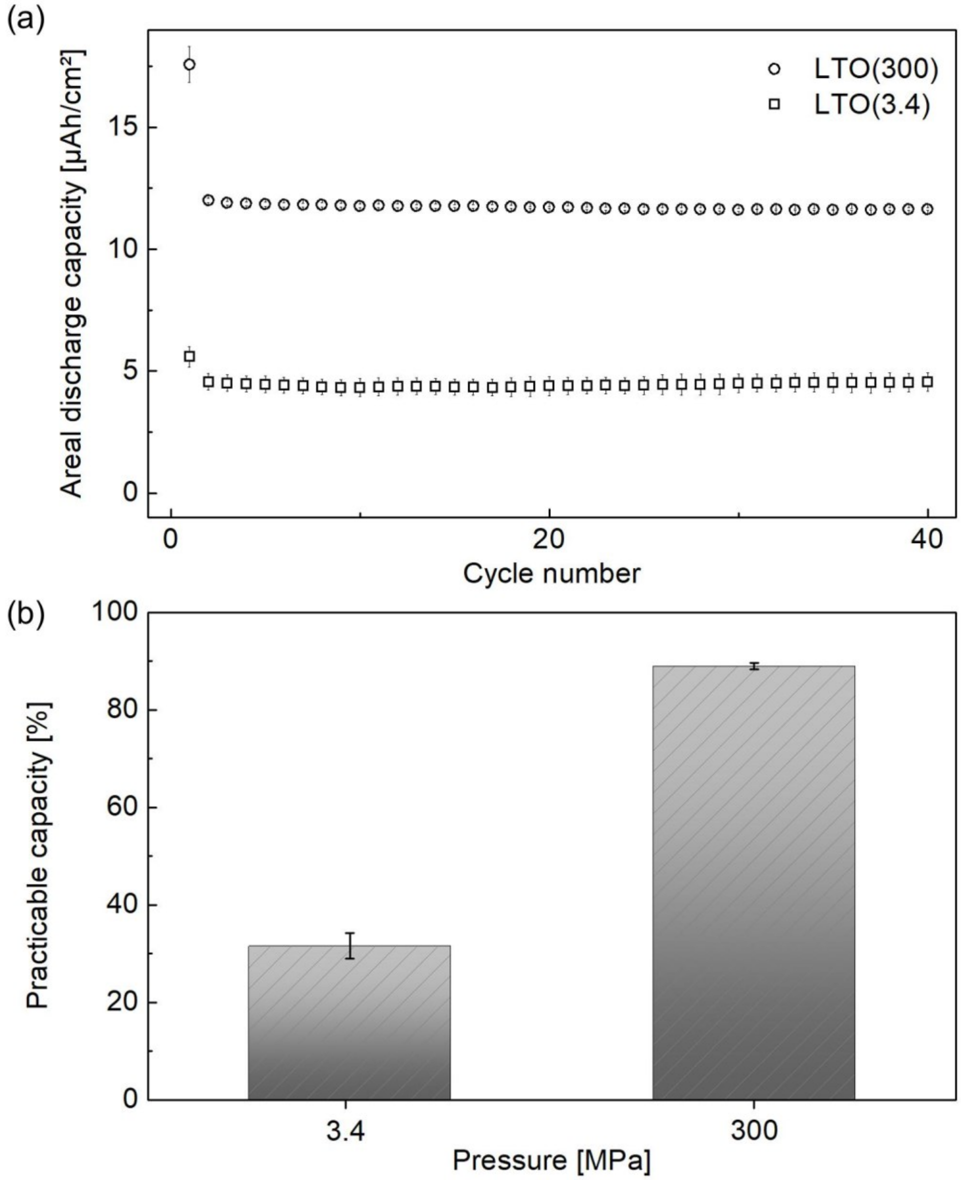

Fig. 9.15 The **(a)** ADCs and **(b)** practicable capacities of LTO(300) and LTO(3.4) (adapted with permission from [126]).

LTO(300) presented a practicable capacity of 88.2%, (~154 mAh/g) while LTO(3.4) showed only 31.2% (~54.6 mAh/g), which was a remarkable enhancement of 183% of the reversible discharge capacity (**Fig. 9.15b**). Normalized to the layer thicknesses of LTO(300) and LTO(3.4), the two electrode types provided volumetric discharge capacities of 28 and 4-6 µAh/cm²·µm, respectively. The pulsed laser deposited LTO thin films of Schichtel *et al.*, had ADCs of 33 µAh/cm² at 3.5 µA/cm². Considering a thickness of 650 nm, their volumetric discharge capacities were ~50 µAh/cm²·µm, which was almost two times greater than obtained for LTO(300) [126,158].

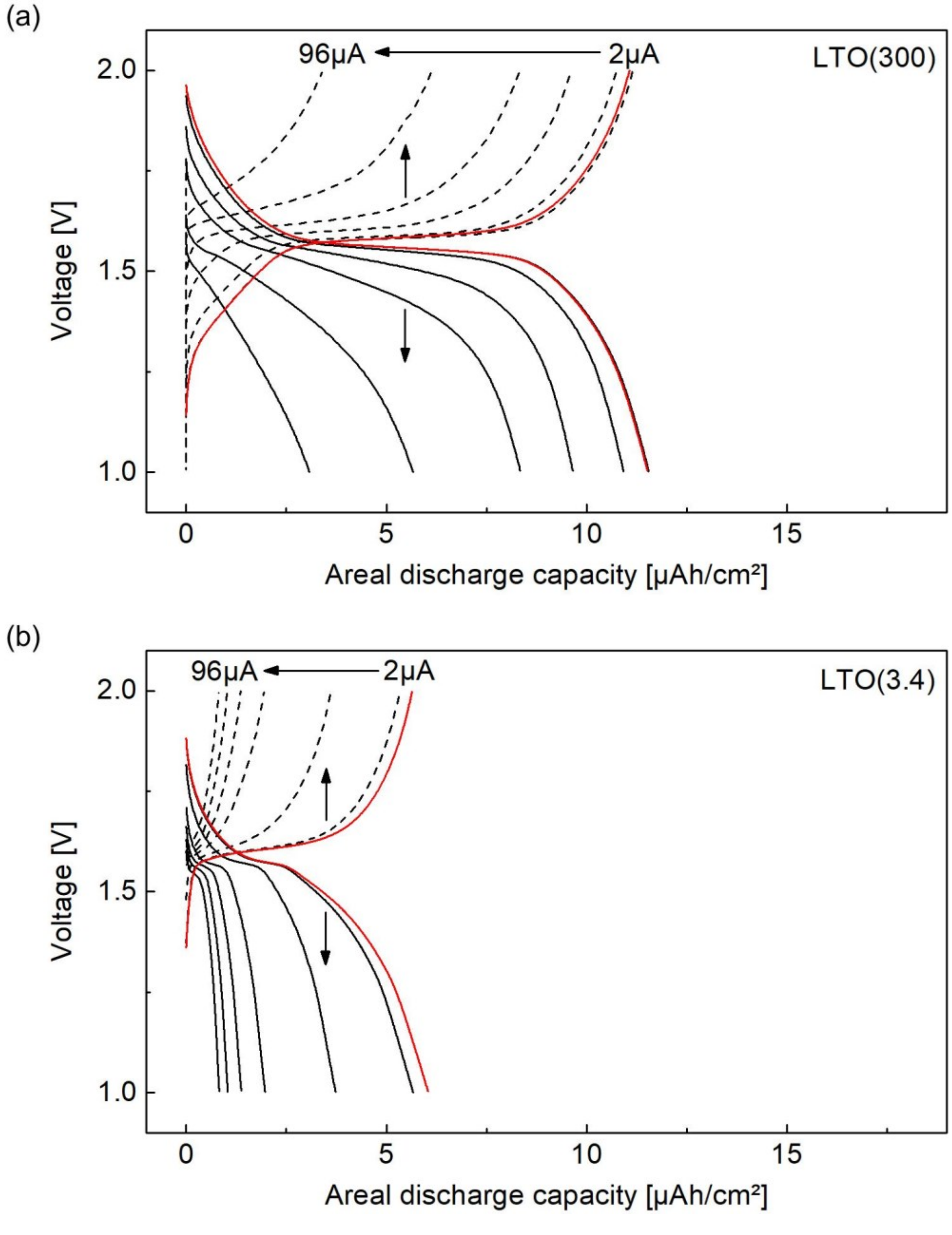

Fig. 9.16 The dis-/charge curves derived from rate tests at 2, 4, 12, 24, 48 and 96 µA for **(a)** LTO(300) showed more favorable dis-/charge reaction kinetics than those of **(b)** LTO(3.4). The red lines in (a) and (b) illustrate the final rates at 2 µA for reproducibility (adapted with permission from [126]).

The improved performance of the pulsed laser deposited thin films was ascribed to the significantly lower porosities of the bulky LTO films. In terms of practicable capacity, however, the pulsed laser deposited LTO layers showed a poorer performance than LTO(300), with ~58.0 and 88.2%, respectively. The larger practicable capacities of porous LTO(300) films arose most likely from lower loadings and lower related overpotentials. By reducing the residual porosity of LTO(300) and concomitantly increasing the loading, the electrochemical performance may have approximated that of denser LTO layers synthesized by Schichtel *et al.* [158].

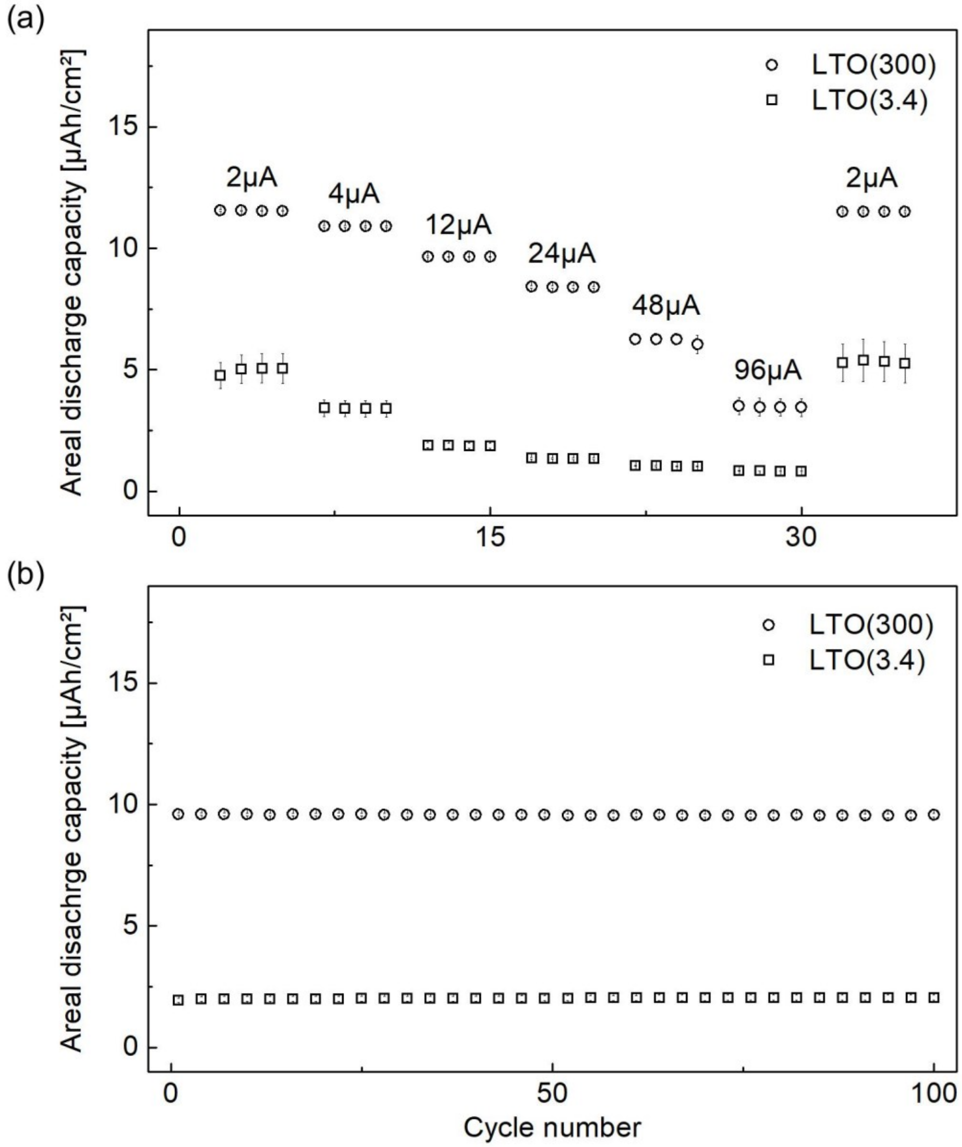

Fig. 9.17 (a) high-rate capability of LTO(300) and LTO(3.4), **(b)** long term cycling performances of LTO(300) and LTO(3.4) at 12 µA. Cycling stability was given for 100 cycles for both battery-cell types, while higher ADCs are obtained for LTO(300) (adapted with permission from [126]).

Dis-/charge curves extracted from rate tests of LTO(300) and LTO(3.4) are presented in **Fig. 9.16a** and **Fig. 9.16b**, respectively. With increments in current rates, LTO(300) plateau lengths have reduced while deviations from plateau height at ~1.55 V have increased due to growing overpotentials. The very same behavior was observed for LTO(3.4), however, the plateau lengths of LTO(3.4) were clearly shorter than those of LTO(300). At rates of 2, 4, 12, 24, 48, 96 and 2 μA, LTO(300) and LTO(3.4) presented ADCs of 11.5, 10.9, 9.6, 8.4, 6.2, 3.4, 11.5 μAh/cm² and 5.0, 3.4, 1.9, 1.3, 1.1, 0.9, 5.3 μAh/cm², respectively (**Fig. 9.17a**). The losses in ADCs for LTO(300) and LTO(3.4) from lowest to highest rate were 70% and 82%, respectively, showing enhanced capacity retention for LTO(300). The similar ADCs of the first and final (red lines) 2 μA cycles, implied reversible battery-cell kinetics even after high rate application. The cycling stability over 100 cycles (12 μA ≈ 1.3C) was excellent for both electrode types as presented in **Fig. 9.17b**. Here, LTO(300) and LTO(3.4) showed reversible ADCs of 9.6 and 2.0 mAh/cm², respectively.

9.5. Cyclic Voltammetry

The three LIB battery-cell types LTO_{LNT}, LTO_{LTB} and LTO_{LAA} were tested with CV to examine the occurring redox reactions and their reversibility. **Fig. 9.18a** shows voltammograms of LTO_{LNT}, LTO_{LTB} and LTO_{LAA}, recorded at scan rates of 0.2, 0.5 and 1.0 mV/s, with similar redox profile characteristics. Phase-pure LTO, in absence of any overpotentials, has two characteristic CV peaks, *i.e.* negative cathodic (LTO reduction/battery-cell discharge) and positive anodic (LTO oxidation/battery-cell charge) peaks, at 1.60 and 1.55 V, respectively. The resulting peak separation distance, *i.e.* dU_{CV}, is 50 mV. At a scan rate of 0.2 mV/s, the three battery-cell types LTO_{LNT}, LTO_{LTB} and LTO_{LAA}, revealed the same distinct anodic and cathodic peaks, however, they were located at around 1.67 and 1.48 V, respectively [98,150]. The difference between both peaks (dU_{CV}) for each sample was thus around 190 mV. Consequently, the three battery-cell types LTO_{LNT}, LTO_{LTB} and LTO_{LAA}, measured at 0.2 mV/s, were phase-pure (in accordance with XRD results) but exhibited overpotentials [159].

Increments in scan rate have further separated the cathodic and anodic peak positions. For scan rates of 0.5 and 1.0 mV/s, peak extreme values were located at 1.72, 1.78 V (anodic peaks) and 1.43, 1.41 V (cathodic peaks), with dU_{CV} of 290 and 370 V, respectively. Likewise, the peak intensities grew with increasing rates, while they were scaling linearly with the square root of the scan rate (**Fig. 9.18b**). The linear relationship suggested that the occurring redox reactions were diffusion-controlled, rather than surface-controlled [160,161]. Since anodic and cathodic peak currents were comparable in intensity at each individual scan rate, an excellent reversibility of the lithium de-/intercalation process was suggested for each electrode type [162].

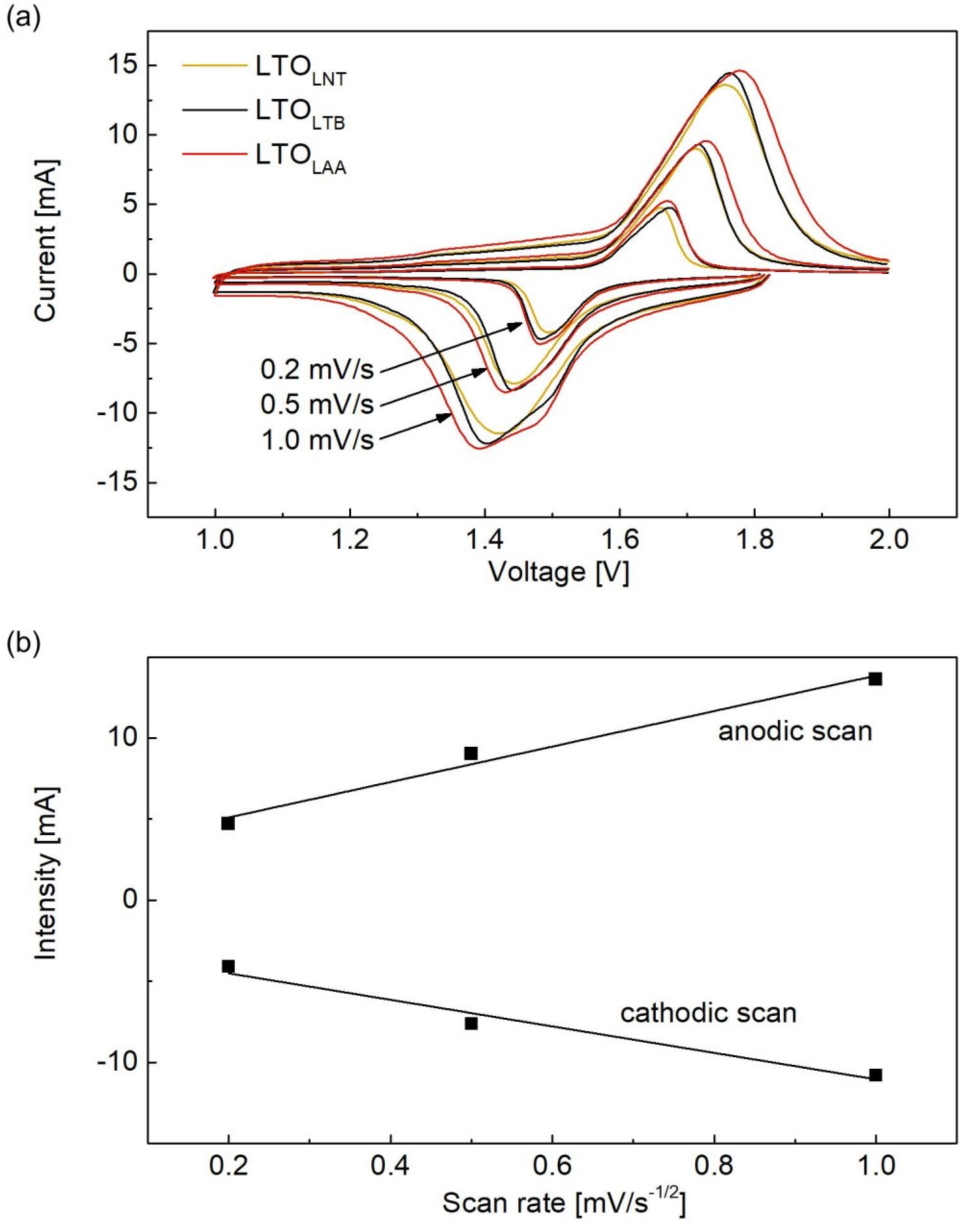

Fig. 9.18 **(a)** Cyclic voltammograms of LTO$_{LNT}$, LTO$_{LTB}$ and LTO$_{LAA}$ pouch cells showed reduction (down) and oxidation (up) peak signals recorded at 0.2, 0.5 and 1.0 mV/s (adapted with permission from [96]), **(b)** Linear relationship between square root of the scan rate and peak intensity, indicating diffusion-controlled redox-reactions.

CV has also been conducted with LTO(3.3), to characterize the reaction kinetics of LTO$_{LAA}$ in an all-solid-state thin-film configuration (**Fig. 9.19a**). At each scan rate, LTO-typical cathodic and anodic peaks were found, indicating LTO phase-purity. While the scan rate was increased from 0.2, 0.5, to 1.0 mV/s, the corresponding peak positions deviated negligibly for anodic (1.55 V) and cathodic plateau potential (1.60 V) peaks with 1.56, 1.56, 1.55 V and 1.60, 1.61, 1.62 V, respectively.

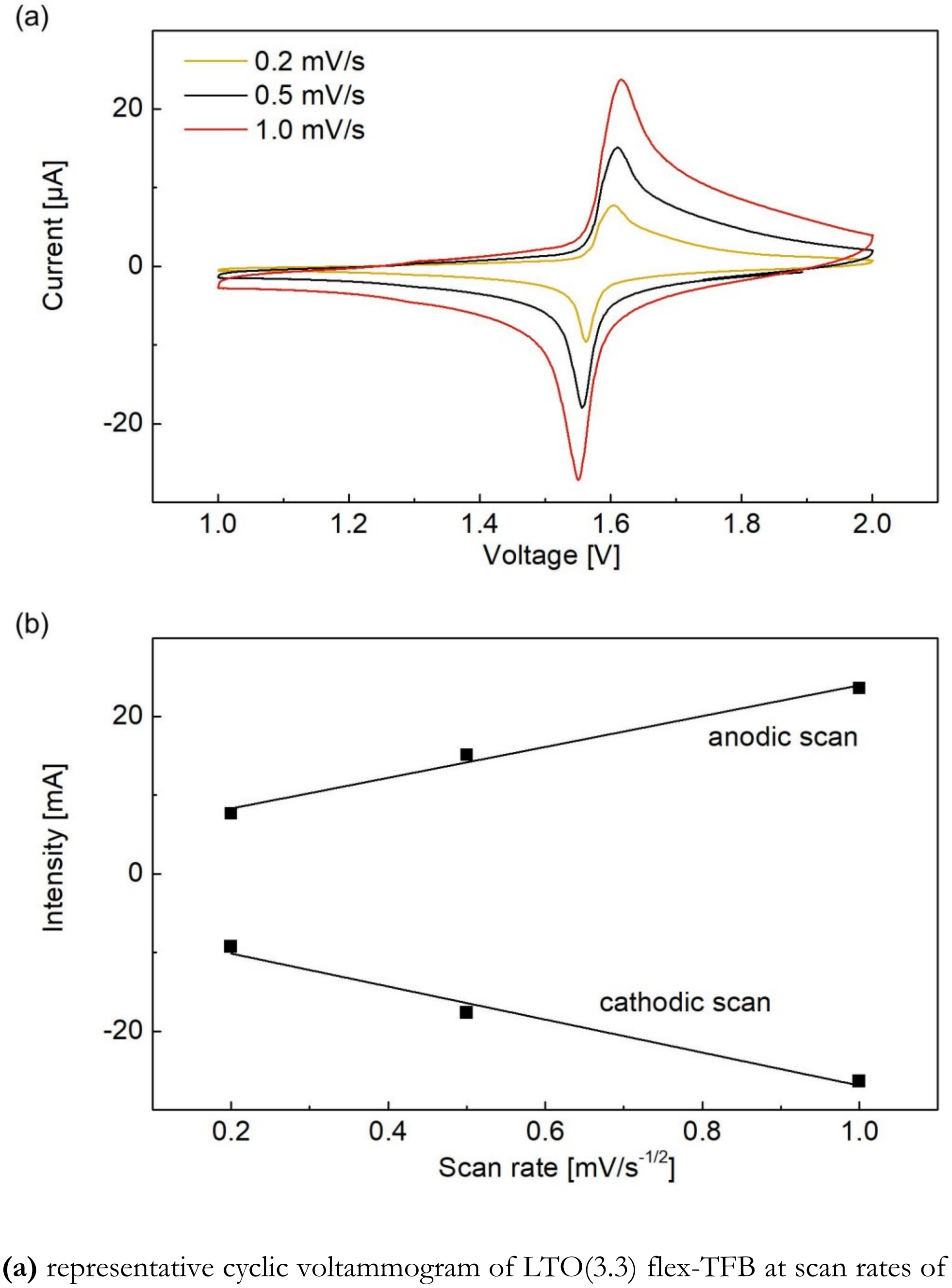

Fig. 9.19 (a) representative cyclic voltammogram of LTO(3.3) flex-TFB at scan rates of 0.2, 0.5, and 1 mV/s, showing charge (positive) and discharge (negative) peaks (adapted with permission from [98]), **(b)** Linear correlation of peak intensity and square root of the scan rate, suggesting diffusion-controlled redox-reactions.

The differences between charge and discharge peaks (dU_{CV}) at 0.1, 0.5 and 1 mV/s were thus 40, 50 and 70 V, respectively. This indicated excellent LTO de-/intercalation reversibility at all three scan-rates. The values were significantly smaller compared to the LTO_{LAA} sample used for LIB fabrication (**Fig. 9.19a**), suggesting less pronounced overpotentials in the thin-film geometry. Analogous to the liquid-electrolyte LIBs, LTO(3.3) scaled linearly with the square root of the scan rate (**Fig. 9.19b**), suggesting diffusion-controlled redox reactions. The pairs of charge and discharge peaks had similar intensities and peak shapes, additionally indicating high purity and reversibility of the LTO(3.3) thin-film configuration.

10. Summary and Conclusion

Three FSP-produced high-purity LTO powders, *i.e.* LTO_{LNT}, LTO_{LTB} and LTO_{LAA}, originating from different precursor solvent combinations, have been fabricated into LIB electrodes *via* doctor-blading. Assembled into LIB pouch-cells, all three powders revealed fairly good reversible capacities around 160 mAh/g for 450 cycles. The comparable electrochemical performance showed that all three precursor-solvent combinations were suitable to synthesize high-quality LTO *via* FSP. This fact allows the battery manufacturer to choose that precursor-solvent combination which is most suitable in terms of his ecologic and economic demands.

Based on the FSP synthesis of LTO_{LAA}, three LTO/C electrode batches, prepared from a DFSP/transfer-lamination technique with applied pressures of 1.5, 2.6 or 3.3 MPa, were microstructurally characterized. It has been found *via* SEM-FIB investigations that the superior electrochemical performance at higher transfer-lamination pressures was due to an enlarged electrically conductive network [97]. In comparison, conventionally prepared doctor bladed electrodes of LTO/C composites, showed less regular microstructures. They performed comparable to transfer-laminated LTO/C(3.3) at low, but inferior at higher dis-/charge rates. The superior performance of LTO/C(3.3) was related to the highly regular microstructure, offering an expanded electrically conductive network, while providing readily accessible lithium-ion reactions sites [97]. Further advantages of the DFSP/transfer-lamination technique are a possible cost-efficient and "green" processing, since (1) both the active material and the carbon additive can be autonomously synthesized, allowing adjustments in LTO/C constitution, (2) the electrode fabrication itself is significantly simpler and faster without needing electrochemically inactive organic binders or carcinogenic solvents for fabrication of regular electrode films. Thus, DFSP/transfer-lamination offers potential economic and ecologic advantages compared to the conventionally applied doctor blading technique [163,164].

This work also demonstrated that the FSP method can be applied for the fabrication of all-solid-state thin-film battery electrodes. The polycrystalline LTO thin-films were *in-situ* deposited to flexible polymer substrates without any sintering step for obtaining LTO crystallization. Assembly of functional flex-TFBs required mechanical compression (3.3 MPa) of LTO thin-films to provide layer stability. Compressed LTO(3.3) electrodes were assembled into flex-TFBs and revealed extraordinary cycling stability at various rates. The LTO loadings were, however, strongly varying and showed an inverse relationship to the practicable capacities, *i.e.* poorer efficiency for higher loadings. It was concluded that thicker LTO layers were accompanied with growing kinetic hindrances in charge transport since lithium-ion and electrically conductive additives were absent. Cycling the flex-TFBs in static bent state, caused a little drop in capacity, followed by highly reversible cycling. After releasing the stress, the ADCs were slightly increased. This indicated that the LTO particle network, in absence of any binder, experienced mechanical contact losses upon bending that were partly reversible.

After optimizing the prototypic FSP *in-situ* deposition setup, reproducible LTO thin-film production became possible. Further, it was found *via* SEM-FIB, BET and simulative studies, that a drastic LTO thin-film compression led to lower residual porosities with (1) increased LTO particle coordination numbers, and (2) larger contact densities to adjacent functional layers. Both factors, eventually, led to significantly improved practicable capacities of 183% at 1C, compared to a less compressed batch of LTO thin-films. The residual porosity of ~46,6%, may still be beneficial to buffer potential volume changes in the active material upon lithium-ion de-/intercalation.

11. Outlook

Based on the results of the current thesis, following hypotheses are formulated in anticipation of cost-efficient FSP-based LIB and flex-TFB electrode fabrication, with improved electrochemical performances. Validating these hypotheses, may support the transformation of the prototypic FSP-based electrode fabrication techniques to industrial scale production.

Optimizing the transfer-lamination process for LIB fabrication:

- By finding an optimal particle size, roughly in the range of 20-80 nm [95], the high rate capability of LTO electrodes will be enhanced and irreversible formation reactions reduced.
- The energy and power density of LTO/C electrodes will be enhanced by coating the LTO particles with only a slight amount of adequately graphitized carbon.
- Applying metal filters (reusable) for LTO/C collection and transfer-lamination will avoid glass-fiber residues on the LTO/C electrode surfaces.

- Scanning also larger LTO/C transfer-lamination pressures, followed by SEM-FIB investigation and LIB cell assembly and testing, will help to identify residual porosities that are useful for a good percolation of liquid electrolyte and to buffer occurring stresses upon battery-cell dis-/charging.
- High voltage cathode materials such as LMO exhibit larger volume changes. If transfer-laminated LMO electrodes with a controlled porosity can buffer such stresses, full-cell preparation *vs.* graphite or LTO becomes feasible.
- Using warm binder-coated substrates for transfer-lamination, will help to strengthen the mechanical integrity of electrodes that experience volume expansion upon dis-/charging.
- By using a suitable material, the FSP particle collector unit will be useful as separator. Instead of transfer-lamination, the collected LTO/C material only needed to be compressed. If a critical LTO/C loading is not surpassed and air-permeability is still given, the separator will be coated from the other side with *e.g.* LMO, in a second step. The double-coated separator sandwich will then be laminated between two current collectors that are possibly coated with a binder material.

Optimizing the *in-situ* deposition process for flex-TFB fabrication:

- The lithium-ion conductivity of flexible electrodes will be improved by conformal filling of the open porosity with *e.g.* LiPON, using the atomic layer deposition technique [165].
- The electrical conductivity will be enhanced by *in-situ* depositing a LTO/C composite, using two individual aerosol streams, *i.e.* DFSP technique [97].
- A better understanding of capacity losses upon bending will be obtained by characterizing LTO flex-TFB cells using multifrequency impedance spectroscopy in dynamical bending tests.
- A beneficial trade-off between a porous microstructure that provides sufficient charge transport capabilities and buffers volume changes, will enable application of high voltage cathode materials such as LMO with long cycle life and high energy/power densities.

12. References

[1] B. Scrosati, J. Garche, Lithium batteries: Status, prospects and future, J. Power Sources. 195 (2010) 2419–2430.

[2] J.M. Tarascon, M. Armand, Issues and challenges facing rechargeable lithium batteries, Nature. 414 (2001) 359–67.

[3] Y. Wang, B. Liu, Q. Li, S. Cartmell, S. Ferrara, Z. Daniel, J. Xiao, Lithium and lithium ion batteries for applications in microelectronic devices: A review, J. Power Sources. 286 (2015) 330–345.

[4] Y. Zhou, M. Xue, Z. Fu, Nanostructured thin-film electrodes for lithium storage and all-solid-state thin-film lithium batteries, J. Power Sources. 234 (2013) 310–332.

[5] J. Cho, S. Jeong, Y. Kim, Commercial and research battery technologies for electrical energy storage applications, Prog. Energy Combust. Sci. 48 (2015) 84–101.

[6] M. Vetter, L. Rohr, Lithium-ion batteries for storage of renewable energies and electric grid backup, in: Lithium-Ion Batter. Adv. Appl., Elsevier, 2014: pp. 293–309.

[7] M. Sterner, I. Stadler, Energiespeicher – Bedarf, Technologien, Integration, 2nd ed., Springer Vieweg, Berlin, 2017.

[8] V.S. Bagotsky, A.M. Skundin, Y.M. Volfkovich, Electrochemical power sources: batteries, fuel cells, and supercapacitors, John Wiley & Sons, Pennington, NJ, 2015.

[9] J.B. Goodenough, Y. Kim, Challenges for rechargeable Li batteries, Chem. Mater. 22 (2010) 587–603.

[10] A. Mahmoudzadeh Andwari, A. Pesiridis, S. Rajoo, R. Martinez-Botas, V. Esfahanian, A review of battery electric vehicle technology and readiness levels, Renew. Sustain. Energy Rev. 78 (2017) 414–430.

[11] M.A. Hannan, M.M. Hoque, A. Mohamed, A. Ayob, Review of energy storage systems for electric vehicle applications: Issues and challenges, Renew. Sustain. Energy Rev. 69 (2017) 771–789.

[12] P. Van den Bossche, F. Vergels, J. Van Mierlo, J. Matheys, W. Van Autenboer, SUBAT: An

assessment of sustainable battery technology, J. Power Sources. 162 (2006) 913–919.

[13] U. Koehler, General overview of non-lithium battery systems and their safety issues, in: Electrochem. Power Sources Fundam. Syst. Appl., Elsevier B.V., 2019: pp. 21–46.

[14] H. Chen, Y. Xu, C. Liu, F. He, S. Hu, Storing Energy in China-An Overview, Elsevier Inc., 2016.

[15] C. Spataru, P. Bouffaron, Off-Grid Energy Storage, Elsevier Inc., 2016.

[16] H. Budde-Meiwes, J. Drillkens, B. Lunz, J. Muennix, S. Rothgang, J. Kowal, D.U. Sauer, A review of current automotive battery technology and future prospects, Proc. Inst. Mech. Eng. Part D: J. Automob. Eng. 227 (2013) 761–776.

[17] C. Liu, Z.G. Neale, G. Cao, Understanding electrochemical potentials of cathode materials in rechargeable batteries, Mater. Today. 19 (2016) 109–123.

[18] N. Nitta, F. Wu, J.T. Lee, G. Yushin, Li-ion battery materials: Present and future, Mater. Today. 18 (2015) 252–264.

[19] D. Cao, X. Sun, Q. Li, A. Natan, P. Xiang, H. Zhu, Lithium Dendrite in All-Solid-State Batteries: Growth Mechanisms, Suppression Strategies, and Characterizations, Matter. (2020) 1–38.

[20] Y. Yuan, K. Amine, J. Lu, R. Shahbazian-Yassar, Understanding materials challenges for rechargeable ion batteries with in situ transmission electron microscopy, Nat. Commun. 8 (2017) 1–14.

[21] T. Abe, T. Koyama, Thermodynamic modeling of the $LiCoO_2$-CoO_2 pseudo-binary system, CALPHAD. 35 (2011) 209–218.

[22] W. Zhao, J. Yi, P. He, H. Zhou, Solid-State Electrolytes for Lithium-Ion Batteries: Fundamentals, Challenges and Perspectives, Electrochem. Energy Rev. 2 (2019) 574–605.

[23] J. Schnell, T. Günther, T. Knoche, C. Vieider, L. Köhler, A. Just, M. Keller, S. Passerini, G. Reinhart, All-solid-state lithium-ion and lithium metal batteries – paving the way to large-scale production, J. Power Sources. 382 (2018) 160–175.

[24] B. Scrosati, Lithium rocking chair batteries: An old concept?, J. Electrochem. Soc. 139 (1992) 2776.

[25] D. Choi, W. Wang, Z. Zang, Lithium-ion batteries: Material Challenges and Perspectives, in: Lithium Ion Batter. Adv. Mater. Technol., CRC Press, Boca Raton, FL, 2011: pp. 1–50.

[26] J.W. Fergus, Recent developments in cathode materials for lithium ion batteries, J. Power Sources. 195 (2010) 939–954.

[27] B. Zhao, R. Ran, M. Liu, Z. Shao, A comprehensive review of $Li_4Ti_5O_{12}$-based electrodes for lithium-ion batteries: The latest advancements and future perspectives, Mater. Sci. Eng. R-Rep. 98 (2015) 1–71.

[28] T. Ohzuku, A. Ueda, N. Yamamoto, Zero-strain insertion material of $Li[Li_{1/3}Ti_{5/3}]O_4$ for rechargeable lithium cells, J. Electrochem. Soc. 142 (1995) 1431–1435.

[29] D. Bresser, E. Paillard, S. Passerini, Lithium-ion batteries (LIBs) for medium- and large-scale energy storage:, Elsevier Ltd., 2015.

[30] W.J.H. Borghols, M. Wagemaker, U. Lafont, E.M. Kelder, F.M. Mulder, Size effects in the $Li_{4+x}Ti_5O_{12}$ spinel, J. Am. Chem. Soc. 131 (2009) 17786–17792.

[31] T.-F. Yi, S.-Y. Yang, Y. Xie, Recent advances of $Li_4Ti_5O_{12}$ as a promising next generation anode material for high power lithium-ion batteries, J. Mater. Chem. A. 3 (2015) 5750–5777.

[32] D. Bresser, E. Paillard, M. Copley, P. Bishop, M. Winter, S. Passerini, The importance of "going nano" for high power battery materials, J. Power Sources. 219 (2012) 217–222.

[33] P.C. Tsai, W.D. Hsu, S.K. Lina, Atomistic structure and ab initio electrochemical properties of $Li_4Ti_5O_{12}$ defect spinel for li ion batteries, J. Electrochem. Soc. 161 (2014).

[34] T.F. Yi, H. Liu, Y.R. Zhu, L.J. Jiang, Y. Xie, R.S. Zhu, Improving the high rate performance of $Li_4Ti_5O_{12}$ through divalent zinc substitution, J. Power Sources. 215 (2012) 258–265.

[35] M. Wagemaker, D.R. Simon, E.M. Kelder, J. Schoonman, C. Ringpfeil, U. Haake, D. Lützenkirchen-Hecht, R. Frahm, F.M. Mulder, A kinetic two-phase and equilibrium solid solution in spinel $Li_{4+x}Ti_5O_{12}$, Adv. Mater. 18 (2006) 3169–3173.

[36] B. Ziebarth, M. Klinsmann, T. Eckl, C. Els, Lithium diffusion in the spinel phase Li4Ti5O12 and in the rocksalt phase Li7Ti5O12 of lithium titanate from first principles, Phys. Rev. B. 174301 (2014) 1–7.

[37] J. Zheng, J. Lu, K. Amine, F. Pan, Depolarization effect to enhance the performance of lithium

ions batteries, Nano Energy. 33 (2017) 497–507.

[38] A.. Bard, L.. Faulkner, Electrochemical methods - fundamentals and applications, 2nd ed., Wiley, New York, 2001.

[39] W. Jossen, A. Weydanz, Moderne Akkumulatoren richtig einsetzen, 1st ed.xu, Inge Reichardt Verlag, 2006.

[40] P. Albertus, S. Babinec, S. Litzelman, A. Newman, Status and challenges in enabling the lithium metal electrode for high-energy and low-cost rechargeable batteries, Nat. Energy. 3 (2018) 16–21.

[41] K. Xu, M. About, T. Article, Nonaqueous liquid electrolytes for lithium-based rechargeable batteries, Chem. Rev. 104 (2004) 4303–4418.

[42] Z.J. Zhang, P. Ramadass, W. Fang, Safety of lithium-ion batteries, in: Lithium-Ion Batter. Adv. Appl., Elsevier, 2014: pp. 409–435.

[43] M. Winter, R.J. Brodd, What are batteries, fuel cells, and supercapacitors?, Chem. Rev. 104 (2004) 4245–4269.

[44] I. Laresgoiti, S. Käbitz, M. Ecker, D.U. Sauer, Modeling mechanical degradation in lithium ion batteries during cycling: Solid electrolyte interphase fracture, J. Power Sources. 300 (2015) 112–122.

[45] G. Cui, Reasonable Design of High-Energy-Density Solid-State Lithium-Metal Batteries, Matter. 2 (2020) 805–815.

[46] C. Sun, J. Liu, Y. Gong, D.P. Wilkinson, J. Zhang, Recent advances in all-solid-state rechargeable lithium batteries, Nano Energy. 33 (2017) 363–386.

[47] S. Larfaillou, D. Guy-Bouyssou, F. Cras, S. Franger, Comprehensive characterization of all-solid-state thin films commercial microbatteries by electrochemical impedance spectroscopy, J. Power Sources. 319 (2016) 139–146.

[48] J. Janek, W.G. Zeier, A solid future for battery development, Nat. Publ. Gr. 1 (2016) 1–4.

[49] J.F.M. Oudenhoven, L. Baggetto, P.H.L. Notten, All-solid-state lithium-ion microbatteries: A review of various three-dimensional concepts, Adv. Energy Mater. 1 (2011) 10–33.

[50] Z. Zhang, Y. Shao, B. Lotsch, Y.S. Hu, H. Li, J. Janek, L.F. Nazar, C.W. Nan, J. Maier, M. Armand, L. Chen, New horizons for inorganic solid state ion conductors, Energy Environ. Sci. 11 (2018) 1945–1976.

[51] G. Homann, P. Meister, L. Stolz, J.P. Brinkmann, J. Kulisch, T. Adermann, M. Winter, J. Kasnatscheew, High-Voltage All-Solid-State Lithium Battery with Sulfide-Based Electrolyte: Challenges for the Construction of a Bipolar Multicell Stack and How to Overcome Them, ACS Appl. Energy Mater. (2020).

[52] A. Sepúlveda, J. Speulmanns, P.M. Vereecken, Bending impact on the performance of a flexible $Li_4Ti_5O_{12}$ -based all-solid-state thin-film battery, Sci. Technol. Adv. Mater. 19 (2018) 454–464.

[53] L.Y. Yang, H.Z. Li, L.Z. Cheng, S.T. Li, J. Liu, J. Min, K.J. Zhu, H. Wang, M. Lei, A three-dimensional surface modified carbon cloth designed as flexible current collector for high-performance lithium and sodium batteries, J. Alloys Compd. 726 (2017) 837–845.

[54] E. Borgia, The internet of things vision: Key features, applications and open issues, Comput. Commun. 54 (2014) 1–31.

[55] J. Glenneberg, F. Andre, I. Bardenhagen, F. Langer, J. Schwenzel, R. Kun, A concept for direct deposition of thin film batteries on flexible polymer substrate, J. Power Sources. 324 (2016) 722–728.

[56] J. Yuan, X. Zhang, C. Chen, Y. Hao, R. Agrawal, C. Wang, W. Li, H. Yu, Y. Yu, X. Zhu, Z. Xiong, Y. Xie, Facile fabrication of three-dimensional porous ZnO thin films on Ni foams for lithium ion battery anodes, Mater. Lett. 190 (2017) 37–39.

[57] D. Zhou, D. Shanmukaraj, A. Tkacheva, M. Armand, G. Wang, Polymer Electrolytes for Lithium-Based Batteries: Advances and Prospects, Chem. 5 (2019) 2326–2352.

[58] E. Quartarone, P. Mustarelli, Electrolytes for solid-state lithium rechargeable batteries: recent advances and perspectives, Chem. Soc. Rev. 40 (2011) 2525–2540.

[59] J.W. Fergus, Ceramic and polymeric solid electrolytes for lithium-ion batteries, J. Power Sources. 195 (2010) 4554–4569.

[60] U.S. Department of Energy, 2015 Annual progress report for energy storage R&D, 2015.

[61] A. Kwade, W. Haselrieder, R. Leithoff, A. Modlinger, F. Dietrich, K. Droeder, Current status and challenges for automotive battery production technologies, Nat. Energy. 3 (2018) 290–300.

[62] G. Berckmans, M. Messagie, J. Smekens, N. Omar, L. Vanhaverbeke, J. Van Mierlo, Cost projection of state of the art lithium-ion batteries for electric vehicles up to 2030, Energies. 10 (2017) 1314.

[63] E. Maiser, S. Michaelis, D. Müller, A. Kampker, H.H. Heimes, C. Deutskens, M. Ordung, J.-P. Ganser, N. Sarovic, S. Wessel, C. Hast, Batteriezellenproduktion in Deutschland - Chancen für den Maschinen- und Anlagenbau, Frankfurt am Main, Aachen, 2015.

[64] T. Schlick, G. Hertel, B. Hagemann, E. Maiser, M. Kramer, Zukunftsfeld Elektromobilität - Chance und Herausforderungen für den deutschen Maschinen- und Anlagenbau, 2011.

[65] W. Kräußlich, Maschinenbau & Zukunft - Batteriefertigung - Den gesamten Prozess im Blick - Das Siemens Portfolio für die Batterieherstellung, 2014.

[66] J. Kurfer, M. Westermeier, C. Tammer, G. Reinhart, Production of large-area lithium-ion cells - Preconditioning, cell stacking and quality assurance, CIRP Ann. - Manuf. Technol. 61 (2012) 1–4.

[67] PEM & VDMA, Produktionsprozess einer Lithium-Ionen Batteriezelle, Aachen, Frankfurt am Main, 2015.

[68] H. Bockholt, M. Indrikova, A. Netz, F. Golks, A. Kwade, The interaction of consecutive process steps in the manufacturing of lithium-ion battery electrodes with regard to structural and electrochemical properties, J. Power Sources. 325 (2016) 140–151.

[69] J. Smekens, R. Gopalakrishnan, N. Van den Steen, N. Omar, O. Hegazy, A. Hubin, J. Van Mierlo, Influence of electrode density on the performance of Li-ion batteries: Experimental and simulation results, Energies. 9 (2016) 1–12.

[70] S. Ahmed, P.A. Nelson, K.G. Gallagher, D.W. Dees, Energy impact of cathode drying and solvent recovery during lithium-ion battery manufacturing, J. Power Sources. 322 (2016) 169–178.

[71] D.L. Wood, J. Li, C. Daniel, Prospects for reducing the processing cost of lithium ion batteries, J. Power Sources. 275 (2015) 234–242.

[72] B. Bitsch, J. Dittmann, M. Schmitt, P. Scharfer, W. Schabel, N. Willenbacher, A novel slurry concept for the fabrication of lithium-ion battery electrodes with beneficial properties, J. Power Sources. 265 (2014) 81–90.

[73] G. Patry, A. Romagny, S. Martinet, D. Froelich, Cost modeling of lithium-ion battery cells for automotive applications, Energy Sci. Eng. 3 (2015) 71–82.

[74] X. Sun, P. V. Radovanovic, B. Cui, Advances in spinel $Li_4Ti_5O_{12}$ anode materials for lithium-ion batteries, New J. Chem. 39 (2015) 38–63.

[75] H. Naatz, R. Hoffmann, A. Hartwig, F. La Mantia, S. Pokhrel, L. Mädler, Determination of the flat band potential of nanoparticles in porous electrodes by blocking the substrate-electrolyte contact, J. Phys. Chem. C. 122 (2018) 2796–2805.

[76] J. Xiao, A. Kuc, S. Pokhrel, M. Schowalter, S. Parlapalli, A. Rosenauer, T. Frauenheim, L. Mädler, L.G.M. Pettersson, T. Heine, Evidence for Fe^{2+} in wurtzite coordination: Iron doping stabilizes ZnO nanoparticles, Small. 7 (2011) 2879–2886.

[77] J.A. Kemmler, S. Pokhrel, J. Birkenstock, M. Schowalter, A. Rosenauer, N. Barsan, U. Weimar, L. Mädler, Quenched, nanocrystalline $In_4Sn_3O_{12}$ high temperature phase for gas sensing applications, Sens. Actuators B.Chem. 161 (2012) 740–747.

[78] J.A. Kemmler, S. Pokhrel, L. Mädler, U. Weimar, N. Barsan, Flame spray pyrolysis for sensing at the nanoscale, Nanotechnology. 24 (2013) 442001 (14pp).

[79] M. Minnermann, H.K. Grossmann, S. Pokhrel, K. Thiel, H. Hagelin-Weaver, M. Bäumer, L. Mädler, Double flame spray pyrolysis as a novel technique to synthesize alumina-supported cobalt Fischer-Tropsch catalysts, Catal. Today. 214 (2013) 90–99.

[80] K.D. Kim, S. Pokhrel, Z. Wang, H. Ling, C. Zhou, Z. Liu, M. Hunger, L. Mädler, J. Huang, Tailoring high-performance Pd catalysts for chemoselective hydrogenation reactions via optimizing the parameters of the double-flame spray pyrolysis, ACS Catal. 6 (2016) 2372–2381.

[81] H. Naatz, S. Lin, R. Li, W. Jiang, Z. Ji, C.H. Chang, J. Köser, J. Thöming, T. Xia, A.E. Nel, L. Mädler, S. Pokhrel, Safe-by-design CuO nanoparticles via Fe-doping, Cu−O bond length variation, and biological assessment in cells and zebrafish embryos, ACS Nano. 11 (2017) 501–515.

[82] J.A.H. Dreyer, S. Pokhrel, J. Birkenstock, M.G. Hevia, M. Schowalter, A. Rosenauer, A. Urakawa, W.Y. Teoh, L. Mädler, Decrease of the required dopant concentration for δ-Bi_2O_3 crystal stabilization through thermal quenching during single-step flame spray pyrolysis, CrystEngComm. 18 (2016) 2046–2056.

[83] B. Sun, S. Pokhrel, D.R. Dunphy, H. Zhang, Z. Ji, X. Wang, M. Wang, Y.P. Liao, C.H. Chang, J. Dong, R. Li, L. Mädler, C.J. Brinker, A.E. Nel, T. Xia, Reduction of acute inflammatory effects of fumed silica nanoparticles in the lung by adjusting silanol display through calcination and metal doping, ACS Nano. 9 (2015) 9357–9372.

[84] B. Sun, X. Wang, Y.P. Liao, Z. Ji, C.H. Chang, S. Pokhrel, J. Ku, X. Liu, M. Wang, D.R. Dunphy, R. Li, H. Meng, L. Mädler, C.J. Brinker, A.E. Nel, T. Xia, Repetitive dosing of fumed silica leads to profibrogenic effects through unique structure-activity relationships and biopersistence in the lung, ACS Nano. 10 (2016) 8054–8066.

[85] L. Mädler, H.K. Kammler, R. Mueller, S.E. Pratsinis, Controlled synthesis of nanostructured particles by flame spray pyrolysis, J. Aerosol Sci. 33 (2002) 369–389.

[86] W.Y. Teoh, R. Amal, L. Mädler, Flame spray pyrolysis: An enabling technology for nanoparticles design and fabrication, Nanoscale. 2 (2010) 1324–1347.

[87] S. George, S. Pokhrel, T. Xia, B. Gilbert, Z. Ji, M. Schowalter, A. Rosenauer, R. Damoiseaux, K.A. Bradley, L. Mädler, A.E. Nel, Use of a rapid cytotoxicity screening approach to engineer a safer zinc oxide nanoparticle through iron doping, ACS Nano. 4 (2010) 15–29.

[88] T.J. Patey, R. Büchel, S.H. Ng, F. Krumeich, S.E. Pratsinis, P. Novák, Flame co-synthesis of $LiMn_2O_4$ and carbon nanocomposites for high power batteries, J. Power Sources. 189 (2009) 149–154.

[89] F.O. Ernst, H.K. Kammler, A. Roessler, S.E. Pratsinis, W.J. Stark, J. Ufheil, P. Novák, Electrochemically active flame-made nanosized spinels: $LiMn_2O_4$, $Li_4Ti_5O_{12}$ and $LiFe_5O_8$, Mater. Chem. Phys. 101 (2007) 372–378.

[90] O. Waser, R. Büchel, A. Hintennach, P. Novák, S.E. Pratsinis, Continuous flame aerosol synthesis of carbon-coated nano-$LiFePO_4$ for Li-ion batteries, J. Aerosol Sci. 42 (2011) 657–667.

[91] N.A. Hamid, S. Wennig, S. Hardt, A. Heinzel, C. Schulz, H. Wiggers, High-capacity cathodes

for lithium-ion batteries from nanostructured LiFePO 4 synthesized by highly-flexible and scalable flame spray pyrolysis, J. Power Sources. 216 (2012) 76–83.

[92] A. Birrozzi, M. Copley, J. Von Zamory, M. Pasqualini, S. Calcaterra, F. Nobili, A. Di Cicco, H. Rajantie, M. Briceno, E. Bilbé, L. Cabo-Fernandez, L.J. Hardwick, D. Bresser, S. Passerini, Scaling up "nano" $Li_4Ti_5O_{12}$ for high-power lithium-ion anodes using large scale flame spray pyrolysis, J. Electrochem. Soc. 162 (2015) 2331–2338.

[93] T. Karhunen, J. Välikangas, T. Torvela, A. Lähde, U. Lassi, J. Jokiniemi, Effect of doping and crystallite size on the electrochemical performance of $Li_4Ti_5O_{12}$, J. Alloys Compd. 659 (2016) 132–137.

[94] O. Waser, Flame Aerosol Synthesis of Li-ion Battery Materials, 2015.

[95] L. Kavan, J. Procházka, T.M. Spitler, M. Kalbáč, M. Zukalová, T. Drezen, M. Grätzel, Li Insertion into $Li_4Ti_5O_{12}$ (Spinel), J. Electrochem. Soc. 150 (2003) A1000–A1007.

[96] F. Meierhofer, H. Li, M. Gockeln, R. Kun, T. Grieb, A. Rosenauer, U. Fritsching, J. Kiefer, J. Birkenstock, L. Mädler, S. Pokhrel, Screening precursor–solvent combinations for $Li_4Ti_5O_{12}$ energy storage material using flame spray pyrolysis, ACS Appl. Mater. Interfaces. 9 (2017) 37760–37777.

[97] M. Gockeln, S. Pokhrel, F. Meierhofer, J. Glenneberg, M. Schowalter, A. Rosenauer, U. Fritsching, M. Busse, L. Mädler, R. Kun, Fabrication and performance of $Li_4Ti_5O_{12}$/C Li-ion battery electrodes using combined double flame spray pyrolysis and pressure-based lamination technique, J. Power Sources. 374 (2018) 97–106.

[98] M. Gockeln, J. Glenneberg, M. Busse, S. Pokhrel, L. Mädler, Flame aerosol deposited $Li_4Ti_5O_{12}$ layers for flexible, thin film all-solid-state Li-ion batteries, Nano Energy. 49 (2018) 564–573.

[99] D. Mcnulty, H. Geaney, E. Carroll, N. Wagner, A.M. Svensson, F. Vullum-bruer, Liquid-feed flame spray pyrolysis as alternative synthesis for electrochemically active nano-sized Li_2MnSiO_4, Transl. Mater. Res. 3 (2016) 025001.

[100] V. Lobintsev, Synthesis of Li-ion battery cathode materials by flame spray pyrolysis, 2016.

[101] N.A. Hamid, Cathode materials produced by spray flame synthesis for lithium ion batteries, 2013.

[102] R. Strobel, S.E. Pratsinis, Flame aerosol synthesis of smart nanostructured materials, J. Mater. Chem. 17 (2007) 4743–4756.

[103] M. Høj, D.K. Pham, M. Brorson, L. Mädler, A.D. Jensen, J.D. Grunwaldt, Two-nozzle flame spray pyrolysis (FSP) synthesis of CoMo/Al_2O_3 hydrotreating catalysts, Catal. Lett. (2013) 1–9.

[104] M. Piacentini, R. Strobel, M. Maciejewski, S.E. Pratsinis, A. Baiker, Flame-made Pt-Ba/Al_2O_3 catalysts: Structural properties and behavior in lean-NO_x storage-reduction, J. Catal. 243 (2006) 43–56.

[105] Z. Wang, S. Pokhrel, M. Chen, M. Hunger, L. Mädler, J. Huang, Palladium-doped silica-alumina catalysts obtained from double-flame FSP for chemoselective hydrogenation of the model aromatic ketone acetophenone, J. Catal. 302 (2013) 10–19.

[106] M. Minnermann, S. Pokhrel, K. Thiel, R. Henkel, J. Birkenstock, T. Laurus, A. Zargham, J.I. Flege, V. Zielasek, E. Piskorska-Hommel, J. Falta, L. Mädler, M. Bäumer, Role of palladium in iron based fischer-tropsch catalysts prepared by flame spray pyrolysis, J. Phys. Chem. C. 115 (2011) 1302–1310.

[107] M. Schubert, S. Pokhrel, A. Thomé, V. Zielasek, T.M. Gesing, F. Roessner, L. Mädler, M. Bäumer, Highly active Co-Al_2O_3-based catalysts for CO_2 methanation with very low platinum promotion prepared by double flame spray pyrolysis, Catal. Sci. Technol. 6 (2016) 7449–7460.

[108] R. Strobel, F. Krumeich, S.E. Pratsinis, A. Baiker, Flame-derived Pt/Ba/$Ce_xZr_{1-x}O_2$: Influence of support on thermal deterioration and behavior as NO_x storage-reduction catalysts, J. Catal. 243 (2006) 229–238.

[109] R. Strobel, L. Mädler, M. Piacentini, M. Maciejewski, A. Baiker, S.E. Pratsinis, Two-nozzle flame synthesis of Pt/Ba/Al_2O_3 for NO_x storage, Chem. Mater. 18 (2006) 2532–2537.

[110] S. Pokhrel, A.E. Nel, L. Mädler, Custom-designed nanomaterial libraries for testing metal oxide toxicity, Acc. Chem. Res. 46 (2013) 632–641.

[111] H.K. Grossmann, T. Grieb, F. Meierhofer, M.J. Hodapp, D. Noriler, A. Gröhn, H.F. Meier, U. Fritsching, K. Wegner, L. Mädler, Nanoscale mixing during double-flame spray synthesis of heterostructured nanoparticles, J. Nanoparticle Res. 17 (2015) 1–16.

[112] T. Karhunen, A. Lähde, J. Leskinen, R. Büchel, O. Waser, U. Tapper, J. Jokiniemi, Transition

metal-doped lithium titanium oxide nanoparticles made using flame spray pyrolysis, ISRN Nanotechnol. 2011 (2011) 1–6.

[113] F.O. Ernst, R. Büchel, R. Strobel, S.E. Pratsinis, One-step flame-synthesis of carbon-embedded and -supported platinum clusters, Chem. Mater. 20 (2008) 2117–2123.

[114] M. Kammoun, S. Berg, H. Ardebili, Flexible thin-film battery based on graphene-oxide embedded in solid polymer electrolyte, Nanoscale. 7 (2015) 17516–17522.

[115] A. Mukanova, A. Jetybayeva, S.T. Myung, S.S. Kim, Z. Bakenov, A mini-review on the development of Si-based thin film anodes for Li-ion batteries, Mater. Today Energy. 9 (2018) 49–66.

[116] S.Y. Chew, T.J. Patey, O. Waser, S.H. Ng, R. Büchel, A. Tricoli, F. Krumeich, J. Wang, H.K. Liu, S.E. Pratsinis, P. Novák, Thin nanostructured $LiMn_2O_4$ films by flame spray deposition and in situ annealing method, J. Power Sources. 189 (2009) 449–453.

[117] L. Mädler, A.A. Lall, S.K. Friedlander, One-step aerosol synthesis of nanoparticle agglomerate films: simulation of film porosity and thickness, Nanotechnology. 17 (2006) 4783–4795.

[118] V. Baric, L. Colombi, L. Mädler, Compaction-induced restructuring of aggregated nanoparticle films using the discrete element method, Powder Technol. 342 (2019) 773–779.

[119] H.P. Zhu, Z.Y. Zhou, R.Y. Yang, A.B. Yu, Discrete particle simulation of particulate systems: A review of major applications and findings, Chem. Eng. Sci. 63 (2008) 5728–5770.

[120] S. Salameh, J. Schneider, J. Laube, A. Alessandrini, P. Facci, J.W. Seo, L.C. Ciacchi, L. Mädler, Adhesion mechanisms of the contact interface of TiO_2 nanoparticles in films and aggregates, Langmuir. 28 (2012) 11457–11464.

[121] J. Laube, M. Dörmann, H.J. Schmid, L. Mädler, L. Colombi Ciacchi, Dependencies of the Adhesion Forces between TiO_2 Nanoparticles on Size and Ambient Humidity, J. Phys. Chem. C. 121 (2017) 15294–15303.

[122] J. Laube, V. Baric, S. Salameh, L. Mädler, L. Colombi Ciacchi, A new contact model for the discrete element method simulation of TiO_2 nanoparticle films under mechanical load, Granul. Matter. 20 (2018) 1–16.

[123] H. Xia, Z. Luo, J. Xie, Nanostructured $LiMn_2O_4$ and their composites as high-performance

cathodes for lithium-ion batteries, Prog. Nat. Sci. Mater. Int. 22 (2012) 572–584.

[124] S.O. Schopf, S. Salameh, L. Mädler, Transfer of highly porous nanoparticle layers to various substrates through mechanical compression, Nanoscale. 5 (2013) 3764–72.

[125] J. Kemmler, S.O. Schopf, L. Mädler, N. Barsan, U. Weimar, New process technologies for the deposition of semiconducting metal oxide nanoparticles for sensing, Procedia Eng. 87 (2014) 24–27.

[126] M. Gockeln, T. Ruiter, A.P. Saura, V. Baric, J. Glenneberg, M. Busse, S. Pokhrel, R. Kun, L. Mädler, Enhancing the utilization of porous $Li_4Ti_5O_{12}$ layers for thin-film lithium-ion batteries, ACS Appl. Energy Mater. 3 (2020) 9667–9675.

[127] J. Birkenstock, R.X. Fischer, T. Messner, The Bremen Rietveld analysis and structure suite, Zeitschrift Fur Krist. Suppl. 1 (2006) 237–242.

[128] S. Pokhrel, J. Birkenstock, A. Dianat, J. Zimmermann, M. Schowalter, A. Rosenauer, L.C. Ciacchi, L. Mädler, In situ high temperature X-ray diffraction, transmission electron microscopy and theoretical modeling for the formation of WO_3 crystallites, CrystEngComm. 17 (2015) 6985–6998.

[129] J. Birkenstock, R.X. Fischer, T. Messner, BRASS, the Bremen Rietveld analysis and structure suite, Zeitschrift Fur Krist. Suppl. 1 (2006) 237–242.

[130] S. Pokhrel, J. Birkenstock, M. Schowalter, A. Rosenauer, L. Mädler, Growth of ultrafine single crystalline WO_3 nanoparticles using flame spray pyrolysis, Cryst. Growth Des. 10 (2010) 632–639.

[131] E.P. Barrett, L.G. Joyner, P.P. Halenda, The determination of pore volume and area distributions in porous substances. I. Computations from nitrogen isotherms, J. Am. Chem. Soc. 73 (1951) 373–380.

[132] J.H. de Boer, B.C. Lippens, B.G. Linsen, J.C.P. Broekhoff, A. van den Heuvel, T.J. Osinga, The t-curve of multimolecular N_2-adsorption, J. Colloid Interface Sci. 21 (1966) 405–414.

[133] L.J. Van der Pauw, A method of measuring specific resistivity and Hall effect of discs of arbitrary shape, Philips Res. Reports. 13 (1958) 1–9.

[134] W. Versnel, Analysis of symmetrical Van der Pauw structures with finite contacts, Solid State

Electron. 21 (1978) 1261–1268.

[135] S. Salameh, R. Scholz, J.W. Seo, L. Mädler, Contact behavior of size fractionated TiO_2 nanoparticle agglomerates and aggregates, Powder Technol. 256 (2014) 345–351.

[136] D.O. Potyondy, P.A. Cundall, A bonded-particle model for rock, Int. J. Rock Mech. Min. Sci. 41 (2004) 1329–1364.

[137] P. Serp, J.L. Figueiredo, Carbon Materials for Catalysis, A John Wiley & Sons, INC., Publication, Hoboken, New Jersey, 2009.

[138] Z.Q. Li, C.J. Lu, Z.P. Xia, Y. Zhou, Z. Luo, X-ray diffraction patterns of graphite and turbostratic carbon, Carbon N. Y. 45 (2007) 1686–1695.

[139] J.N. Rouzaud, A. Oberlin, C. Beny-Bassez, Carbon films: Structure and microtexture (optical and electron microscopy, Raman spectroscopy), Thin Solid Films. 105 (1983) 75–96.

[140] J.-N. Rouzaud, C. Clinard, Quantitative high-resolution transmission electron microscopy: a promising tool for carbon materials characterization, Fuel Process. Technol. 77 (2002) 229–235.

[141] M. Pawlyta, H. Hercman, Transmission electron microscopy (TEM) as a tool for identification of combustion products: Application to black layers in speleothems, Ann. Soc. Geol. Pol. 86 (2016) 237–248.

[142] N. Poirier, S. Derenne, J.N. Rouzaud, C. Largeau, A. Mariotti, J. Balesdent, J. Maquet, Chemical structure and sources of the macromolecular, resistant, organic fraction isolated from a forest soil (Lacadee, south-west France), Org. Geochem. 31 (2000) 813–827.

[143] R.D. Heidenreich, W.M. Hess, L.L. Ban, A test object and criteria for high resolution electron microscopy, J. Appl. Crystallogr. 1 (1968) 1–19.

[144] S. Scharner, W. Weppner, P. Schmid-Beurmann, Evidence of two-phase formation upon lithium insertion into the $Li_{1.33}Ti_{1.67}O_4$ Spinel, J. Electrochem. Soc. 146 (1999) 857–861.

[145] K.M. Colbow, J.R. Dahn, R.R. Haering, Structure and electrochemistry of the spinel oxides $LiTi_2O_4$ and $Li_{4/3}Ti_{5/3}O_4$, J. Power Sources. 26 (1989) 397–402.

[146] C. Heubner, A. Nickol, J. Seeba, S. Reuber, N. Junker, M. Wolter, M. Schneider, A. Michaelis, Understanding thickness and porosity effects on the electrochemical performance of

$LiNi_{0.6}Co_{0.2}Mn_{0.2}O_2$-based cathodes for high energy Li-ion batteries, J. Power Sources. 419 (2019) 119–126.

[147] H. Li, H. Zhou, Enhancing the performances of Li-ion batteries by carbon-coating: present and future, Chem. Commun. 48 (2012) 1201–1217.

[148] Z. Zhu, F. Cheng, J. Chen, Investigation of effects of carbon coating on the electrochemical performance of $Li_4Ti_5O_{12}$/C nanocomposites, J. Mater. Chem. A. 1 (2013) 9484–9490.

[149] H. Liu, G. Wen, S. Bi, P. Gao, Enhanced rate performance of nanosized $Li_4Ti_5O_{12}$/graphene composites as anode material by a solid state-assembly method, Electrochim. Acta. 171 (2015) 114–120.

[150] C.P. Sandhya, B. John, C. Gouri, Surfactant-assisted sol-gel route to lithium titanate and its electrochemical properties, J. Alloys Compd. 655 (2016) 238–243.

[151] X. Sun, M. Hegde, Y. Zhang, M. He, L. Gu, Y. Wang, J. Shu, P. V. Radovanovic, B. Cui, Structure and electrochemical properties of spinel $Li_4Ti_5O_{12}$ nanocomposites as anode for lithium-ion battery, Int. J. Electrochem. Sci. 9 (2014) 1583–1596.

[152] J. Wang, X.-M. Liu, H. Yang, X. Shen, Characterization and electrochemical properties of carbon-coated $Li_4Ti_5O_{12}$ prepared by a citric acid sol–gel method, J. Alloys Compd. 509 (2011) 712–718.

[153] PEM & VDMA, Leaflet: "Der Produktionsprozess einer Lithium-Ionen-Folienzelle," 2015.

[154] Y. Sheng, C. Fell, Y. Son, B. Metz, Effect of calendering on electrode wettability in lithium-ion batteries, Front. Energy Res. 2 (2014) 1–8.

[155] S.G. Lee, D.H. Jeon, Effect of electrode compression on the wettability of lithium-ion batteries, J. Power Sources. 265 (2014) 363–369.

[156] H. Bockholt, W. Haselrieder, A. Kwade, Intensive powder mixing for dry dispersing of carbon black and its relevance for lithium-ion battery cathodes, Powder Technol. 297 (2016) 266–274.

[157] J. Glenneberg, I. Bardenhagen, F. Langer, M. Busse, R. Kun, Time resolved impedance spectroscopy analysis of lithium phosphorous oxynitride - LiPON layers under mechanical stress, J. Power Sources. 359 (2017) 157–165.

[158] P. Schichtel, M. Geiß, T. Leichtweiß, J. Sann, D.A. Weber, J. Janek, On the impedance and

phase transition of thin film all-solid-state batteries based on the $Li_4Ti_5O_{12}$ system, J. Power Sources. 360 (2017) 593–604.

[159] J. Li, Y.L. Jin, X.G. Zhang, H. Yang, Microwave solid-state synthesis of spinel $Li_4Ti_5O_{12}$ nanocrystallites as anode material for lithium-ion batteries, Solid State Ionics. 178 (2007) 1590–1594.

[160] Y.S. Lee, K.S. Ryu, Study of the lithium diffusion properties and high rate performance of $TiNb_6O_{17}$ as an anode in lithium secondary battery, Sci. Rep. 7 (2017) 1–13.

[161] P.A. Medina, H. Zheng, B.D. Fahlman, P. Annamalai, A. Swartbooi, L. le Roux, M.K. Mathe, $Li_4Ti_5O_{12}$/graphene nanoribbons composite as anodes for lithium ion batteries, Springerplus. 4 (2015) 1–7.

[162] C.K. Lan, Q. Bao, Y.H. Huang, J.G. Duh, Embedding nano-$Li_4Ti_5O_{12}$ in hierarchical porous carbon matrixes derived from water soluble polymers for ultra-fast lithium ion batteries anodic materials, J. Alloys Compd. 673 (2016) 336–348.

[163] H. Zheng, G. Liu, X. Song, P. Ridgway, S. Xun, V.S. Battaglia, Cathode performance as a function of inactive material and void fractions, J. Electrochem. Soc. 157 (2010) A1060–A1066.

[164] B. Ludwig, Z. Zheng, W. Shou, Y. Wang, H. Pan, Solvent-free manufacturing of electrodes for lithium-ion batteries, Sci. Rep. 6, 23150 (2016).

[165] A.C. Kozen, A.J. Pearse, C.-F. Lin, M. Noked, G.W. Rubloff, Atomic layer deposition of the solid electrolyte LiPON, Chem. Mater. 27 (2015) 5324–5331.

13. Additional Information

13.1. Relevant Publications, Presentations and Patents

F. Meierhofer, H. Li, M. Gockeln, R. Kun, T. Grieb, A. Rosenauer, U. Fritsching, J. Kiefer, J. Birkenstock, L. Mädler, S. Pokhrel, *"Screening Precursor Solvent Combinations for $Li_4Ti_5O_{12}$ Energy Storage Material Using Flame Spray Pyrolysis"*, ACS Appl. Mater. Interfaces. 9 (2017) 37760–37777. doi:10.1021/acsami.7b1143

M. Gockeln, S. Pokhrel, F. Meierhofer, J. Glenneberg, M. Schowalter, A. Rosenauer, U. Fritsching, M. Busse, L. Mädler, R. Kun, *"Fabrication and performance of $Li_4Ti_5O_{12}$/C Li-ion battery electrodes using combined double flame spray pyrolysis and pressure-based lamination technique"*, J. Power Sources. 374 (2018) 97–106. doi:10.1016/j.jpowsour.2017.11.016

M. Gockeln, J. Glenneberg, M. Busse, S. Pokhrel, L. Mädler, R. Kun *"Flame aerosol deposited $Li_4Ti_5O_{12}$ layers for flexible, thin-film all-solid-state Li-ion batteries"*, Nano Energy. 49 (2018) 564–573. doi:10.1016/j.nanoen.2018.05.007

M. Gockeln, S. Pokhrel, F. Meierhofer, J. Glenneberg, L. Mädler, R. Kun, *"Fabrication and performance of $Li_4Ti_5O_{12}$/C Li-ion battery electrodes using combined double flame spray pyrolysis and lamination technique"*, Poster at International Meeting on Lithium-ion Batteries 2018 in Kyoto, Japan. http://www.imlb2018.org/pdf/a11_2554203.pdf

Patent: „Lösungs- und bindemittelfreie Elektrodenherstellung für Lithiumionenbatterien durch kombinierte Doppelflammensprühpyrolyse und Laminierungstechnik". Registered as German patent: DE 10 2017 213 024.5

13.2. Student Supervision

In this dissertation, the results from the supervision of the master student Ana Palacios Saura are included: "Effect of Compression on Thin Film Batteries deposited via Flame Spray Pyrolysis", 2019 [126].

13.3. Alternative Routes for $Li_4Ti_5O_{12}$ Thin-Film Deposition

In an analogous approach for depositing crystalline LTO thin-films on flexible KaCu substrates, LTO nanoparticles were synthesized *via* FSP. LTO particles were collected on a glass-fiber particle-collecting unit (600 mm) before individual pieces of 10 mm diameter were punched out and transferred to KaCu substrates *via* transfer-lamination technique. The transferred LTO layers had significant glass-fiber residues on their surfaces. The rough topography was improperly coverable by the thin LiPON layer, which persistently resulted in short circuit formation upon lithium deposition. To overcome this issue, the experiment was repeated with a metal-fiber filter since the metal-fibers are less prone to detachment (**Fig. A1a**). Indeed, metal-fibers were absent after transfer-lamination from a metal-fiber filter and functional LIB cells were fabricated. The transferred layers showed, however, incompletely transferred LTO layers (**Fig. A1b**) with low loading reproducibility.

Another approach was conducted, in which the LTO particles were *in-situ* deposited (600 mm) on various substrates, using a custom-built sample holder (**Fig. A1c**). Five electrodes were placed in pocket masks and fixed with metal pieces (**Fig. A1d**). After mounting the sample holder into the FSP reactor (**Fig. A1e**) and running the deposition process, substrates were successfully covered. However, copper layers were partially oxidized due to high temperatures in absence of substrate cooling (**Fig. A1f**). Moreover, the amount of deposited LTO was fairly low since the particles were rather sucked through the metal mesh than being deposited to the air-impermeable substrates.

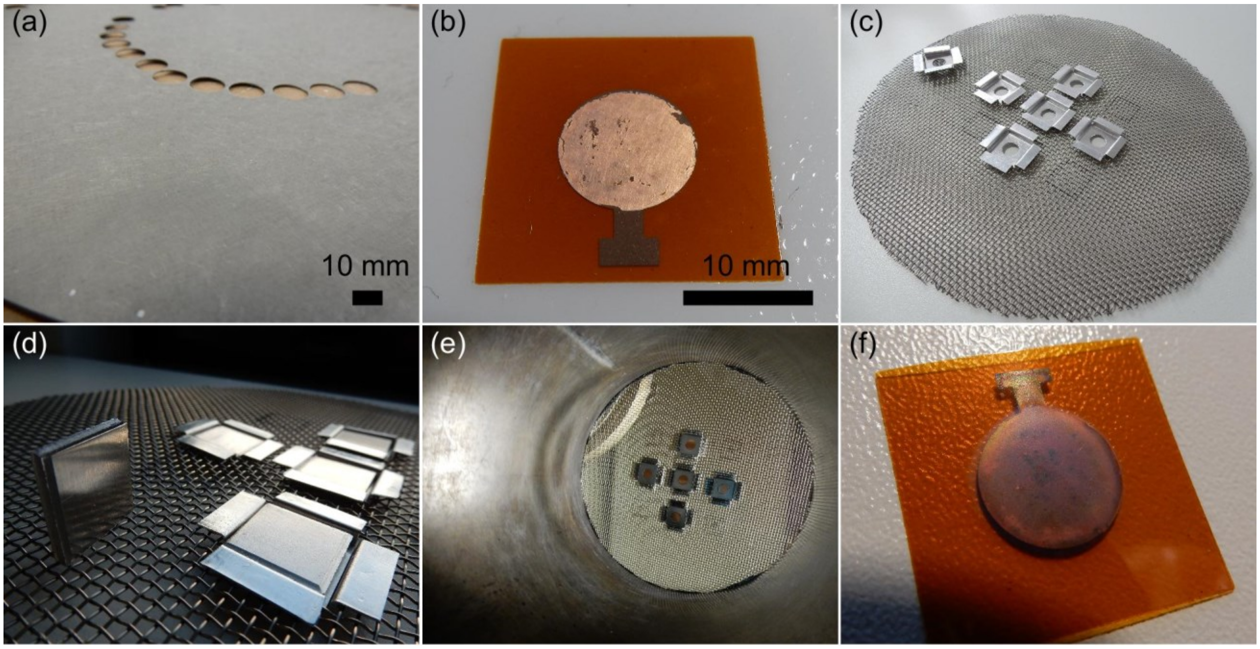

Fig. A1 (a) LTO collected on metal-fiber particle collector with punched-out pieces (Ø=10 mm) for transfer-lamination, **(b)** transfer-laminated LTO thin-film on KaCu (20x20 mm²) with visible layer inhomogeneities, **(c)** custom-made metal-mesh with pockets for KaCu substrates, **(d)** KaCu substrates fixed with metal weights, **(e)** substrates mounted in FSP reactor, ready for LTO deposition, **(f)** *in-situ* deposited LTO on partially oxidized KaCu substrates.